MASTER'S THESIS

Initialisation Protocols for Quantum Memory Writing with Vanadium Defects in Silicon Carbide

Author:
Adrian P.J. Sidhu

Supervisor:
prof. dr. ir. Caspar van der Wal

Second Examiner:
prof. dr. Steven Hoekstra

Daily Supervisors:
Joop Hendriks MSc.
dr. Carmem Gilardoni

Master's Thesis for the Programme:
MSc Physics - Quantum Universe
Zernike Institute for Advanced Materials
Faculty of Science & Engineering
University of Groningen
May 2022 - May 2023

Initialisation Protocols for Quantum Memory Writing with Vanadium Defects in Silicon Carbide

Adrian Parveet James Sidhu
S3340058

Abstract

Quantum memories are necessary for efficient long-distance quantum networks. The vanadium (V) defect in silicon carbide (SiC) exhibits promising qualities for use as a quantum memory in telecom-compatible quantum communication technologies. While these defects are optically addressable at telecom wavelengths, the rich hyperfine structure of the ground state makes high-fidelity coherent control difficult. To solve this, the system needs to be initialised into a pure quantum state. This research investigates steady-state two-laser initialisation protocols for the neutral charge state V^{4+} defect in 4H-SiC at 2 K. Based on an exhaustive theoretical framework of the system, the two-laser perturbed populations of the ground and excited eigenstates were simulated using a Lindbladian model. These populations were then analysed to find regions of maximised state fidelity. Initialisation predicted by the simulated model was experimentally verified for an inhomogeneous ensemble of V defects, motivating its use for developing theoretical initialisation protocols at the single-defect level. It was found, in both experiment and simulation, that initialisation is strongly dependent on the spin relaxation of the system (and hence the temperature), the polarisation of the optical driving fields, and the extent of inhomogeneity in the system. High-fidelity initialisation was only seen in two ground eigenstates within the strong electron Zeeman regime ($\gtrsim 30$ mT). For the inhomogeneous case, the maximum theoretical fidelity found was $F < 0.1$, suggesting that ensembles of V defects are not suitable for applications in quantum technology. The maximum theoretical single-defect fidelity found at 2 K was $F > 0.921$, with a corresponding qubit candidate that might be coherently driven with electric fields. Furthermore, a simplified temperature dependence was modelled and resulted in fidelities of $F > 0.999$ at 100 mK, similar to previous work done on this system. This research provides a solid framework to achieve high-fidelity initialisation for V defects in SiC, enabling further experimental studies on the coherence properties of individual vanadium defects at 2 K.

Initialisation Protocols for Quantum Memory Writing with Vanadium Defects in Silicon Carbide

Adrian Parveet James Sidhu

S3340058

Acknowledgements

I write these acknowledgements now with over a week of distance from this project. Looking back, I am really so grateful for having been able to work on such a fascinating topic, and to learn from such brilliant minds.

To Caspar van der Wal, my primary supervisor, I thank you for your guidance, and especially for your trust in the work I was doing. Throughout all those Monday meeting discussions and disagreements, I always felt that my knowledge and insight was appreciated. I went away from every meeting full of ideas, and your supervision has really helped me to develop my abilities as an independent researcher. I also appreciate all of our conversations outside of physics, and look forward to keeping up to date with your running! Thank you for letting me be a part of, and letting me contribute to, the Quantum Devices team.

To Joop Hendriks, the best daily supervisor I could have asked for! I really appreciate all those times where you took a minute (or realistically, an hour) to help me out with something I was stuck on, or to give some advice, or to lend me your coffee card. I have learnt so much from working with you, not just about our system and our lab, but also about research and science as a whole. We made a great team, and I am really happy with what we have achieved in this past year. I wish you all the best with the house project, and of course, with finishing your PhD!

To Carmem Gilardoni, thank you for teaching me the fundamentals I needed to know to start this project. The theoretical work you did was fascinating, and I am so happy I got to learn it from you first-hand. Thank you as well for staying involved in the project even though you were no longer a part of the Quantum Devices team - our fortnightly meetings were always so helpful. I hope you are enjoying Cambridge, and best of luck with the rest of your postdoc!

To the FND, thank you for creating such a welcoming environment. It was a pleasure to be a part of the group. To Steven Hoekstra, thank you for taking the time to be my second examiner.

To my friends in Groningen, thank you for the good times. It was a great six years together, and I know we will all see each other very soon. To my sister, Anna, thank you for always being a phone call away. While we did not speak much in the final weeks of my thesis, I knew you were always there for me. To my parents, thank you for your support from afar. I would not be where I am without everything you have done and sacrificed for me. For this I will always be grateful.

Finally, to Sofia Llàcer Caro, my partner, my best friend. I would not have been able to finish this project without your unconditional support. The thought of taking our next steps together was what kept me going. Thank you for everything. *T'estime.*

Contents

1 Introduction

Quantum Networks and Repeaters

Quantum bits (qubits) are the next step in the evolution of computing. A qubit is a two-level quantum system and the basic unit of information in quantum information theory [1]. A classical bit can be in one of the binary states 0 or 1. In a qubit however, these binary states are represented by the quantum state (e.g. spin state) of the system. In this way, a qubit can be in the states 0, 1, or a coherent superposition of these two binary states. Computers utilising qubits (quantum computers) are theorised to perform certain calculations at a monumentally faster speed than a classical computer due to this superposition state, a phenomenon termed quantum supremacy [2]. Since 2019, there have been several claims of quantum supremacy [3–6]. It is of no doubt then that in the coming decades qubits will play an essential role in the computing industry and beyond. Qubits can be used for more than just computation. In fact, to be able to transfer information between quantum computers, a special network is needed - a quantum network [7]. Similar to a classical network, a quantum network enables communication between different quantum computers by using qubits as a messenger of information. Quantum networks can be used for cryptography [8, 9], distributed computing [10, 11], clock synchronisation [12], and more [13, 14]. Of interest in this research are quantum networks for use in communication. Generally, there are two communication channels used in quantum network infrastructure: ground-based fibre-optic channels [15, 16] and satellite-based free-space channels [17, 18], with each having its unique advantages and disadvantages. A particular advantage of optic fibre channels is that much of the required infrastructure already exists from current telecommunication networks. In the future, quantum networks are likely to be composed of a combination of fibre-optic and free-space channels. Fibre-optic channels are typically used for smaller, more localised scales (e.g. within a city district), whereas free-space channels are used for communication at larger scales (e.g. between cities) [19–22].

That being said, fibre-optic channels do not need to be restricted to small scales. The basic structure of a quantum network involves two end nodes (quantum processors) connected via a communication channel [7, 23] over which qubits are sent. For fibre-optic channels, the distance of information transmission is severely limited by photon losses [24, 25]. Furthermore, classical amplifiers cannot be used as due to the no-cloning theorem quantum states cannot be simply copied [26]. To achieve efficient long-distance transmission of qubits with optical fibres, it is necessary to introduce quantum repeaters (or repeater nodes) between the end nodes [27]. A simplified picture of the conventional method used by quantum repeaters is as follows [7, 28–37]: repeater nodes are equipped with a writable quantum memory; a memory capable of storing (and retrieving) quantum states. Quantum memories between adjacent repeater nodes are then entangled through the transmission of photons which themselves are entangled with the memory from one of the nodes. Then, via entanglement swapping [38], the distant end nodes can eventually be entangled and a quantum communication channel established between the end nodes. There has been a lot of progress made in the past decades on quantum repeaters, both in experimental proposals [32, 34, 39–41] and practical demonstrations [42–45]. However, a network-scalable quantum repeater is yet to be built. Since repeater systems write on and read out of a quantum memory using photons in the infrared (i.e. via optical fibres), a high degree of coherent control (controlling quantum phenomena with light [46]) over the qubit system is necessary. Nitrogen-vacancy (NV) centres in diamond have shown a lot of promise for coherent control at room temperature [47–50]. However, NV centres are optically active in the visible and near-infrared regions [47, 51, 52] resulting in high levels of attenuation in optical fibres [53, 54]. While wavelength conversion techniques exist, the conversion efficiencies are still less than 50% [55, 56]. What is needed then, is a system with high coherent control that is also optically

active in the telecom band $1260 - 1675$ nm (optimal spectral band for optical fibres - defined by the International Telecommunications Union [54]). One such system is the vanadium (V) defect in silicon carbide (SiC).

Vanadium Defects in Silicon Carbide

In this thesis, the neutral (and stable [57]) charge state V^{4+} in 4H-SiC is investigated. It will be referred to hereafter as the V defect in SiC. The V defect in SiC has been subject to considerable scrutiny in the past years due to its favourable qualities for technological applications, and in particular, for its possible use as a quantum memory. Firstly, silicon carbide is a staple of the semiconductor industry with mature fabrication technology dating back to 1955 [58, 59]. Vanadium in 4H-SiC has a low-temperature zero-phonon line (ZPL) at ~ 1280 nm [60–62] commonly referred to as the α-line, which sits comfortably in the telecom O-band ($1260 - 1360$ nm [54]). Naturally occurring ^{51}V also has a nuclear spin of $7/2$, which when combined with the $1/2$ effective spin of the strongly localised 3d electron in vanadium, results in a rich hyperfine structure. A 2022 study was able to measure coherence times T_2 of this spin structure that went beyond tens of microseconds [62]. Studies on other solid-state systems have shown that qubits utilising electron-nuclear spin coupling (i.e. hyperfine coupling) can achieve coherence times sufficient for quantum memory purposes, in particular due to the long-lived coherence of nuclear spins (resulting from their small magnetic moments), while still maintaining optical accessibility through the electron spin states [63–66]. Thus the V defect in SiC with its optical accessibility, and hyperfine-coupled states with coherent times sufficient for basic quantum operations, is a very plausible candidate.

The properties of V defects in SiC are still being characterised. Work has been done to largely characterise the optical and spin-state energy structure of these defects [61, 67–71], along with the system Hamiltonian [70, 72]. Furthermore, work done by Gilardoni [72] (Chapter 6) and Astner et al. [73] show spin-relaxation times T_1 exceeding seconds, and as mentioned, work by Hendriks et al. [62] showed coherence times T_2 of at least tens of microseconds. These studies are the first steps towards achieving full coherent control of the V defect in SiC. For technological applications, quantum systems must be in a pure state, or in other words, have a high fidelity. In general, quantum systems in thermal equilibrium are in a mixed state and have a low fidelity. To go from a mixed state to a pure state, the system must be spin polarised, or *initialised*. The specific methods of initialising are called initialisation protocols. Since characterisation studies of V defects in SiC for quantum technology applications have only been conducted recently, so far, there has been seldom research done on initialising this system. Initialising V defects in SiC is not a trivial task, as the ground-state hyperfine structure is composed of 16 levels. Currently, only one initialisation protocol exists for V defects in SiC. Tissot et al. [74] developed a ratchet-type dissipative initialisation protocol at 100 mK. While simulated fidelities of > 0.999 were achieved, 100 mK is a less practical and more expensive operating temperature than 2 K, and requires the use of dilution fridges. This then motivates the development of initialisation protocols suited for 2 K, enabling further study of high-fidelity coherence of V defects in SiC at and around this temperature.

Research Aim and Thesis Outline

In this work, steady-state dissipative initialisation protocols are developed for V^{4+} defects in 4H-SiC at an operating temperature of 2 K. This is achieved using a simulated Lindbladian model. The ultimate aim of this research is to achieve high-fidelity initialisation with these protocols, while simultaneously investigating the underlying dynamics of initialisation. In this way, regardless of the fidelities achieved, important properties of the system can be determined and used to develop better protocols in the future.

The outline of this thesis is as follows. In Section 2, the theoretical foundation of this research is introduced. Most importantly, this section outlines the Lindbladian model which is used to determine the eigenstate populations in the steady state, and also introduces the theoretical measures used for initialisation. In Section 3, a brief overview of the experimental methods used to verify the model is given. In Section 4, experimental and simulated results for an inhomogeneous ensemble are analysed and compared, experimentally verifying an inhomogeneous protocol developed with the model. In Section 5, theoretical single-defect initialisation protocols are outlined, along with a thorough analysis of the spin-state dynamics of the system. Finally, in Section 6, the conclusions and outlook of this research are given.

2 Theoretical Overview

2.1 System Overview

The characterisation of the system, including the symmetry analysis and the derivation of the system Hamiltonian, was done by Gilardoni [72] (Chapters 2, 4-6) and collaborators in 2019-2021 for transition metal defects in silicon carbide. The theoretical foundation of this research is based on this characterisation.

2.1.1 Vanadium Defects in 4H-SiC: Energy and Spin-State Structure

This research focuses specifically on neutral charge state (V^{4+}) vanadium defects in 4H-SiC, a polytype of silicon carbide. Vanadium has a strongly localised 3d electron with a five-fold degeneracy. When a vanadium atom is substituted into a silicon lattice site in 4H-SiC, this five-fold degeneracy is first lifted by the defect-site crystal field potential with T_d symmetry, and then by the surrounding crystal field potential with C_{3v} symmetry. The crystal structure can be seen in Figure 2.1a. Finally spin-orbit (S-O) coupling completely lifts the degeneracy into five distinct S-O coupled states. With the inclusion of S-O coupling, the states then transform as the irreps of the double group $\overline{C}_{3v}$. The effect of the different crystal fields and S-O coupling on the electronic energy structure can be seen in Figure 2.1b. $A_{1,2}$ and E are irreps of C_{3v}, and Γ_4 and $\Gamma_{5,6}$ are irreps of $\overline{C}_{3v}$. The S-O coupled states are labelled in the community as, in ascending energy, GS1 (Γ_4), GS2 ($\Gamma_{5,6}$), ES1 ($\Gamma_{5,6}$), ES2 (Γ_4), and ES3 (Γ_4). GS and ES stand for ground state and excited state, respectively. Only GS1 and ES1 are considered in this research, due to their favourable energy structure and symmetry-related selection rules. Each S-O coupled state consists of a Kramers doublet (KD), which acts as an effective-spin $\tilde{S} = 1/2$ system with quantization along the crystal c axis. For the remainder of this thesis, the effective-spin states of the GS1 KD will be symbolically represented in the basis $\{|\uparrow\rangle, |\downarrow\rangle\}$ and the effective-spin states of the ES1 KD in the basis $\{|\nearrow\rangle, |\swarrow\rangle\}$. The slight shift in arrow direction between the two bases serves only as a label to distinguish the GS1 effective-spin basis from the ES1 effective-spin basis.

More than 99.7% of naturally occurring vanadium is ^{51}V [75], which has a nuclear spin $I = 7/2$ [76]. This nuclear spin I couples to the effective-spin $\tilde{S}$ to form an effective hyperfine structure $\tilde{F} = \tilde{S} + I$. This results in each S-O coupled state (i.e. GS1 and ES1) having 16 hyperfine levels, corresponding to eight hyperfine-mediated eigenstates in each of the effective-spin states ($\uparrow$, $\downarrow$, $\nearrow$, $\swarrow$) of the KD. This can be seen in Figure 2.2, which also shows the Zeeman splitting of the hyperfine-mediated eigenstates. Since each effective-spin state actually consists of 8 hyperfine-mediated eigenstates, each KD effective-spin state will be referred to as an effective-spin manifold. The energy spacing between the hyperfine levels is on the order of $10^{-8} - 10^{-7}$ eV ($10 - 100$ MHz) depending on the Zeeman splitting, while the energy spacing between GS1 and ES1 is on the order of 1 eV (~ 1278 nm). Since this is an optically-active transition, excitation (relaxation) between GS1 and ES1 will be referred to as optical excitation (relaxation) or optical driving. The cryostat used in experiment was operated at 2 K. The thermal energy supplied to the system is on the order of $k_B T \approx 10^{-4}$ eV, far smaller than the optical transition, but much larger than the hyperfine energy spacing. Therefore, at 2 K, there is sufficient thermal energy to cause mixing of a once initialised state.

2.1.2 System Hamiltonian and its Eigenstates

The Hamiltonians describing GS1 and ES1 are distinct due to their different S-O symmetries (GS1 transforms as Γ_4, ES1 transforms as $\Gamma_{5,6}$). A full description, and derivation, of the respective Hamiltonians can be found in Gilardoni [72] (Chapter 5). For use as a quantum memory, the
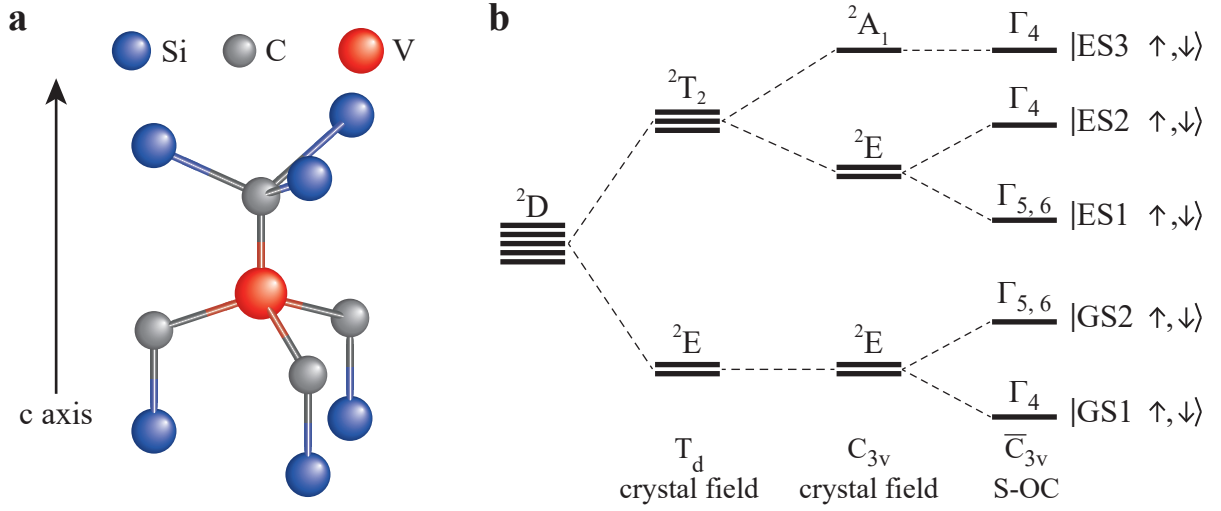
Figure 2.1: **a** Crystal structure of 4H-SiC with a V defect substituting a Si lattice site. The V and C atoms combined have a T_d symmetry, and the V, C, and Si atoms combined have a C_{3v} symmetry. The crystal c axis is parallel to the symmetry axis (i.e. the three-fold rotational axis) of C_{3v}. **b** The effect of symmetry on the electronic energy structure. The superscript 2 represents the two-fold degeneracy of each state arising from the electron spin. The strongly localised 3d electron (^{2}D) has a five-fold degeneracy (10 states when including the electron spin) which is split by the defect-site T_d symmetry into a ground orbital doublet ^{2}E and an excited orbital triplet $^2T_2$. The crystal field C_{3v} symmetry splits the excited triplet into a doublet ^{2}E and a singlet $^2A_1$. Finally, S-O coupling (S-OC in the figure) splits the ground and excited doublets, resulting in five distinct S-O coupled state. Each S-O state is a Kramers doublet (KD), which acts as an effective-spin $\tilde{S} = 1/2$ doublet. Only GS1 and ES1 are of interest in this research, with corresponding transition energy $\sim$ 1278.81 nm.

hyperfine-coupled vanadium system must be coherently controlled, and hence the hyperfine-mediated eigenstates must be accessible. As a result of the Zeeman interaction, applying a constant magnetic field splits the 16 hyperfine-mediated eigenstates of GS1 (and ES1), allowing for better accessibility. This can be seen in Figure 2.2. Furthermore, as the magnetic field increases, the eigenstate energy levels change as a result of the competing hyperfine and Zeeman interaction. This results in certain points where the transition energy between two eigenstates is stable with respect to minor fluctuations in the magnetic field (magnetic noise), an experimentally favourable quality. These are called zero first-order Zeeman shift (ZEFOZ) transitions or clock transitions (for their use in atomic clocks). It is therefore preferable for qubit candidates selected in an initialisation protocol to be ZEFOZ transitions.

Since there are two non-zero spins in the effective hyperfine interaction $\tilde{F} = \tilde{S} + I$, there are two Zeeman contributions to the Hamiltonian, an electronic Zeeman interaction and a nuclear Zeeman interaction. Denoting the hyperfine contribution as HF, the electronic ($\tilde{S}$) Zeeman contribution as Z:el, and the nuclear (I) Zeeman contribution as Z:nuc, the Hamiltonian for effective spin states transforming as Γ_4 and $\Gamma_{5,6}$ is given by

$$H_{\Gamma_x} = H^{eff}_{\text{HF}, \Gamma_x} + H^{eff}_{\text{Z:el}, \Gamma_x} + H^{eff}_{\text{Z:nuc}, \Gamma_x}, \tag{2.1}$$

where for $\Gamma_x = \Gamma_4$

$$H^{eff}_{\text{HF}, \Gamma_4} = a_{\parallel, \Gamma_4} \tilde{S}_z I_z + a_{\perp, \Gamma_4}(\tilde{S}_+ I_+ + \tilde{S}_- I_-) + Q_{zz} I_z^2$$
$$H^{eff}_{\text{Z:el}, \Gamma_4} = -\mu_B \big(g_{\parallel, \Gamma_4} B_z \tilde{S}_z + g_{\perp, \Gamma_4}(B_x \tilde{S}_x + B_y \tilde{S}_y) \big) \tag{2.2}$$
$$H^{eff}_{\text{Z:nuc}, \Gamma_4} = -\mu_N g_n (B_z I_z + B_x I_x + B_y I_y)$$

and for $\Gamma_x = \Gamma_{5,6}$

$$
\begin{aligned}
H_{\text{HF}, \Gamma_{5,6}}^{eff} &= (a_{\parallel, \Gamma_{5,6}}\tilde{S}_z + a_{\perp, \Gamma_{5,6}}\tilde{S}_x)I_z + Q_{zz}I_z^2 \\
H_{\text{Z:el}, \Gamma_{5,6}}^{eff} &= -\mu_B g_{\parallel, \Gamma_{5,6}}B_z\tilde{S}_z \\
H_{\text{Z:nuc:}, \Gamma_{5,6}}^{eff} &= -\mu_N g_n(B_zI_z + B_xI_x + B_yI_y).
\end{aligned}
\tag{2.3}
$$

$\tilde{S}_{x,y,z}$, and $I_{x,y,z}$ are the effective-spin and nuclear spin operators (defined in Appendix B.I), respectively, and (B_x, B_y, B_z) is the applied static magnetic field vector. The $\hat{z}$ axis is taken to be parallel with the crystal c axis. Here a is a term characterising the hyperfine interaction, g is the electronic g-factor, g_n is the nuclear g-factor, μ_B is the Bohr magneton, and μ_N is the nuclear magneton. The term $Q_{zz}I_z^2$ characterises the nuclear electric quadrupole moment, with Q_{zz} being the strength of the quadrupole interaction experienced by the vanadium nucleus due to a $\hat{z}$-direction electric-field gradient [62, 77]. The factors a and g used in this research were determined by Wolfowicz et al [61]. The exact values can be found in Appendix B.I. Parallel and perpendicular terms are with respect to the crystal c axis, which is also the C_{3v} symmetry axis. One important note is that while symmetry allows for perpendicular magnetic fields to drive transitions between spin manifolds, vanadium has an accidental $g_\perp \approx 0$.[1] Therefore, a magnetic field parallel to the crystal c axis results in the strongest Zeeman splitting. A parallel magnetic field is used, in both experiment and simulation, to produce the Zeeman splitting.

In general, the system is not in a pure state but a mixed state, as systems in thermal equilibrium tend towards mixed states. Pure states, including coherent superpositions, can be represented by a single ket vector $|\psi\rangle$. Mixed states however, are a statistical ensemble of pure states. In this way, they can only be described by a density matrix ρ (density operator defined in the basis $\{|\phi_i\rangle\}$)

$$
\rho = \sum_n p_n |\psi_n\rangle \langle\psi_n|
\tag{2.4}
$$

where $\{|\psi_n\rangle\}$ are pure states of the system, p_n is the statistical weight associated with the pure state $|\psi_n\rangle$ ($\sum_n p_n = 1$), and the (weighted) sum goes over all possible pure states that the system can be in. The diagonal terms $\rho_{ii} \equiv P_i$ of a density matrix are called populations, as they represent the probability to find the system in the basis state $|\phi_i\rangle$, whereas the off-diagonal terms are called coherences, and quantify the magnitude of coherence between the basis states. Upon application of a laser resonant with the GS1-ES1 transition, the hyperfine-coupled vanadium system is described by a 32×32 density matrix, as there are 16 energy eigenstates in both GS1 and ES1. The 16 energy eigenstates of GS1 labelled $\{|g_i\rangle\}$ and of ES1 labelled $\{|e_i\rangle\}$, with $i = 1, \ldots, 16$, are given by the eigenvalue equations

$$
\begin{aligned}
H_{\Gamma_4}|g_i\rangle &= E_{g_i}|g_i\rangle, \\
H_{\Gamma_{5,6}}|e_i\rangle &= E_{e_i}|e_i\rangle.
\end{aligned}
\tag{2.5}
$$

The states $\{|g_i\rangle, |e_i\rangle\}$ form the basis of the 32×32 density matrix. E_{g_i} is the energy of state $|g_i\rangle$, and E_{e_i} is the energy of state $|e_i\rangle$. For brevity, the bra-ket notation will sometimes be omitted when describing the eigenstates, such that g_i means $|g_i\rangle$. These (pure) eigenstates are linear combinations of the effective-spin basis states $\{|g, m_{\tilde{S}}, m_I\rangle\}$ for GS1 and $\{|e, m_{\tilde{S}}, m_I\rangle\}$ for ES1, with projection along the crystal c axis ($\hat{z}$ axis). This effective-spin state mixing of the eigenstates is primarily due

---

[1]Note that for states transforming as $\Gamma_{5,6}$ symmetry dictates that $g_\perp = 0$, while for states transforming as Γ_4, $g_\perp$ is near zero. For the purpose of this work however, where static magnetic fields below 1 T are used, $g_\perp$ can be set to zero for both Γ_4 and $\Gamma_{5,6}$ states. For more information, refer to Gilardoni [72] (Chapters 5, 6).
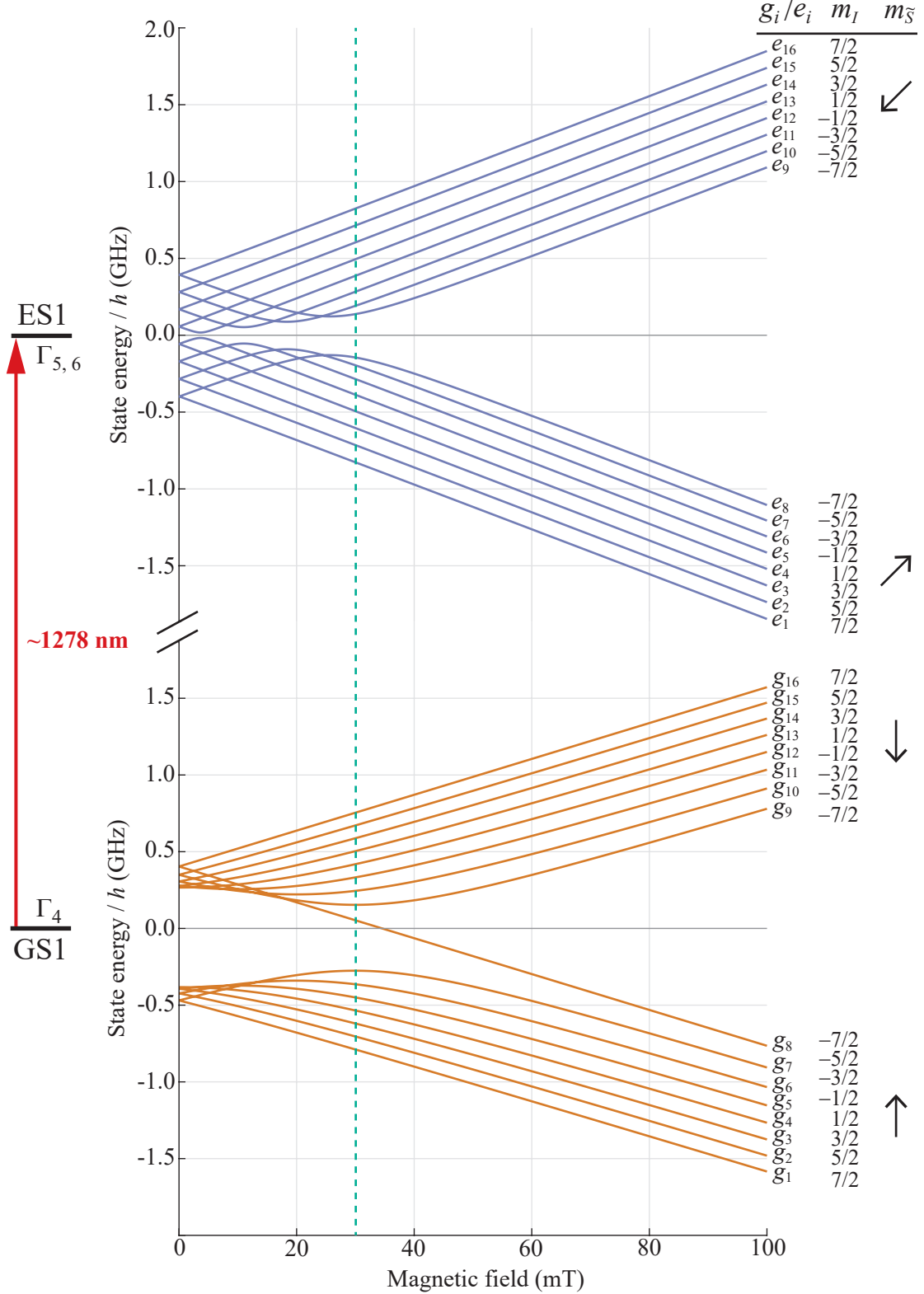
Figure 2.2: Zeeman splitting of the hyperfine-mediated eigenstates of GS1 (Γ_4) and ES1 ($\Gamma_{5,6}$). The plot shows the energy of each eigenstate (with respect to the corresponding S-O state, GS1 or ES1) as a function of the magnetic field strength of an applied static magnetic field parallel to the crystal c axis. The GS1 (ES1) eigenstates are labelled g_i (e_i) for $i = 1, \ldots, 16$. At $\gtrsim 30$ mT (dashed green line in figure), the system Hamiltonian is dominated by the electronic Zeeman interaction. In this magnetic field regime, each eigenstate can be approximated by a single spin state $|m_{\tilde{S}}, m_I\rangle$. The spin-state values $m_{\tilde{S}}$, m_I corresponding to each eigenstate in this regime are given next to the eigenstate labels.

to the nuclear electric quadrupole perturbation $Q_{zz}I_z$ to the Hamiltonian. Here, g and e are added as a label in the ket to distinguish between GS1 and ES1 effective-spin states. The eigenstates can then be written as

$$g_i = \sum_k C_k^g \left| g, \ m_{\tilde{S}}, \ m_I \right\rangle,$$

$$e_i = \sum_k C_k^e \left| e, \ m_{\tilde{S}}, \ m_I \right\rangle.$$

Here the sum over k represents the summing over the different effective-spin states (i.e. summing over combinations of $m_{\tilde{S}} = -1/2, \ 1/2$ and $m_I = -7/2, \ -5/2, \ldots, \ 7/2$). The coefficients $C_k^{g, \ e}$ are the probability amplitudes of the kth state given by a specific $m_{\tilde{S}}$ and m_I. The sum of the probability densities is $\sum_k |C_k^g|^2 = \sum_k |C_k^e|^2 = 1$. The probability amplitudes $C_k^{g, \ e}$ are magnetic field dependent due to the Zeeman terms in the Hamiltonian. In the electronic Zeeman dominated regime ($B \gtrsim 30$ mT), the effective spin $\tilde{S}$ is strongly aligned with the external field. In this magnetic field regime, the probability amplitudes $C_k^{g, \ e}$ tend to zero except for one value of k; the eigenstates can then be approximated by the effective-spin state associated with k. The state with the lowest energy, g_1, corresponds to the spin state $|\uparrow, \ 7/2\rangle$. This is because an effective spin aligning with the magnetic field minimises the energy,[2] and a nuclear spin aligning with the effective spin further minimises the energy. The associated effective-spin states of the other eigenstates in the high-field limit can be seen in Figure 2.2.

While the eigenstates of the system are (necessarily) pure states, the full state description of the hyperfine-coupled vanadium system in equilibrium is given by a density matrix ρ. As will be seen, the model calculates the populations (diagonal terms of ρ) in the steady state. One assumption of the model is that in steady-state initialisation, the coherences disappear. This is not entirely true, as coherent population trapping (CPT) can occur. CPT happens when the transitions $g_i - e_j$ and $g_k - e_j$ are driven simultaneously, and can lead to coherence between the states g_i and g_k. As will be seen, at 2 K, these driving schemes (denoted as Λ-schemes) do not initialise the system, and CPT is therefore not included in the model. At lower temperatures however, Λ-schemes do appear. This is discussed further in Section 5.3. Ignoring CPT means that the density matrix describing the hyperfine-coupled vanadium system is purely diagonal and can be written as

$$\rho = \text{diag}(\vec{P}) = \text{diag}\left(\left(\vec{P}_g, \ \vec{P}_e\right)\right) \tag{2.6}$$

where $\vec{P} = \left(\vec{P}_g, \ \vec{P}_e\right)$, and $\vec{P}_g = (P_{g_1}, \ldots, P_{g_{16}})$ and $\vec{P}_e = (P_{e_1}, \ldots, P_{e_{16}})$ are the population vectors of GS1 and ES1 respectively, with P_{g_i} (P_{e_i}) being the population of state g_i (e_i).

2.1.3 Inhomogeneous Broadening of GS1−ES1 Transition

Each defect is situated in a different part of the 4H-SiC crystal lattice and feels differing electrostatic inhomogeneities arising from lattice imperfections and other environmental factors. These inhomogeneities result in unique changes in the energy structure of the different defects, and as such causes an inhomogeneous broadening of the GS1−ES1 optical-transition linewidth (i.e. the transition energy). In the sample studied here, the inhomogeneous broadening is roughly 20 GHz. The consequence of this is that the same laser frequency can be resonant with different transitions between the defects, and the overall energy resolution decreases. With two lasers the hyperfine-mediated energy levels of

---

[2]Above 30 mT, the electronic Zeeman contribution to the Hamiltonian is on average 10^3 times as much as the nuclear Zeeman contribution, so the effective electronic spin plays a bigger role than the nuclear spin in minimising energy.

GS1 can still be resolved. While the actual inhomogeneity is ~ 20 Ghz, an effective inhomogeneity Δ, on the order of a few GHz, was applied in the model. Further explanation on the effective inhomogeneity can be found in Appendix A.I, and more information on how the inhomogeneities were implemented in the model can be found in Appendix B.1.

The case where there is no inhomogeneous broadening of the GS1$-$ES1 transition linewidth is termed the single-defect case. In this research only the inhomogeneous case could be studied experimentally. Both the inhomogeneous and single-defect cases were theoretically modelled. When initialising with two lasers in the inhomogeneous case, only the frequency of one laser is scanned over while the other laser is kept fixed. This is because it is not the individual frequencies that matter, but their difference, since the inhomogeneities cause one laser frequency to be resonant with several different transitions at once within the ensemble. In the single-defect case however, the laser frequencies must be considered individually. With the appropriate technique, V defects in SiC are individually accessible [78].

2.2   Relaxation Processes

Work done by Gilardoni et al. [79] approximated the system spin relaxation within a KD to four effective-spin processes. The four processes happen both in GS1 and ES1 but with differing relative strengths, and are dependent on environmental factors (e.g. magnetic field, temperature). The processes are the electronic spin flip (ESF), the nuclear spin flip (NSF), the flip-flop (FF), and the $\hat{z}$-axis flip-flop (FFz). The electronic spin flip is a change in the effective-spin of a state (e.g. $|\uparrow\rangle \Rightarrow |\downarrow\rangle$). The nuclear spin flip is a change in m_I of a state, with $\Delta m_I = \pm 1$ changes having the strongest relaxation pathways. The flip-flop and $\hat{z}$-axis flip-flop are processes in which both the effective electronic spin and nuclear spin change. The difference between the two processes being that the operators mediating the flip-flop are the ladder operators S_+, S_-, I_+, I_- while the $\hat{z}$-axis flip-flop is mediated by the projection operators S_z, I_z. This means that in the high-field limit, where the spins are strongly aligned with the projection axis ($\hat{z}$-axis), the projection operators have a much weaker effect on the quantized spins as compared to the ladder operators. In this thesis the operators associated with these relaxation processes will be denoted by $\mathcal{O}_{\text{NSF}}$, $\mathcal{O}_{\text{ESF}}$, $\mathcal{O}_{\text{FF}}$, and $\mathcal{O}_{\text{FFz}}$, with the subscript corresponding to the abbreviations in the brackets above. The operator for optical relaxation (from ES1 to GS1) is denoted by $\mathcal{O}_{\text{opt}}$. The operators are defined in Appendix B.I.

It must be noted that in terms of the formulation developed above, the four spin processes are all effective processes, even at the eigenstate level. Relaxation between two eigenstates is mediated by all four processes, as all the eigenstates are composed of effective-spin states. For example, at 0 mT, g_9 can be approximated by $|\Psi\rangle = 0.57\big(|\uparrow, -1/2\rangle - |\downarrow, 1/2\rangle\big) + 0.4\big(|\downarrow, -3/2\rangle - |\uparrow, 3/2\rangle\big)$ with $|\langle g_9|\Psi\rangle|^2 > 0.98$. It also has a strong relaxation pathway with g_{11}, which can be approximated by $|\Phi\rangle = 0.64\big(|\uparrow, -3/2\rangle - |\downarrow, 3/2\rangle\big) + 0.3\big(|\downarrow, -5/2\rangle - |\uparrow, 5/2\rangle\big)$ with $|\langle g_{11}|\Phi\rangle|^2 > 0.999$. Thus, going from g_9 to g_{11} involves a combination of spin processes, and is not as simple as stating that it is a pure electronic spin flip or flip-flop process. Fortunately, as mentioned, in the electronic Zeeman dominated regime the eigenstates can be represented by one effective-spin state, which makes it considerably easier to determine the relevant processes.

2.3   Lindbladian Model

As mentioned prior, the system is calculated in the steady state, that is

$$\dot{\rho} = 0. \tag{2.7}$$

Since it is assumed that there are no coherences, so that ρ is only composed of diagonal terms (populations), ρ can be replaced with a 32-entry column vector $\vec{\rho}_{\text{diag}}$. Explicitly

$$\rho = \text{diag}(\vec{P}) \rightarrow \vec{\rho}_{\text{diag}} = \vec{P}^{\text{T}} = (P_{g_1},\ P_{g_2}, \ldots, P_{e_{16}})^{\text{T}} = (P_1,\ P_2,\ \ldots,\ P_{32})^{\text{T}}. \tag{2.8}$$

The subscripts g_j, e_j have been replaced with $i = 1, \ldots, 32$ for brevity. Replacing the 32×32 matrix ρ with a 32-entry vector $\vec{\rho}_{\text{diag}}$ makes it more (computationally) efficient to solve for the populations. In this way, Eq. (2.7) is a system of 32 linear differential equations (DEs). The evolution of an open quantum system (a system that interacts with its environment) is governed by the master Lindblad equation [80], given by

$$\dot{\rho} = \mathcal{L}\rho \tag{2.9}$$

where $\mathcal{L}$ is the Lindbladian. For the system studied here, the Lindbladian $\mathcal{L}$ can be represented by a 32×32 matrix M. Eqs. (2.7), (2.8), and (2.9) can then be combined to give

$$M\vec{\rho}_{\text{diag}} = \vec{0} \tag{2.10}$$

where $\vec{0}$ is a 32-entry column vector of zeros. Eq. (2.10) is the foundation of the simulated model used in this research. Now, instead of 32 linear DEs, Eq. (2.10) is a system of 32 linear equations. Eq. (2.10) can be rearranged to give

$$\vec{\rho}_{\text{diag}} = M^{-1}\vec{0}.$$

After normalisation of the populations $\sum_i P_i = 1$ for $i = 1,\ 2, \ldots,\ 32$, the above equation can be solved for ρ. The Lindbladian matrix M takes the general form (a derivation of M, and further explanation on the normalisation of the populations, can be found in Appendix A.II)

$$M = \begin{pmatrix} \begin{matrix} -\Omega - \gamma_g & +\gamma_g & \cdots \\ +\gamma_g & \ddots & \\ \vdots & & \ddots \end{matrix} & +\Gamma \\ \hline +\Omega & \begin{matrix} -\Gamma - \gamma_e & +\gamma_e & \cdots \\ +\gamma_e & \ddots & \\ \vdots & & \ddots \end{matrix} \end{pmatrix} \equiv \left(\begin{array}{c|c} M_g & M_\Gamma \\ \hline M_\Omega & M_e \end{array} \right) \tag{2.11}$$

where Ω are driving rates, Γ are the optical relaxation rates between excited and ground eigenstates, and γ_g (γ_e) are relaxation rates between ground (excited) eigenstates. The Lindbladian matrix is split into four 16×16 matrices. Starting from the upper left and going clockwise, these represent the GS1 dynamics (M_g), optical relaxation from ES1 to GS1 (M_Γ), optical driving from GS1 to ES1 (M_Ω), and the ES1 dynamics (M_e). The last step in solving ρ is to now find the rates Ω, Γ, and γ. This was done in a semi-empirical manner. The probability of an x-mediated relaxation (with x an effective-spin process) between two states $|i\rangle$, $|j\rangle$ is given by the transition probability $|\langle j|\mathcal{O}_x|i\rangle|^2$, with $\mathcal{O}_x$ a dimensionless operator corresponding to the effective-spin process x.[3] In an open system, this transition probability is affected by environmental effects which are not considered by the Hamiltonian nor the operator (which are both derived for a closed system). To incorporate these environmental effects, and especially temperature, the rate coefficient $\mathcal{R}_x$ of the effective-spin process x, can be multiplied with the respective transition probability. The rate coefficient is an experimentally determined parameter. As mentioned, there are four processes in GS1 and ES1

---

[3]Note that the dimensionless operators $\mathcal{O}_x$ only provide information on the strength of an effective-spin process at a very generic level. They do not give any quantitative physical information on a process, as opposed to, for example, the electric dipole moment (with SI units Coulomb-metre).

which govern spin transitions, with operators $\mathcal{O}_{\text{ESF}}$, $\mathcal{O}_{\text{NSF}}$, $\mathcal{O}_{\text{FF}}$, and $\mathcal{O}_{\text{FFz}}$. Therefore, the relaxation rates $\gamma_g \equiv \gamma_{g_i - g_j}$ from g_i to g_j and $\gamma_e \equiv \gamma_{e_i - e_j}$ from e_i to e_j are given by

$$
\begin{aligned}
\gamma_{g_i - g_j} = & \mathcal{R}_{\text{ESF}}^{g} |\langle g_j | \mathcal{O}_{\text{ESF}} | g_i \rangle|^2 + \mathcal{R}_{\text{NSF}}^{g} |\langle g_j | \mathcal{O}_{\text{NSF}} | g_i \rangle|^2 + \\
& \mathcal{R}_{\text{FF}}^{g} |\langle g_j | \mathcal{O}_{\text{FF}} | g_i \rangle|^2 + \mathcal{R}_{\text{FFz}}^{g} |\langle g_j | \mathcal{O}_{\text{FFz}} | g_i \rangle|^2,
\end{aligned}
\tag{2.12}
$$

$$
\begin{aligned}
\gamma_{e_i - e_j} = & \mathcal{R}_{\text{ESF}}^{e} |\langle e_j | \mathcal{O}_{\text{ESF}} | e_i \rangle|^2 + \mathcal{R}_{\text{NSF}}^{e} |\langle e_j | \mathcal{O}_{\text{NSF}} | e_i \rangle|^2 + \\
& \mathcal{R}_{\text{FF}}^{e} |\langle e_j | \mathcal{O}_{\text{FF}} | e_i \rangle|^2 + \mathcal{R}_{\text{FFz}}^{e} |\langle e_j | \mathcal{O}_{\text{FFz}} | e_i \rangle|^2.
\end{aligned}
\tag{2.13}
$$

As mentioned, the operators are defined in Appendix B.I. It is generally difficult to individually determine the GS1 relaxation rates $\gamma_{g_i - g_j}$, especially for a 16-level system. What is typically measured instead is some weighted average of these rates $\bar{\gamma}_g$, with the inverse of $\bar{\gamma}_g$ designated the spin-relaxation time $T_1 \sim 1/\bar{\gamma}_g$. The effective-spin relaxation rate coefficients $\mathcal{R}^g$, $\mathcal{R}^e$ were determined by optimising simulated two-laser spectra with experimental two-laser spectra for a range of magnetic fields between $0 - 300$ mT at 2 K (Appendix B.I). Therefore, these effective-spin rate coefficients are only valid at 2 K, and are referred to as the standard rate coefficients. They were also kept constant throughout the magnetic field range. The implications of this can be found in Appendix C.II. The optical relaxation rate $\Gamma_{e_i - g_j}$ between state e_i to g_j (including $i = j$) is given by

$$
\Gamma_{e_i - g_j} = \mathcal{R}_{\text{opt}}^{\text{rlx}} |\langle g_j | \mathcal{O}_{\text{opt}}^{\text{rlx}} | e_i \rangle|^2
\tag{2.14}
$$

where the subscript 'opt' stands for optical, and the superscript 'rlx' stands for relaxation. The optical relaxation rate coefficient $\mathcal{R}_{\text{opt}}^{\text{rlx}} = \Gamma_{\text{opt}}$, the optical linewidth. The driving rates $\Omega_{g_i - e_i}$ between state g_i and e_j are derived in a similar way, but the effects of a finite optical linewidth must be incorporated. This is done by introducing a Lorentzian probability density function (PDF) $f(\omega; \omega_0, \Gamma_{\text{opt}})$, where ω is the laser frequency, ω_0 is the transition (resonance) frequency of the $g_i - e_j$ transition, and the optical linewidth Γ_{opt} is ~ 10 MHz (an optical lifetime of ~ 100 ns, fitted from experimental data [60, 61]) for vanadium defects in 4H-SiC. The Lorentzian PDF is given by

$$
f(\omega; \omega_0, \Gamma_{\text{opt}}) = \frac{1}{\pi} \frac{\Gamma_{\text{opt}}}{(\omega_0 - \omega)^2 + \Gamma_{\text{opt}}^2}.
\tag{2.15}
$$

The driving rate $\Omega_{g_i - e_i}$ is then given by

$$
\Omega_{g_i - e_i} = f(\omega; \omega_0, \Gamma) \cdot \left(\mathcal{R}_{\text{opt}}^{\text{drv}} |\langle e_j | \mathcal{O}_{\text{opt}}^{\text{drv}} | g_i \rangle|^2 \right).
\tag{2.16}
$$

The rate coefficient $\mathcal{R}_{\text{opt}}^{\text{drv}}$ reflects the power of the incident laser. The populations are calculated as a function of the laser detunings $\delta_{1,2} = \omega_0 - \omega_{1,2}$ with respect to the GS1$-$ES1 transition energy, per magnetic field $\vec{B}$. In the inhomogeneous case, since the inhomogeneities cause one frequency to be resonant with several different transitions at once, it is the frequency difference of the two lasers that is the relevant quantity. The populations are then a function of the frequency difference (also referred to as the detuning) $\Delta\delta = \delta_1 - \delta_2 = \omega_1 - \omega_2$ between the two lasers. This can be seen schematically in Figure 2.3. The detunings δ_1 and δ_2 will sometimes be referred to as δ_F and δ_S if one laser is kept fixed in frequency (δ_F) while the other is scanned (δ_S). Typically in the inhomogeneous case one of the lasers is kept fixed and is not detuned, $\delta_F = 0$, since this will be resonant with several transitions anyway. The detuning $\Delta\delta$ then reduces to $\Delta\delta = \delta_S$. The relaxation rates Eqs. (2.12)-(2.14) are detuning independent and are constant for a specific magnetic field strength.
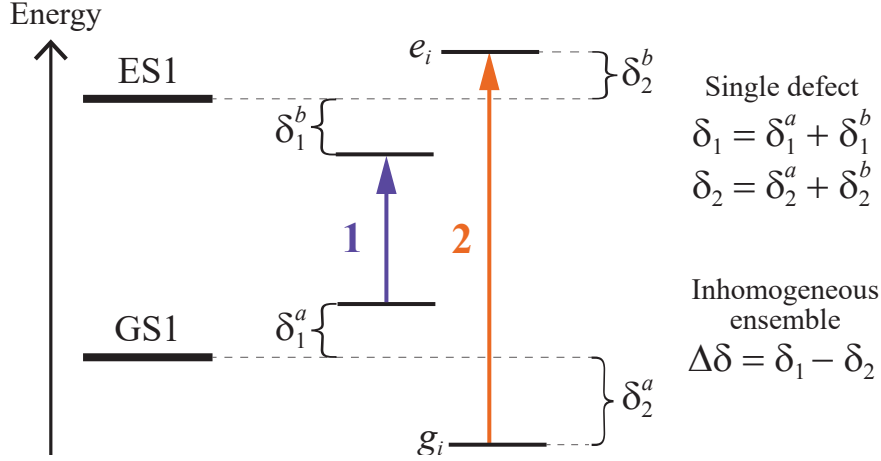
Figure 2.3: Guide on detunings used in this thesis. The detuning δ_2^a (δ_2^b) corresponds to the energy E_{g_i} (E_{e_i}) of state g_i (e_i). For a single defect, the two laser detunings δ_1, δ_2 are considered separately. For an inhomogeneous ensemble however, it is their difference $\Delta\delta = \delta_1 - \delta_2$ that is the relevant quantity. Typically, one laser is kept fixed at $\delta_2 = 0$, so the inhomogeneous ensemble detuning $\Delta\delta$ reduces to $\Delta = \delta_1$. In this driving scheme, laser **1** is the short leg, and laser **2** is the long leg. Note that in this detuning description, the 1278 nm optical transition energy is not included.

2.3.1 Circular Polarisation

It should be noted that there are two optical operators, $\mathcal{O}_{\mathrm{opt}}^{\mathrm{drv}}$ and $\mathcal{O}_{\mathrm{opt}}^{\mathrm{rlx}}$. These operators are actually equal if the driving fields are linearly polarised, that is

$$\mathcal{O}_{\mathrm{opt}}^{\mathrm{drv:\ linear}} = \mathcal{O}_{\mathrm{opt}}^{\mathrm{rlx}} = \begin{pmatrix} \mathbb{I}_8 & 0_{8,8} \\ 0_{8,8} & \mathbb{I}_8 \end{pmatrix} = \mathbb{I}_{16}.$$

The linear driving operator (and optical relaxation operator) favours optical transitions in which the spin ($m_{\tilde{S}}$, m_I) is conserved, but still weakly allows transitions where the spin is not conserved (due to effective-spin-state mixing in the eigenstates). The upper $\mathbb{I}_8$ matrix acts on states in the lower spin manifolds ($\uparrow$ in GS1, $\nearrow$ in ES1), while the lower $\mathbb{I}_8$ matrix acts on states in the upper spin manifold ($\downarrow$ in GS1, $\swarrow$ in ES1). Since linearly-polarised light is a superposition of the two angular momentum states (or polarisation states) of light, it can access transitions in both effective-spin manifolds. However, circularly-polarised light is composed of purely one angular momentum state, and therefore heavily suppresses transitions in one of the spin manifolds. This can be represented in the circularly-polarised driving operators $\mathcal{O}_+$ and $\mathcal{O}_-$ with

$$O_+ = \begin{pmatrix} \mathbb{I}_8 & 0_{8,8} \\ 0_{8,8} & 0_{8,8} \end{pmatrix}$$

$$O_- = \begin{pmatrix} 0_{8,8} & 0_{8,8} \\ 0_{8,8} & \mathbb{I}_8 \end{pmatrix}.$$

The choice of $+$, $-$ is physically arbitrary, but once defined must be kept consistent. Using the handedness convention of the quarter-wave plate used in experiment [81], it was experimentally determined (Section 4.2) that $\mathcal{O}_+$ corresponds to left-hand circularly polarised, and $\mathcal{O}_-$ to right-hand circularly polarised. The operator $\mathcal{O}_+$ amplifies $\uparrow \Longrightarrow \nearrow$ transitions and suppresses $\downarrow \Longrightarrow \swarrow$ transitions, and vice versa for $\mathcal{O}_-$. In terms of notation, the polarisation $\sigma_\pm$ corresponds to the operator $\mathcal{O}_\pm$. Since the linearly-polarised driving operator and optical relaxation operator are the same, they will both be denoted as $\mathcal{O}_{\mathrm{opt}}$. A schematic of the selection rules can be found in Appendix A.III.

2.4 Effective-Spin Driving (ESD)

After the system is initialised, two of the GS1 eigenstates are driven by an applied oscillating magnetic or electric field. If these eigenstates are driven coherently, it effectively creates a qubit. However, incoherent driving can still result in measurable resonance. The operator driving these effective-spin transitions will be denoted as the effective-spin driving (ESD) operator $\mathcal{O}_{\mathrm{esd}}$. Any field driving transitions between eigenstates mediate the transitions via the four effective-spin processes (ESF, NSF, FF, and FFz). Thus, the effective-spin driving operator $\mathcal{O}_{\mathrm{esd}}$ can be defined as

$$\mathcal{O}_{\mathrm{esd}} = \mathcal{O}_{\mathrm{ESF}} + \mathcal{O}_{\mathrm{NSF}} + \mathcal{O}_{\mathrm{FF}} + \mathcal{O}_{\mathrm{FFz}}$$

and the ESD transition probability is given by

$$|\langle g_j|\mathcal{O}_{\mathrm{esd}}|g_i\rangle|^2 = \left| \langle g_j|\mathcal{O}_{\mathrm{ESF}} + \mathcal{O}_{\mathrm{NSF}} + \mathcal{O}_{\mathrm{FF}} + \mathcal{O}_{\mathrm{FFz}}|g_i\rangle \right|^2$$

$$= \left| \langle g_j|\mathcal{O}_{\mathrm{ESF}}|g_i\rangle + \langle g_j|\mathcal{O}_{\mathrm{NSF}}|g_i\rangle + \langle g_j|\mathcal{O}_{\mathrm{FF}}|g_i\rangle + \langle g_j|\mathcal{O}_{\mathrm{FFz}}|g_i\rangle \right|^2.$$

It was found that pure electronic spin flip transitions $\Delta m_{\tilde{S}} = 1$, $\Delta m_I = 0$ either had ESD probabilities which were too low, or neither state in the transition could be well initialised. Thus, only states with $\Delta m_I \neq 0$ were subsequently analysed. Effective-spin driving between states with $\Delta m_I \neq 0$ is a hyperfine-mediated process, and as such both magnetic dipole and electrical quadrupole transitions are possible (higher multipole transitions are also possible, but are very weak). In general, transitions strongly mediated by a $\Delta m_I = 1$ effective-spin process are magnetic dipole transitions, whereas $\Delta m_I = 2$ are electric quadrupole transitions. This means that both magnetic and electric field driving is possible, depending on the transition. What also needs to be considered is the orientation of the driving field, whether parallel or perpendicular to the spin-quantisation axis (which is parallel to the crystal c axis upon application of a parallel static B field). Due to the $g_\perp \approx 0$, perpendicular magnetic fields are not efficient in driving effective-spin transitions. In experiment then, an oscillating magnetic field parallel to the crystal c axis is used. For further information on electric field driving, refer to Appendix C.VI.

2.5 Initialisation: Fidelity and Population Contrast

Before an initialisation protocol can be developed, a quantitative definition of initialisation must be given. Ultimately, initialisation means preparing the system into a pure quantum state, and specifically in the context of this work, an eigenstate of GS1. In terms of the 32×32 density matrix ρ, this means going from the mixed state ρ (with nonzero populations along the diagonal) to a pure state σ, where there is only one nonzero population equal to 1. Since this population is associated with an effective-spin state, initialisation in this way is also commonly called spin polarisation, as the system is polarised into one (effective-)spin state. The question then is, how close is the mixed state ρ to the pure state σ. To answer this, it is useful to introduce the concept of fidelity $F(\rho,\,\sigma)$ defined as [82]

$$F(\rho,\,\sigma) = \mathrm{Tr}\left(\sqrt{\sqrt{\rho}\sigma\sqrt{\rho}} \right).$$

The fidelity is symmetric $F(\rho,\,\sigma) = F(\sigma,\,\rho)$ and reduces to the state overlap $F = \langle\psi_\rho|\psi_\sigma\rangle$ when ρ and σ are pure states. It is a measure of the distance between two quantum states, such that when $\rho = \sigma$, $F(\rho,\,\sigma) = 1$. When working with density matrices without coherences, and comparing them to pure eigenstates as is done here, the fidelity of an initialised state ρ and eigenstate g_i is simply given by

$$F(\rho,\,g_i) = \sqrt{P_{g_i}} \tag{2.17}$$

where P_{g_i} is the population of eigenstate g_i in ρ. A derivation of Eq. (2.17) can be found in Appendix A.IV. With a quantitative measure for initialisation now defined, an initialisation approach can be developed. While it is important that high-fidelity initialisation into a GS1 eigenstate g_i is achieved, g_i also has to be coherently driven with some other eigenstate g_j. In general, the higher the fidelity, the higher the population of one particular eigenstate. However, there is no certainty that initialisation with a fidelity of $F > \sqrt{0.5}$ can be achieved, meaning that the population of the two relevant eigenstates can still be near equal. For resonant (and coherent) driving, if two eigenstates have near equal populations, the measured signal will be very low. Thus, it is not just the fidelity that is important when initialising, but also the absolute difference in population between the two coherently driven states - the population contrast. The population contrast between the states g_i and g_j is given by

$$\Delta P(g_i, \, g_j) = |P_{g_i} - P_{g_j}|. \tag{2.18}$$

In this thesis the population contrast ΔP is given as a percentage for clarity. For example, a population contrast of $\Delta P(g_i, \, g_j) = |0.62 - 0.29| = 0.33$ is written as $\Delta P = 33\%$. In this example, the state fidelities are $F(\rho, \, g_i) = \sqrt{0.62} \approx 0.79$ and $F(\rho, \, g_j) = \sqrt{0.29} \approx 0.54$. Besides the population contrast ΔP, the effective-spin driving (ESD) probability also has to be considered. For example, if the states g_i and g_j were initialised with a population contrast of $\Delta P > 90\%$, but the ESD transition probability $|\langle g_j|\mathcal{O}_{esd}|g_i\rangle|^2$ is very small, then the states cannot be resonantly driven (and hence neither coherently). To incorporate this, a new measure is needed: the Useful Spin-Resonance Number (USRN or USR number). The USRN is an ad hoc measure defined as

$$\text{USRN}(g_i, \, g_j) = |\langle g_j|\mathcal{O}_{\text{esd}}|g_i\rangle|^2 \cdot \Delta P(g_i, \, g_j). \tag{2.19}$$

The USRN was used to find promising points of initialisation for experimental verification. It turns out however, that when attempting to initialise for coherent driving, ΔP holds more importance than $|\langle\mathcal{O}_{\text{esd}}\rangle|^2$, and consequently the USRN is not a reliable measure. This is because a strong ESD matrix element $\langle g_j|\mathcal{O}_{\text{esd}}|g_i\rangle$ does not only facilitate strong driving, but also implies strong relaxation between the states g_i and g_j. Hence, a very high ESD transition probability can result in a low population contrast $\Delta P(g_i, \, g_j)$. This is further discussed in Appendix C.V. The USRN is still mentioned here however, as it was an integral part of the experimental approach.

3 Experimental Methods & Approach

To reinforce the credibility of the theoretical single-defect initialisation protocols (Section 5), experimental verification of a theoretical protocol was conducted. Simulated results showed that the system could initialise very well into g_8 (and g_{16}), with maximum fidelities of $\gtrsim 0.9$ in the single-defect case, and ~ 0.1 in the inhomogeneous case (which is still significant for an inhomogeneous ensemble). Furthermore, since ODMR had been previously measured between g_6 and g_8 [62] the $g_6 - g_8$ transition was chosen as a qubit candidate. A theoretical initialisation approach was developed as follows. The USRN was calculated for $g_6 - g_8$ between 0 and 50 mT in 1 mT steps and for laser detunings in the range of $100 - 900$ MHz (started from 100 MHz due to experimental limitations). This was done for both the inhomogeneous and single-defect case. The laser detunings $(\delta_1,\ \delta_2)$ are considered separately in the single-defect case, while in the inhomogeneous case one laser is kept fixed ($\delta_F = 0$) while the other is scanned over the detuning δ_S (see Figure 2.3 for further explanation). After experimental measurements were taken, it was discovered that the USRN is not a good measure for initialisation and subsequent coherent driving. Therefore, when developing the single-defect initialisation protocols, the population contrast ΔP was used instead (see Section 2.5 and Appendix C.V for more information). Two lasers were used for initialisation as it is standard for most quantum optics laboratories and also convenient for commercial applications. Using one laser is not sufficient to resolve hyperfine structure in an inhomogeneous ensemble. Even in the single-defect case, one-laser initialisation will generally result in lower contrast as there is less control over the system. Spectral diffusion can also affect the one-laser resolution, but it is possible to mitigate these effects [83]. Restrictions of allowed $g_6 - g_8$ transition energies were applied due to the effective range of the microwave antenna ($200 - 600$ MHz), which applied the coherent driving (microwave) field. Ultimately, 40 mT was chosen for verification, as it showed very promising initialisation (via a maximised USRN) both in the single-defect and inhomogeneous cases. Prior to conducting the primary measurements, verification of the GS1$-$ES1 transition frequency was performed via resonant excitation spectroscopy, and verification of the $g_6 - g_8$ transition energy at 40 mT was performed via optically detected magnetic resonance (ODMR). These measurements can be found in Appendix B.III.

3.1 Optically Detected Two-Laser Spin Resonance (OD2LSR)

The technique used to experimentally verify the protocol utilised two lasers to initialise the system, a microwave (MW) to resonantly drive the transition, and a subsequent optical readout using one of the two lasers. For this reason, the technique is termed optically detected two-laser spin resonance (OD2LSR). The OD2LSR pulse sequence and the experimental setup can be seen in Figures 3.1b, c, respectively. In OD2LSR, two laser beams are continually incident on the sample, with one beam fixed in frequency and the other scanned over ($100 - 800$ MHz in 1 MHz steps). In this setup, an electro-optic modulator (EOM), paired with a Fabry-Perot cavity, enables the detuning of the scan beam (from 100 MHz). The two beams are created from an initial laser beam which is split by a beamsplitter. The beams are then made to align on the sample to ensure that they are accessing the same part of the defect ensemble, but do not align prior to incidence. When the laser light leaves the sample, the scan beam is detected with a photodiode but the fixed beam is blocked. Microwave pulses with the $\vec{B}$-field ($\mathbf{B}_1$ in Figure 3.1c) component parallel to the crystal c axis are applied to the sample at a fixed repetition rate. The MW frequency is set to the frequency of the relevant transition $g_i - g_j$. The two incident lasers attempt to initialise the system into state g_i for each detuning δ_S of the scan laser. Then, the MW drives the transition $g_i - g_j$, and the detected scan laser probes the change in population of state g_j. If the driving scheme ($\delta_F = 0$, $\delta_S = \omega_0$) results in good intialisation, this will be detected as an increase in the absolute value of the MW-induced signal. This can be

seen schematically in Figure 3.1b. Simultaneous measurements are done with only one laser, to compare the one-laser (uninitialised) and two-laser (initialised) spin resonance. A lock-in amplifier set to the MW pulse repetition rate is used, meaning only the changes in g_j are probed. Ultimately, an OD2LSR scan measures initialised spin-resonance - resonance between two GS1 eigenstates, with system initialisation into one of the eigenstates. The closest analog the measured signal has with the simulated model is the population contrast ΔP, and thus the population contrast is compared with the lock-in signal. Finally, a repump laser beam is used after each measurement period of 30 seconds to counteract charge-state switching, by bringing ionized V defects back to the neutral V^{4+}.
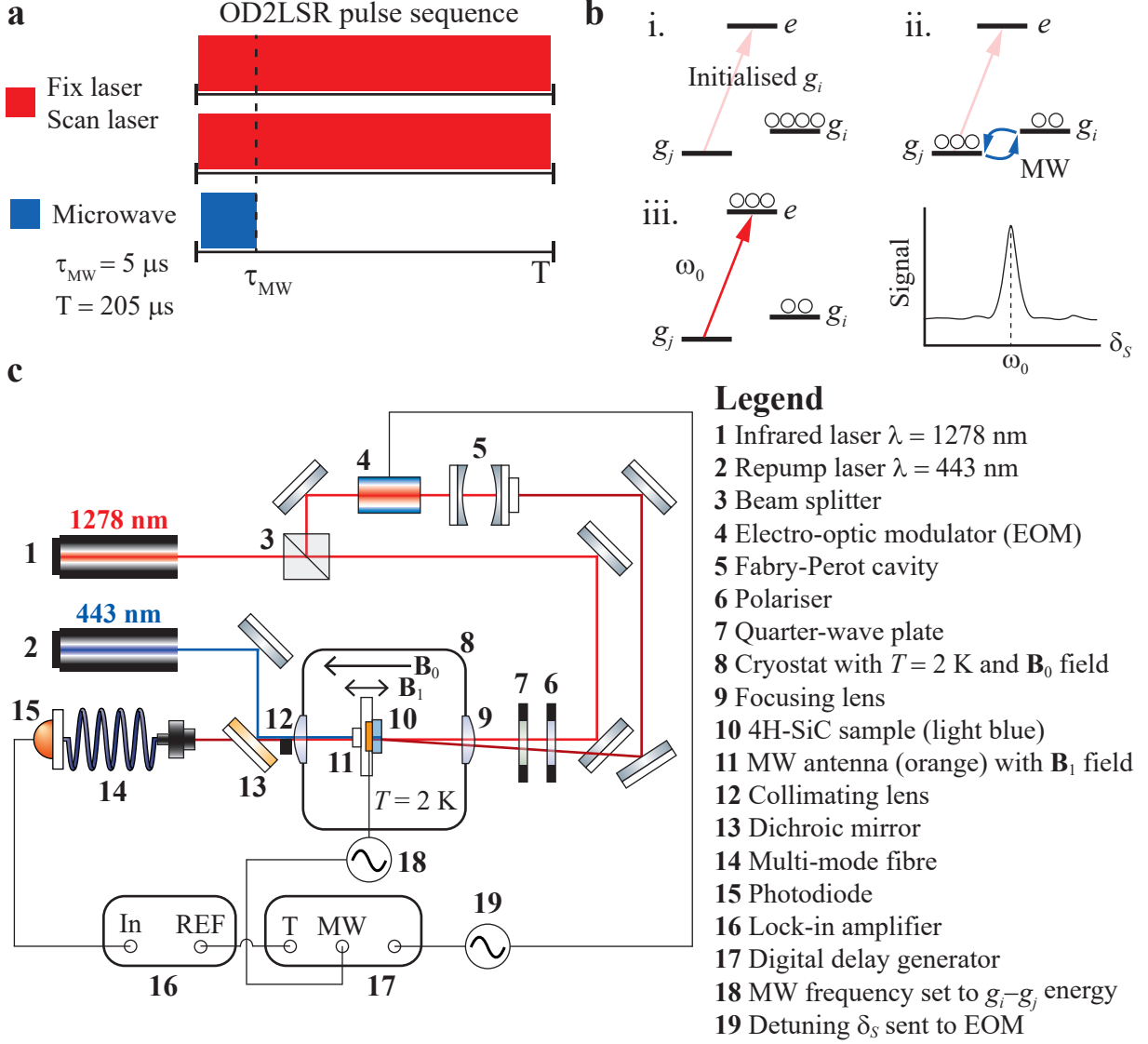

Figure 3.1: **a** The pulse sequence for optically detected two-laser spin resonance (OD2LSR). **b** Energy-level schematic showing how the system is probed: i. The system is two-laser initialised into g_i with a driving scheme that includes the $g_j - e$ transition. ii. Microwaves drive the population between states g_i and g_j. iii. The initialisation laser that is resonant with the transition $g_j - e$ (transition energy ω_0) probes the change in population in state g_j, effectively acting as an optical readout. This results in an increased OD2LSR signal at frequency ω_0. **c** Experimental setup for OD2LSR. The lock-in amplifier gets the reference (REF) for the microwave repetition rate (T, MW) from the digital delay generator (DDG). The detuning δ_S frequency signal is sent from a signal generator (**19**) to the EOM. The EOM creates detuned sidebands (first-order detuned by δ_S), and the Fabry-Perot cavity (narrow band-pass filter) lets through the first-order sideband.

4 Experimental Results: $g_6 - g_8$ Transition at 40 mT

4.1 Linear Polarisation

Figures 4.1a, b show the experimental results of an OD2LSR scan at 40 mT with linearly-polarised lasers. The two-laser signals have been normalised with respect to the corresponding one-laser signal (optically detected one-laser spin resonance). The one-laser signal can be seen in Figures 4.1a, b as a line at lock-in signal 1. The one-laser signal did not show any initialisation features, which is as expected since one laser cannot resolve hyperfine levels in an inhomogeneous ensemble. The microwave frequency was set to be resonant with the $g_6 - g_8$ transition (determined by an ODMR measurement, see Appendix B.III). Figure 4.1a has the scan laser as the short leg ($\delta_S < \delta_F = 0$) of the driving scheme, and Figure 4.1b has the scan laser as the long leg ($\delta_S > \delta_F = 0$) of the driving scheme (refer to Figure 2.3 for further clarification on the short and long legs of a driving scheme). The difference between the two OD2LSR signals is due to different transitions being accessed depending on whether the scan laser is the short or long leg of the driving scheme. Figure 4.1c shows the population contrast ΔP between g_6 and g_8 at 40 mT, for both one- and two-lasers, and uses the standard GS1 rate coefficients $\mathcal{R}^g$ (see Appendix B.I).[4] Due to the way the inhomogeneities are implemented in the simulated model, there is no difference between the scan laser being the short or the long leg of the driving scheme, and so the simulated ΔP contains the information of both.

It can be seen that the model predicts some initialisation features quite well, especially the peak at ~ 525 MHz. This peak corresponds to several[5] Π-schemes which initialise into g_8. However, there are some discrepancies. The relative amplitudes of some simulated initialisation features are not consistent with the experimental relative amplitudes. Furthermore, there are simulated peaks and dips which are not present in the experimental results. The relative amplitude problem arises from the assumption that the rate coefficients $\mathcal{R}$ are only temperature dependent (the coefficients were determined at 2 K). These coefficients are kept constant for other experimental factors such as the applied static magnetic field strength and the number (and power) of applied oscillating fields. This causes some of the effective-spin processes in the simulation to be stronger or weaker than they actually are, ultimately resulting in inconsistencies between the simulated and experimental relative amplitudes. Features seen in the simulation but missing in experiment are due to the lack of an optical readout state; while the simulation calculates all the eigenstate populations, in experiment the scan beam (i.e. the detected beam) can only probe one eigenstate at a time. If a driving scheme causes a population imbalance between g_6 and g_8, but the scan beam is probing neither g_6 nor g_8, this population difference will go undetected in an OD2LSR measurement. Therefore, the simulated population contrast is not a direct reflection of an OD2LSR measurement, but still provides a good measure of comparison. Further analysis on the different initialisation driving schemes, the optical readout problem, and the relative amplitude problem, along with suggested improvements for the model, can be found in Appendices C.I and C.II. As expected for an inhomogeneous ensemble, the average fidelity is < 0.1, which is far too small for quantum technology applications [32, 84]. However, inhomogeneous ensembles can still be useful for characterising, as is the case here.

A significant result from the experiment is the difference in the one- and two-laser signals. Figure 4.1c predicts a two-laser ΔP that is on average 0.4 percentage points higher than the one-laser ΔP, which is a significant difference for an inhomogeneous ensemble. However, in Figures 4.1a, b it can be

---

[4]Note that in the simulated inhomogeneous ensemble the absolute percentage value of ΔP does not hold significant physical meaning, as the simulation sums over a uniform ± 1 GHz inhomogeneity to calculate the populations. However, it is still useful in comparing relative values of ΔP, and hence, in predicting good points of initialisation. See Appendix B.I for more information.

[5]In the inhomogeneous case, one detuning (difference) $\Delta \delta$ can correspond to several different driving schemes.
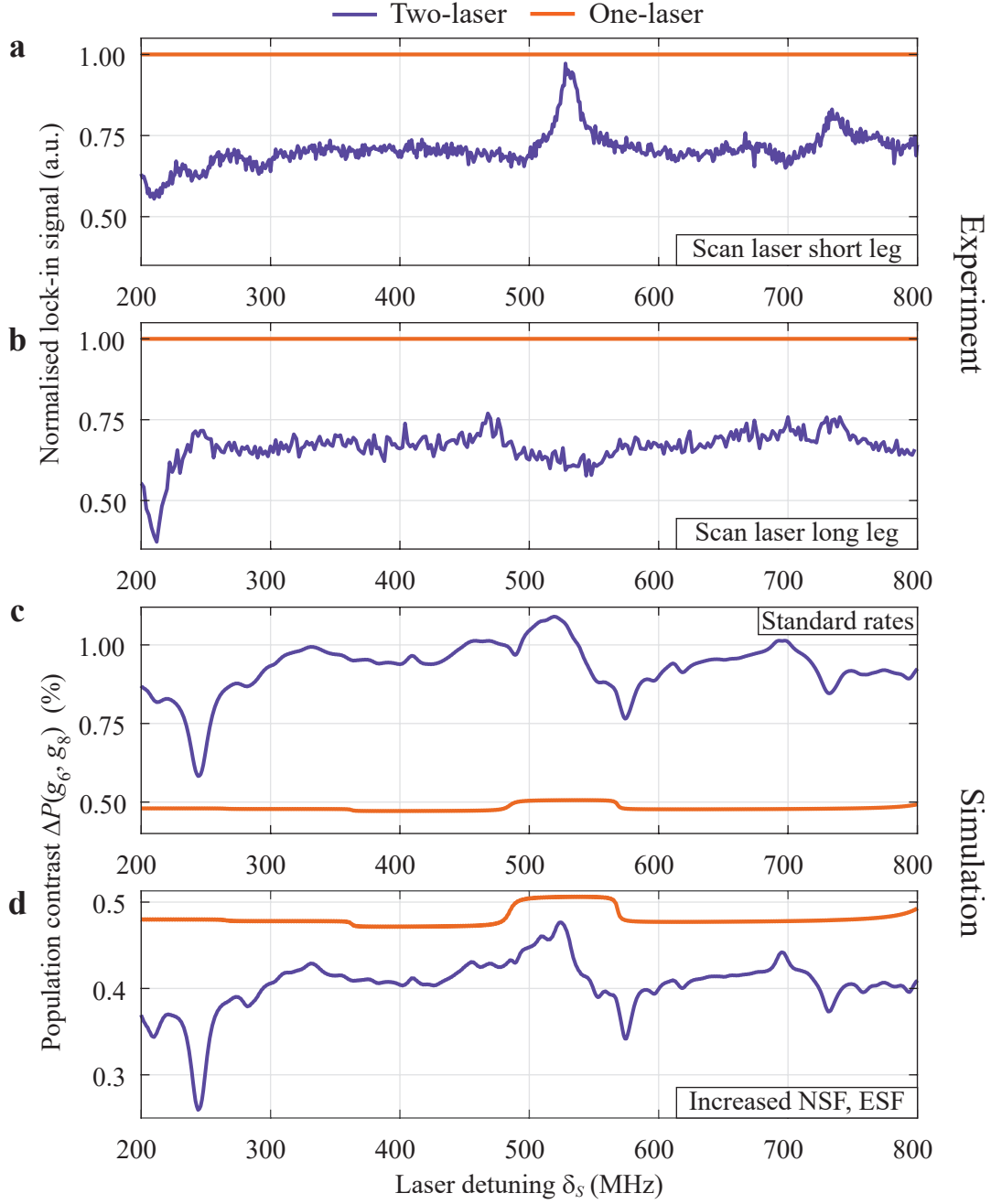
Figure 4.1: Two-laser driving schemes have one laser fixed, $\delta_F = 0$, and one laser scanned over the detunings δ_S. The one-laser schemes only have one laser which is scanned over the detunings δ_S. **a, b** OD2LSR measurements with microwave frequency set to $g_6 - g_8$ transition energy at 40 mT (microwave frequency used was 358.7 MHz, see Appendix B.III), normalised with respect to the one-laser signal. In the OD2LSR measurement of **a**, the scan beam δ_S is the short leg of the driving scheme ($\delta_S < \delta_F$), while in **b** the scan beam δ_S is the long leg ($\delta_S > \delta_F$). **c** Simulated population contrasts $\Delta P(g_6, g_8) = |P_{g_6} - P_{g_8}|$ with standard rate coefficients. **d** Simulated population contrasts $\Delta P(g_6, g_8)$ with increased NSF, ESF rate coefficients.

seen that the experimental two-laser signal is always below the one-laser signal. A consistently larger one-laser signal, which does not initialise the system, implies that two-laser initialisation is generally less effective. It is therefore imperative to understand the reason behind this signal difference, and to subsequently find ways to increase the two-laser signal to the extent that it surpasses the one-

laser signal.

It was found that the most probable reasons behind the signal difference involved some form of enhanced effective-spin relaxation. To test this in the simulation, the rate coefficients $\mathcal{R}$ were revised. By increasing the GS1 NSF rate coefficient $\mathcal{R}_{\mathrm{NSF}}^g$ from 1 kHz to 3.5 kHz, and the GS1 ESF rate coefficient $\mathcal{R}_{\mathrm{ESF}}^g$ from 10 kHz to to 20 kHz, the two-laser population contrast decreased by around 0.6 percentage points, as seen in Figure 4.1d (standard rate coefficients used for the one-laser case). This decrease results in a two-laser ΔP that is consistently lower than the one-laser ΔP, reflecting experiment. Furthermore, the detuning accuracy between the simulated and experimental initialisation features increased on average by ~ 5 MHz. The reason the GS1 NSF and GS1 ESF were changed is as follows. The addition of a second laser is not expected to cause an order (or several orders) of magnitude change to the spin-relaxation time. Thus, only the relaxation processes (x : ESF, NSF, FF, FFz in GS1 and ES1) that significantly affect the simulation response when making only minor changes to the corresponding rate coefficient $\mathcal{R}_x^{g,\,e}$ were considered. Note that these processes are not the dominant processes - they are only the processes that the simulation is most sensitive to. At 40 mT, these were the GS1 NSF, followed by the GS1 ESF (refer to Appendix B.I for more information on how this was determined).

The ratio between the simulated one-laser and two-laser contrasts is to some extent arbitrary, since as mentioned, the population contrast is not a direct reflection of an OD2LSR measurement. Furthermore, although the choice to increase the GS1 NSF and ESF rate coefficients was justified within the model, the new assigned values were determined by trial and error (while being guided by the observed trends), and done simply to give a closer fit to the experimental data. This is also why the rate coefficients for the two-laser case were changed, as opposed to the one-laser case, even though the standard rate coefficients were determined using two-laser spectroscopy data. Thus, while increasing the rate coefficients for the two-laser case implies a decrease in the GS1 spin-relaxation time T_1, it does not provide accurate quantitative information on this decrease. What is of importance however, is that a clear decrease in the two-laser population contrast, paired with an increased detuning accuracy between simulated and experimental initialisation features, was seen. Several other hypotheses which were considered to explain the signal difference (Appendix C.III) were unable to replicate this behaviour. This strongly suggests that this signal difference is caused by some spin-relaxation effect.

Increasing the GS1 NSF and ESF rate coefficients implies a decreased spin-relaxation time T_1. A possible reason for this is that an additional electric field (i.e. the second laser) may cause perturbations in the surrounding lattice sites. In turn, this might affect charge-state configurations, phonon modes, and other lattice and defect characteristics. These environmental changes could then affect the crystal field potential, and in turn, the spin-state dynamics of the system, ultimately resulting in a decreased spin-relaxation time T_1. The most efficient way to verify this would be to conduct one- and two-laser time-resolved T_1 measurements (refer to Astner et al. [73] and Gilardoni [72] Chapter 6 for more information on measurement procedures), and check if the two-laser T_1 is shorter than the one-laser T_1. If the signal difference is indeed caused by a T_1 effect, this will affect initialisation for both the inhomogeneous and single-defect cases. The increased T_1 effect could possibly be mitigated by decreasing the temperature. Astner et al. [73] measured $T_1 \approx 25$ s at 100 mK. In general, decreasing the temperature results in higher spin-relaxation times, and thus allows for better control of the system. However, as will be seen in Section 5.3, decreasing the temperature means new protocols need to be developed. At 2 K, the initialisation protocols necessarily rely on GS1 and ES1 relaxation. If these relaxation rates substantially decrease, the protocols must change accordingly.

While increasing the GS1 NSF and ESF rate coefficients implies a T_1 decrease, there is another spin-relaxation mechanism that could possibly manifest as an effective T_1 decrease. Adding a second laser

could enhance ES1 spin relaxation, which over the entire ensemble causes population to leak from g_8. While this population leakage would not cause an actual change in the GS1 spin-relaxation time T_1, it could result in an effective change in the measured T_1. This only happens in an inhomogeneous ensemble, and can be understood as follows. In general, perturbing the system will cause a population imbalance between all the eigenstates. This is why there is still a nonzero signal measured with only one laser. Furthermore, it was mentioned in Section 3 that the system tends to initialise very well into g_8 (or g_{16}). As will be discussed in Section 5.1, this is due to the spin-state dynamics and relaxation pathways at 2 K. This means that one laser incident on the sample with frequency ω_1, at the right magnetic field strength,[6] will inadvertently cause a greater population imbalance between g_8 and the other GS1 eigenstates. Adding a second laser with frequency ω_2 allows for the resolution of hyperfine structure, which is why clear initialisation features (peaks, dips in the OD2LSR signal) can be seen in Figures 4.1a, b. At the same time, adding a second laser causes more of the population to be driven into the excited state ES1. For a single defect, this aids the initialisation, provided that the appropriate driving scheme (ω_1, ω_2) is chosen (see Section 5.2). However, in an inhomogeneous ensemble, the scheme (ω_1, ω_2) will only be efficient in initialising one part of the ensemble. For other defects in the ensemble, (ω_1, ω_2) will form driving schemes that are resonant with other transitions. Here is where the second laser causes a problem. By driving more of the population into ES1 with driving schemes that do not initialise (well) into g_8, the population becomes more evenly distributed amongst the excited eigenstates via the ES1 relaxation processes, especially when considering that these processes have a lifetime (~ 10 ns [79]) an order of magnitude smaller than the optical lifetime (~ 100 ns [60, 61]). This then results in the GS1 populations in these uninitialised defects being more evenly distributed (after optical relaxation), and over the entire ensemble, results in an effective leakage of population from the initialised state (g_8). This population leakage decreases the fidelity of g_8 and reduces the strength of the OD2LSR signal. In addition, since the GS1 population is now more evenly distributed, it takes a shorter time for the system to relax. While the true GS1 spin-relaxation time T_1 has not actually changed, the population leakage causes an effective change in the measured T_1.

This population leakage also happens in the one-laser case, but to a lesser degree, since there is only one driving field instead of two. Thus, since one laser can still cause a population imbalance between g_6 and g_8, and since there is less population leaking into the other GS1 eigenstates, the result is a one-laser signal that is greater than the two-laser signal. Since this population leakage can manifest as a T_1 effect, developing an experimental method to verify this is not trivial. A possible way would be to decrease the temperature and conduct OD2LSR measurements. At very low temperatures the spin-state dynamics of both GS1 and ES1 change and new protocols are required (Section 5.3), so when decreasing the temperature the ES1 spin-relaxation time cannot exceed the optical lifetime (100 ns). If the ES1 spin-relaxation time increases (but still < 100 ns), the population will be less effectively distributed amongst the ES1 eigenstates, and hence the population leakage effect will reduce. Since this reduction happens for both one and two lasers, the two-laser baseline signal is still expected to be lower than the one-laser baseline. However, this suppressed population leakage might result in a higher two-laser signal at detunings which form good initialisation driving schemes. In fact, preliminary experimental results show that at 1.8 K the peak at ~ 525 MHz surpasses the one-laser signal. This is a strong indication that the signal difference is caused by a population leakage. These preliminary results can be found in Appendix C.IV.

Since reducing the temperature increases T_1, it is necessary to simultaneously verify that this is not a T_1 effect. This could be done by studying the laser power dependency of one- and two-laser

---

[6]Whether the system initialises more into g_8 or g_{16} is dependent on several factors, including the magnetic field strength.

T_1 measurements. If a one-laser T_1 measurement shows no dependency on laser power, this would indicate that adding another electric field is unlikely to affect the system. At the same time, if a two-laser T_1 measurement shows a dependency on laser power this would imply that a population leakage, resulting from enhanced ES1 relaxation over the ensemble, might be responsible for the signal difference. Here, the intensity of the second laser would govern the extent of the leakage. Preliminary experimental results have shown that the one-laser T_1 has no dependency on power, while the two-laser T_1 decreases with increasing fixed beam (i.e. undetected beam) power [85], again indicating that the signal difference is caused by a population leakage. If this signal difference is indeed caused by a population leakage, as opposed to a T_1 effect, this is promising for single-defect initialisation. The population leakage is a result of an initialisation driving scheme simultaneously driving other non-initialising transitions in the inhomogeneous ensemble. As such, it is not present at the single-defect level. ES1 spin relaxation still occurs for single defects, but it forms an integral part of the initialisation process, as will be seen in Section 5.2.

Unfortunately, while initialised spin resonance was seen for the qubit candidate $g_6 - g_8$, no coherence was able to be measured (i.e. Rabi oscillations were not observed). The reason for this might be due to the fact that the $g_6 - g_8$ transition is mediated by a $\Delta m_I = 2$ process, meaning that it is an electric quadrupole transition (as opposed to a magnetic dipole transition, $\Delta m_I = 1$). This means that a magnetic field is unlikely to drive the transition coherently. An electric field might be able to drive coherence however. Further information on this can be found in Appendix C.VI.

4.2   Circular Polarisation

Section 2.3.1 outlined a procedure to implement circular polarisation within the simulated model. This was also experimentally tested, and the results can be seen in Figure 4.2 (simulated results with increased NSF, ESF coefficients). As explained in Section 2.3.1, using circularly polarised light suppresses one of the effective-spin transitions (i.e. $\uparrow \Longrightarrow \nearrow$ or $\downarrow \Longrightarrow \swarrow$ transitions). In both experiment and simulation, it can be seen that σ_- polarisation (right-hand circularly polarised, quarter-waveplate at $+45°$) results in clear initialisation features, similar to the linearly-polarised results. The ~ 525 MHz peak seen in Figure 4.2a is slightly higher (around 0.3 lock-in signal units) than the peak in Figure 4.1a, although this may be attributed to noise. The ΔP value of the simulated ~ 525 MHz peak with σ_- polarisation, seen in Figure 4.2c, is roughly double the simulated ΔP peak with linear polarisation (Figure 4.1d). Both these results indicate that the appropriate circular polarisation may aid initialisation. As expected from simulation, the initialisation with σ_+ polarisation is worse than the linear and σ_- polarisations. While there are some discrepancies between the experimental and simulated circularly-polarised results, the general trend shows that the operators $\mathcal{O}_\pm$ are able to predict the significant differences in behaviour between the two circular polarisations seen in experiment. Thus, $\mathcal{O}_\pm$ will also be implemented in the theoretical single-defect protocols.

4.3   Conclusions

To conclude, it can be seen that the simulation (with the increased rate coefficients) is able to predict initialisation features with a relatively high degree of accuracy (around ± 10 MHz), provided that said features can be optically read out. Furthermore, the experimental initialisation features were predicted by both the inhomogeneous and single-defect simulations. As mentioned in Section 2.3, to go from a single-defect driving scheme (δ_1, δ_2) to an inhomogeneous driving scheme $\Delta\delta$, the laser detunings have to simply be subtracted $\Delta\delta = \delta_1 - \delta_2$. In terms of the single-defect case, the ~ 525 MHz peak is the result of several driving schemes that all have single-defect fidelities of > 0.35. Note that while this is quite a low fidelity, the experimental limitations ($\Delta\delta > 100$ MHz,
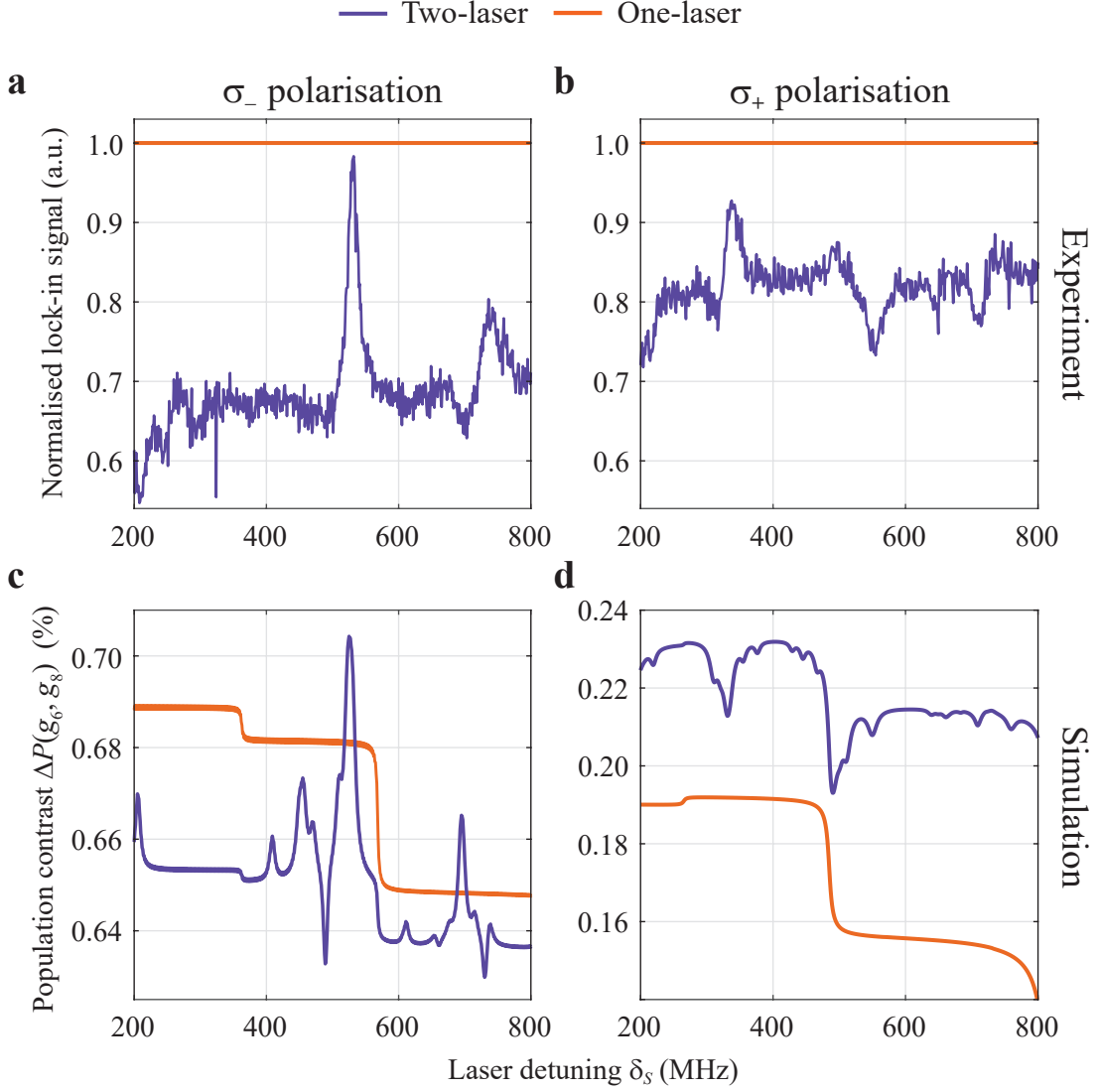
Figure 4.2: Two-laser driving schemes have one laser fixed, $\delta_F = 0$, and one laser scanned over the detunings δ_S. The one-laser schemes only have one laser which is scanned over the detunings δ_S. **a, b** OD2LSR measurement normalised with respect to the one-laser signal. Both lasers are circularly polarised, σ_- polarisation (right-hand circularly polarised) in **a** and σ_+ polarisation (left-hand circularly polarised) in **b**. **c, d** Simulated population contrast $\Delta P(g_6, g_8)$ with σ_- polarisation in **c** and σ_+ polarisation in **d**. The drops in the one-laser ΔP are broadened single-defect peaks, which disappear when the inhomogeneities increase. Since they are a result of the small effective inhomogeneity range used in the simulation (-1 GHz to 1 GHz, see Appendix A.I), they can be considered simulation artefacts.

MW frequency between $200 - 600$ MHz) prevented better initialisation points from being studied. This experimental verification, of both the (simulated) inhomogeneous and single-defect initialisation protocols at 40 mT, motivates the use of the simulated model in developing theoretical single-defect protocols over a larger range of magnetic fields and laser detunings. Finally, it can be clearly seen that high-fidelity initialisation in an inhomogeneous ensemble (with ~ 20 GHz inhomogeneous broadening) is not possible. The simulated fidelities were all < 0.1, and the OD2LSR contrasts were in general very low, indicating that inhomogeneous ensembles are not suited for quantum technology applications.

5 Theoretical Single-Defect Initialisation

Although preliminary experimental results suggest that the signal difference discussed in Section 4.1 is an inhomogeneous ensemble effect, this was not known when the (single-defect) results in this section were simulated and processed. Thus, the two-laser simulated results in this section use the increased NSF and ESF rate coefficients. The rate coefficients $\mathcal{R}$ were determined at $T = 2$ K, meaning that the following analysis is only applicable for neutral V^{4+} defects in 4H-SiC at 2 K. The effects of temperature changes are considered in Section 5.3. Instead of using the detuning $\Delta\delta$ as in the inhomogeneous case, now the individual laser detunings δ_1, δ_2 (or δ_F, δ_S) are considered.

To acquire a more complete picture in the single-defect case, the 32 populations in GS1 and ES1 were simulated as a function of (δ_1, δ_2) for three polarisations and the magnetic fields $0 - 99$ mT in 1 mT steps. From this data, the population contrasts ΔP between all 16 GS1 eigenstates were calculated per magnetic field, with the threshold requirements that $\Delta P(g_i, g_j) \geq 75\%$ and $|\langle g_j|\mathcal{O}_{esd}|g_i\rangle|^2 \geq 10^{-6}$. A more restrictive threshold was applied on ΔP as it plays a bigger role than the ESD transition probability in initialised spin-resonance, as explained in Appendix C.V, but the choice of 75% was arbitrary. The ESD transition probability threshold was kept low to maintain an overview of all possible multipole transitions. No limits were imposed on the GS1 eigenstate transition frequencies as the limits previously imposed (between $200 - 600$ MHz) were due to limitations of the microwave antenna used in experiment. The detuning ranges used were -900 to 900 MHz in 1 MHz steps for both lasers, as explained in Appendix B.II.

Prominent initialisation into g_8 and g_{16} was found at a range of different magnetic fields. The lowest magnetic field found with $\Delta P \geq 75\%$ was at 34 mT, indicating that the hyperfine and mixed hyperfine-electronic Zeeman regimes[7] have relaxation pathways which are too strong for good initialisation. Since the only good points of initialisation were found in the electronic Zeeman dominated regime ($\gtrsim 30$ mT), the following analysis will be focused on this regime. The eigenstates g_i, e_i can then be approximated by the effective-spin basis states $|\{g, e\}, m_{\tilde{S}}, m_I\rangle$ where $\{g, e\}$ indicates whether the state is in GS1 (g) or ES1 (e).

5.1 Spin-State Dynamics in the Zeeman Regime

Above ~ 30 mT, the system is dominated by the electronic Zeeman interaction. As such, the spin-state dynamics of the system are to some extent magnetic field independent. To show this, a normalised average of the GS1 and ES1 relaxation Lindbladians including rates[8] was calculated for the magnetic fields $40 - 99$ mT. This is shown in Figure 5.1. It is clear to see a prominent general trend for this magnetic field range. For all the GS1 eigenstates, the flip-flop is the strongest relaxation process due to both its high transition probability $|\langle\mathcal{O}_{FF}\rangle|^2$ and its relatively large rate coefficient $\mathcal{R}^g_{FF}$ (Appendix B.I). The flip-flop process entail a simultaneous nuclear spin flip Δm_I and effective-spin flip $\Delta m_{\tilde{S}}$. For a given state i, the state j with the strongest flip-flop transition probability is one which minimises both the change in spin, so $\Delta m_{\tilde{S}} = 1$, $\Delta m_I = 1$, and the total energy of the system. The strength of the flip-flop causes an asymmetric relaxation configuration between the GS1 eigenstates, following the pattern $g_1 - g_{15}$, $g_2 - g_{14}$, and so on until $g_6 - g_{10}$ and $g_7 - g_9$.[9] This can be seen by comparing the blue diagonal line with the pink off-anti-diagonal line

---

[7]The hyperfine regime ($0 - 10$ mT) is the magnetic field range where the hyperfine interaction is the dominant interaction in the Hamiltonian, while in the mixed hyperfine-electronic Zeeman regime ($10-30$ mT) the two interactions have roughly equal strengths.

[8]With increased NSF, ESF rate coefficients.

[9]The relaxation rate of the transition $g_i - g_j$ is the element ij in the corresponding relaxation Lindbladian matrix. See Section 2.3 for further details.

(hence asymmetric) in Figure 5.1a. The preferred flip-flop eigenstate for g_{16} is g_2, but $g_2 - g_{14}$ is lower in energy. The preferred flip-flop eigenstate for g_8 is with g_{10}, but g_{10} has a strong flip-flop with g_6. While $g_8 - g_{10}$ is lower in energy than $g_6 - g_{10}$, the flip-flop relaxation scheme that includes $g_8 - g_{10}$ leads to the asymmetric pattern $g_2 - g_{16}$, $g_3 - g_{15}$, ..., $g_6 - g_{12}$, $g_7 - g_{11}$, $g_8 - g_{10}$. This scheme results in all other transitions being much higher in energy, making it energetically unfavourable, and as such it is not the dominant relaxation configuration. In fact, the strongest relaxation pathways that g_8 and g_{16} have are nuclear spin flip and electronic spin flip mediated, with corresponding relaxation rates that are several hundred times less than the average relaxation rate (coming from the flip-flop mediated relaxation processes). This leaves both g_8 and g_{16} without any strong relaxation pathways. For this reason it is easiest to initialise the system into either g_8 or g_{16}. From this point on these states will be referred to as the *static states*, since they are relatively static in relaxation. In ES1, the relaxation is dominated by electronic spin flip mediated processes. This strong ESF results in a symmetric relaxation configuration, where eigenstates in one effective-spin manifold are paired with eigenstates in the opposite manifold with the same nuclear spin m_I. Explicitly, $g_1 - g_{16}$ ($m_I = 7/2$), $g_2 - g_{15}$ ($m_I = 5/2$), ..., $g_8 - g_9$ ($m_I = -7/2$). In Figure 5.1b, this symmetric pattern can be seen by comparing the blue diagonal line and the pink anti-diagonal line.
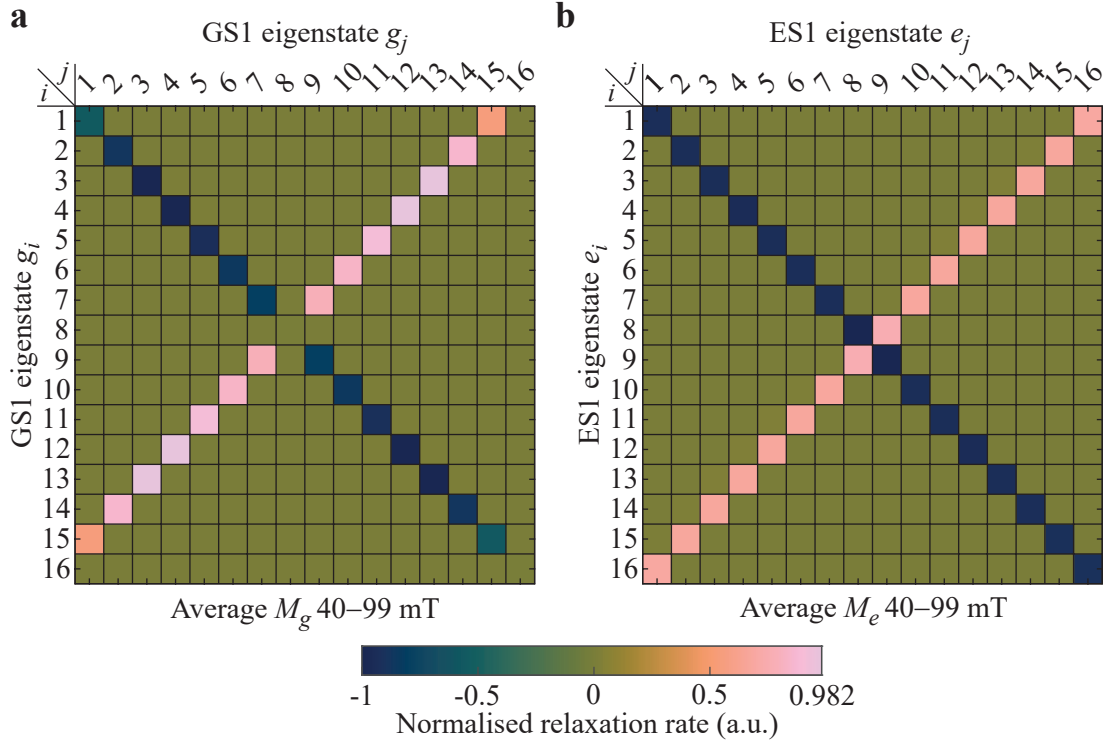

Figure 5.1: **a** The GS1 relaxation Lindbladian matrix M_g normalised to the maximum absolute rate in M_g averaged over the magnetic field range $40 - 99$ mT. The maximum rates are on the order of 1 MHz. To obtain a clearer picture of the effective-spin relaxation dynamics, the driving rates $-\Omega$ on the diagonal are omitted. **b** The ES1 relaxation Lindbladian matrix M_e normalised to the maximum absolute rate in M_e averaged over the magnetic field range $40 - 99$ mT. The maximum rates are on the order of 10 MHz. For the same reasons as **a**, the optical relaxation rates $-\Gamma$ on the diagonal have been omitted. For **a** (**b**), the term ij gives the normalised relaxation rate from state g_j (e_j) into state g_i (e_i). The negative rates on the diagonal ii indicate population leaving the state g_i (e_i) (the $-\gamma_{g,e}$ terms in the Lindbladian matrix, Eq. (2.11)). This population goes to the other states, indicated by positive rates in the relaxation Lindbladian matrix, such that each column in the matrix sums to zero. Note that the green off-diagonal terms have normalised relaxation rates slightly above zero.

The combination of using two lasers, the strong GS1 flip-flop mediated relaxation, and the strong ES1 electronic spin flip mediated relaxation, causes a phenomenon whereby if both lasers are driving transitions within an effective-spin manifold, the static state in the opposite manifold is initialised. The reason for this is as follows. Consider two eigenstates g_i, g_j in the $\uparrow$ manifold, where necessarily i, $j < 8$. Suppose these eigenstates are being driven by the direct (spin-state-conserving) optical transitions $g_i - e_i$ and $g_j - e_j$. The states e_i, e_j in the $\nearrow$ manifold effectively relax via the strong ES1 electronic spin flip mediated process to e_k, e_l respectively. The eigenstates e_k, e_l are in the $\swarrow$ manifold and optically relax into their corresponding GS1 states, g_k and g_l ($\downarrow$ manifold, k, $l > 8$). Then, the strong GS1 flip-flop results in an effective relaxation of the system into the states g_m, g_n ($\uparrow$ manifold) which are strongly flip-flop coupled to g_k, g_l ($\downarrow$ manifold), respectively. Due to the asymmetry of the flip-flop, m, $n = i$, $j - 1$ and m, $n = 16 - k$, l (this also applies if starting in the $\downarrow$ manifold). Now this process continues until the majority of the population sits in g_m, g_n and their respective flip-flop coupled states g_k, g_l. After the flip-flop, nuclear spin flip mediated transitions are the next strongest GS1 relaxation process. The states g_m and g_n can relax into their adjacent effective-spin states (adjacent states have $\Delta m_I = 1$), but if they relax upwards into g_i or g_j, the population will be driven (and relax) back into g_m and g_n. The same applies to their flip-flop coupled states, g_k and g_l, when relaxing downward towards g_i and g_j. Thus, g_m, g_n can effectively only relax downward (states lower than m, n) while g_k, g_l can effectively only relax upward (states higher than k, l). Through a series of nuclear spin flip and flip-flop mediated processes, the system eventually tends towards g_1 and its strongly flip-flop coupled state g_{15}. All the while, weak relaxation channels between g_1 and g_{15} with g_{16} (ESF and NSF mediated relaxation, respectively) slowly populate g_{16}. Since g_{16} has very weak coupling with all other GS1 eigenstates, the population stays in g_{16}. In the steady-state, this eventually leads to a strong spin polarisation of the system into g_{16}. If driving $\downarrow \Longrightarrow \swarrow$ transitions, the system is initialised into g_8 by the same mechanism (weak relaxation channels with g_7 and g_9, a flip-flop pair). This process can be seen schematically in Figures 5.2b, d. It is clear to see here that any steady-state initialisation protocol is then dependent on the longest spin relaxation timescale; this is further elaborated in Section 5.3.

As a general rule, driven transitions which involve an excited eigenstate e_i which is coupled via the ES1 electronic spin flip to the ES1 analog of the static state (i.e. e_8 or e_{16}) will initialise the system better. This is because there are no intermediate pathways. For g_{16}, the transition $g_1 - e_1$ results in an ES1 electronic spin flip mediated effective relaxation into e_{16}, and subsequent optical relaxation into g_{16}. The transition $g_9 - e_9$ results in an electronic spin flip mediated transition into e_8, and subsequent relaxation into g_8. Furthermore, the above analysis does not consider the fact that the optical linewidth is around 10 MHz [60, 61], meaning that neighbouring m_I states are also weakly driven by the applied optical fields, which only serves to amplify the spin polarisation. Due to this and the spin-state dynamics of the system, the most efficient initialisation happens by driving neighbouring optical transitions (e.g. $g_1 - e_1$, $g_2 - e_2$ for g_{16} initialisation). This is also the case for inhomogeneous ensembles, but since the experimental setup could not detune below 100 MHz, these small detunings $\Delta \delta$ were not accessible. Since the static states are each associated with specific effective-spin-manifold optical transitions, implementing circular polarisation amplifies the initialisation. The $\uparrow \Longrightarrow \nearrow$ transitions initialise into g_{16}, and since σ_+ polarisation amplifies said transitions, σ_+ polarisation initialises into g_{16} better than linear polarisation. The same applies for σ_- and g_8. Seeing that in the steady-state g_8 and g_{16} can be very well initialised, these states and their respective initialisation protocols were analysed further.

When the driving scheme includes both $\uparrow \Longrightarrow \nearrow$ and $\downarrow \Longrightarrow \swarrow$ direct transitions or spin-manifold-cross transitions such as $\uparrow \Longrightarrow \swarrow$ the two optical transitions compete, and it is harder to initialise the system. Spin-manifold-conserving cross transitions, where there is a change in m_I but the effective-spin

manifold is conserved, are generally very weak and do not significantly affect the system. Fidelities above 0.8 can still be achieved with spin-manifold-cross transitions, but the scheme must include one transition that initialises into the static state very well (typically not a cross transition), and the cross transition must be chosen carefully. These transitions are only necessary in continuous-wave experiments, where one of the initialisation lasers must also act as an optical readout laser. This is further elaborated in Appendix D.I.

5.2   Analysis of g_8 and g_{16} Initialisation

The $0 - 99$ mT 16 GS1 eigenstate analysis found several areas of system initialisation into g_{16} with fidelities above 0.92, and initialisation into g_8 with fidelities above 0.88. The highest fidelity achieved was an initialised g_{16} at 99 mT with σ_+ polarisation with a maximum fidelity of > 0.921, as seen in Figure 5.2a. There is one detuning scheme which attains this level of fidelity, using the detunings $\delta_1 = -259$ MHz and $\delta_2 = -252$ MHz. The -259 MHz detuning corresponds to a very strong ($|\langle \mathcal{O}_+ \rangle|^2 > 0.99$) $g_1 - e_1$ optical transition, while the -252 MHz corresponds to a very strong ($|\langle \mathcal{O}_+ \rangle|^2 > 0.99$) $g_2 - e_2$ optical transition. It can be seen in Figure 5.2a that when one of the lasers is fixed at a detuning $\delta_F = -252$ MHz, the baseline fidelity (i.e. the fidelity away from any peaks or dips) is ~ 0.15 less than the baseline fidelity of when the fixed laser is detuned to $\delta_F = -259$ MHz. This is because the -252 MHz $g_2 - e_2$ transition has an intermediate pathway $g_2 \xrightarrow[\text{Opt.Exc.}]{} e_2 \xrightarrow[\text{ESF}]{} e_{15} \xrightarrow[\text{Opt.Rlx.}]{} g_{15} \xrightarrow[\text{FF}]{} g_1$ in initialising g_{16}, as can be seen in the initialisation schematic Figure 5.2b. This intermediate step also results in a leaking of population, whereby other states are populated via weaker but still prominent relaxation pathways, and hence a lower population contribution to g_{16}.

This initialised g_{16} state at 99 mT with σ_+ polarisation had the largest population contrast ΔP with g_2 ($\sim 83.92\%$), but the $g_2 - g_{16}$ ESD transition probability is around 10^{-3} orders of magnitude lower than the ESD transition probability ($|\langle g_9 | \mathcal{O}_{\text{esd}} | g_7 \rangle|^2 \approx 8 \cdot 10^{-2}$) of the coherently drivable $g_7 - g_9$ 30 mT clock transition. Taking the ESD transition probability of this clock transition as a spin-resonance benchmark, the $g_2 - g_{16}$ probability is too small. Furthermore, $g_2 - g_{16}$ is not a ZEFOZ transition. The transition with the next highest population contrast ($\sim 83.86\%$) was between g_{16} and g_{14}, also at 99 mT with σ_+ polarisation, with an ESD transition probability roughly half that of $|\langle g_9 | \mathcal{O}_{\text{esd}} | g_7 \rangle|^2$ at the 30 mT clock transition. If the ESD transition probability between two eigenstates is too high (> 0.1) the two-state population contrast will be extremely low. If the ESD transition probability is too low (< 0.01), it will increase the population contrast but driving spin resonance is unlikely, and even less so for coherence. The dynamics of this are further explained in Appendix C.V. Since the $g_{14} - g_{16}$ ESD transition probability is on the order of the $g_7 - g_9$ ESD transition probability, the $g_{14} - g_{16}$ transition is likely to be coherently driven with a suitable oscillating field, especially considering that the fidelity of g_{16} can reach > 0.92 with the appropriate protocol. $g_{14} - g_{16}$ is also a ZEFOZ transition. States like g_{14}, which show promising population contrasts and ESD transition probabilities with the relevant static state, will be referred to as coherent partner (CP) states. The static state and the CP state combined make a qubit candidate. Thus, g_{14} is the coherent partner (CP) state of g_{16}, and $g_{14} - g_{16}$ is the corresponding qubit candidate. The $g_{14} - g_{16}$ transition at 99 mT is mediated by a $\Delta m_I = 2$ nuclear spin flip mediated transition. This is an electric quadrupole transition, and hence is likely to be coherently driven with an electric field. Magnetic spin resonance is still likely to be possible however, as was measured for $g_6 - g_8$ at 40 mT in Section 4. Further information can be found in Appendix C.VI.

The g_8 initialised states had slightly lower fidelities than g_{16} but still provided promising areas of initialisation. The highest population contrast achieved was between g_8 and g_{10}, with a contrast
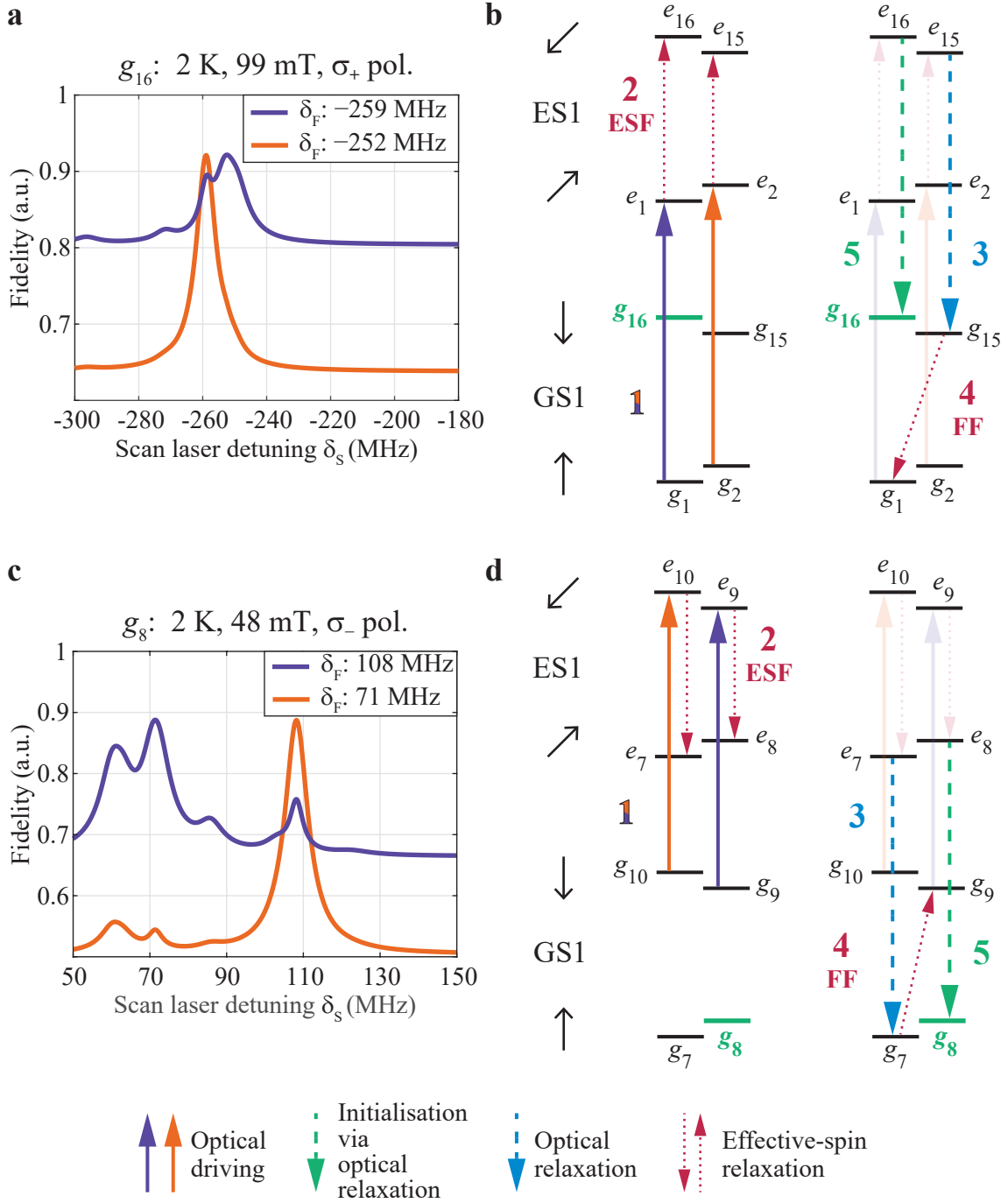
Figure 5.2: **a** Fidelity of g_{16} as a function of scan-laser detuning δ_S at 99 mT with σ_+ polarisation. The purple (orange) plot is for a fixed-laser detuning of $\delta_F = -259$ MHz ($\delta_F = -252$ MHz), corresponding to the $g_1 \to e_1$ ($g_2 \to e_2$) transition. Note that the peaks of both plots with fidelities of $F > 0.921$ correspond to the same driving scheme $(\delta_1, \delta_2) = (-259$ MHz, -252 MHz$)$. **c** Fidelity of g_8 as a function of scan-laser detuning δ_S at 48 mT with σ_- polarisation. The purple (orange) plot is for a fixed-laser detuning of $\delta_F = 108$ MHz ($\delta_F = 71$ MHz), corresponding to the $g_9 \to e_9$ ($g_{10} \to e_{10}$) transition. **b, d** Energy-level diagram showing initialisation of g_{16}, g_8 with the driving scheme $(\delta_1, \delta_2) = (-259$ MHz, -252 MHz$)$, $(\delta_1, \delta_2) = (108$ MHz, 71 MHz$)$ labelled with **1**. Additional steps **3, 4, 1, 2** involved in initialising results in a population leakage (weak GS1, ES1 relaxation into other eigenstates), and hence a lower baseline fidelity for $\delta_F = -252$ MHz, $\delta_F = 71$ MHz in the steady state.

ΔP of $\sim 77.5\%$ and a corresponding g_8 fidelity of > 0.88, at 41 mT and σ_- polarisation. However, the corresponding ESD transition probability is an order of magnitude lower than the $g_7 - g_9$ clock transition ESD transition probability. The following highest contrast was between g_6 and g_8 at 48 mT,[10] with a contrast of $\sim 77.4\%$ and a g_8 fidelity also > 0.88. The fidelity can be seen in Figure 5.2c. The corresponding ESD transition probability is on the same order of magnitude as the $g_7 - g_9$ clock transition ESD transition probability, and as such $g_6 - g_8$ at 48 mT is a promising transition for coherent driving. Further considering that this is a ZEFOZ transition, g_6 is a suitable CP state for g_8. The highest fidelity is achieved with the driving scheme $(\delta_1, \delta_2) = (108$ MHz, 71 MHz$)$. With the fixed laser at 108 MHz, the baseline fidelity is ~ 0.66, roughly 30% higher than with the fixed laser at 71 MHz. Similar to the g_{16} case this can be understood in terms of the driving and relaxation pathways. The 108 MHz detuning corresponds to the $g_9 - e_9$ transition, which after an ES1 electronic spin flip mediated relaxation, goes into e_8, which optically relaxes and initialises into g_8. The 71 MHz detuning corresponds to the $g_{10} - e_{10}$ transition, which has an intermediate step before initialising into g_8. This can be seen schematically in Figure 5.2d.

5.3 Experimental Recommendations for Initialisation

Initialisation at 2 K

The initialisation driving schemes in Section 5.2 do not optically address any of the candidate qubit states, and as such, do not provide optical readout. For continuous-wave experiments such as OD2LSR, this is problematic. While this section focuses on pulsed protocols, for which this is not a problem, Appendix D.I provides more information on how this optical readout problem can be mitigated for continuous-wave experiments. In a steady-state pulsed protocol, the system is first initialised by two simultaneous laser pulses, with a pulse time sufficiently long enough to reach the steady state. Then, operations and readout are conducted after initialisation. This is in contrast to the continuous-wave OD2LSR process, whereby coherent driving and readout were conducted while the lasers were still incident on the sample. The focus remains on g_8 and g_{16}, using the same driving schemes introduced in Section 5.2. For a V defect in a 4H-SiC sample kept at 2 K, the following steady-state initialisation protocol is developed. First, the qubit candidates $g_6 - g_8$ at 48 mT and $g_{14} - g_{16}$ at 99 mT are selected. These qubit candidates have high population contrasts, and ESD transition probabilities on the order of the coherently drivable $g_7 - g_9$ clock transition at 30 mT. Furthermore, they are both ZEFOZ transitions, and are thus protected from magnetic noise. Other qubit candidates involving g_8 and g_{16} are also possible, but the aforementioned candidates are most favourable. As seen in Figure 5.2, the recommended driving scheme for initialisation into g_{16} at 99 mT is $g_1 - e_1$ (-259 MHz) and $g_2 - e_2$ (-252 MHz), with σ_+ polarisation for $g_1 - e_1$ and linear polarisation for $g_2 - e_2$. Despite the linear polarisation, this still results in a state ρ fidelity of $F(\rho, g_{16}) > 0.921$. The reason linear polarisation is chosen for $g_2 - e_2$ is because one of the beams must be linearly polarised for optical readout on g_{14}, as is discussed further below. Seeing that $g_1 - e_1$ is the stronger initialising transition, it is kept polarised in σ_-. The recommended driving scheme for initialisation into g_8 is $g_9 - e_9$ (108 MHz, σ_- polarisation) and $g_{10} - e_{10}$ (-252 MHz, linear polarisation). The polarisations are chosen for the same reasons as for g_{16}. This results in a state ρ fidelity of $F(\rho, g_8) > 0.886$.

It is clear to see from the driving schemes, which do not include the static states g_8 and g_{16}, that this is a process reliant on the spin-relaxation of the system. Without the strong ES1 electronic spin flip processes, or the strong GS1 flip-flop processes, the excited states (e_1, e_2 and e_9, e_{10}) would not

---

[10]In Section 4, the optimal magnetic field found for $g_6 - g_8$ was 40 mT. This was determined using a different (now defunct) approach utilising the USRN and with the standard rates (i.e. no increased NSF, ESF rate coefficients).

relax into the respective static states. Since the populations (and hence fidelities) are calculated in the steady state, the initialisation is dependent on the longest relaxation timescale involved. The optical relaxation is on the order of 100 ns [60, 61], and the ES1 relaxation is on the order of 10 ns [79]. At 2 K, the GS1 spin-relaxation time T_1 is the longest timescale, since $T_1 \lesssim 1$ ms [73]. Thus, for this steady-state initialisation protocol, the lasers should be on sufficiently long enough to allow for a few cycles of GS1 relaxation (mediated primarily by the flip-flop). This means that the two lasers should be on for at least 1 ms. Therefore, a pulsed protocol where two lasers are simultaneously incident on the sample in 1 ms pulses can be implemented. After the 1 ms pulse, the system is initialised, and operations can be carried out on the qubit. The system is then optically read out.

The necessity of optical readout is why linear polarisation is required. At 2 K, circularly-polarised lasers can be used to increase the efficiency of initialisation. However, this circular polarisation will greatly suppress readout on the CP state. For example, σ_+ polarisation is used for g_{16} initialisation, but cannot be used for readout on g_{14} since $|\langle e_{14}|\mathcal{O}_+|g_{14}\rangle|^2 \sim 10^{-11}$. This makes it necessary for one of the lasers to be linearly polarised (using the previous example, $|\langle e_{14}|\mathcal{O}_{\text{opt}}|g_{14}\rangle|^2 > 0.99$). It is possible to keep both the initialisation lasers circularly-polarised by either introducing an additional readout laser, or by using a Pockels cell to quickly switch the polarisation of one of the initialisation lasers. Furthermore, cross transitions can also be used for readout, but these are weaker than direct transitions and so will result in a lower readout contrast. For the qubit candidate $g_{14} - g_{16}$ at 99 mT, the readout transition $g_{14} - e_{14}$ (260 MHz) can be used, while for $g_6 - g_8$ at 48 mT, the readout transition $g_6 - e_6$ (-56 MHz) can be used. Since the necessary operations have already been carried out on the qubit, the state fidelity does not need to be conserved after readout. In other words, it is not a problem if the readout has adverse effects on the system. This is in contrast to continuous-wave steady-state initialisation; since one beam acts as both an initialisation and readout beam, it is necessary that the readout does not negatively affect the system.

Initialisation at 100 mK with ES1 Spin Relaxation

The pulsed protocol recommended above, if initialising into g_{16}, can result in a state fidelity > 0.921. Tissot et al. [74] reported fidelities of > 0.999 for the same system, but at 100 mK. It was recommended in Section 4.1, that a temperature decrease can result in better control of the system, since the spin-relaxation rates are reduced. The temperature dependence of the system is characterised by the rate coefficients $\mathcal{R}$. These coefficients were only determined at 2 K, but since they also characterise T_1 times, a simplified temperature dependence can be modelled. Astner et al. [73] measured a $T_1 \sim 25$ s at 100 mK (using a dilution refrigerator) corresponding to a spin relaxation rate of $\overline{\gamma}_g \sim 10^{-8}$ MHz. The simulation models the spin relaxation to be mediated by four distinct processes (x: ESF, NSF, FF, FFz) with the individual rates $\gamma_g \equiv \gamma_{g_j - g_k}$ given by Eq. (2.12). Since the strongest relaxation probabilities $|\langle O_x\rangle|^2 \sim 0.1$ the GS1 rate coefficients can be approximated by $\mathcal{R}^g \equiv \mathcal{R}^g_x \sim \overline{\gamma}_g/|\langle O_x\rangle|^2 \sim {}^{10^{-8}}\!/_{0.1}$ MHz $= 10^{-7}$ MHz. Of course, this approximation does not incorporate other important experimental and environmental factors (such as the magnetic field), but is sufficient to obtain an order of magnitude estimate for the fidelity at these temperatures. Setting all the GS1 rate coefficients $\mathcal{R}^g = 10^{-7}$ MHz resulted in an overall increase of fidelities. However, new protocols had to be introduced. Note that experimental considerations, such as using a linear polarisation for optical readout, are not considered for brevity.

Due to time limitations, not all magnetic fields could be studied. Therefore, the effect of reducing $\mathcal{R}^g$ to 10^{-7} MHz was only studied for initialisation into g_{16} at 99 mT (with σ_+ polarisation) and g_8 at 48 mT (with σ_- polarisation) for the detuning range of -5000 to 5000 MHz, to include large

transition energies.[11] For initialisation into g_{16}, the fixed laser was set to $\delta_F = -259$ MHz (the prominent initialisation detuning in the 2 K case, see Figures 5.2a, b) corresponding to the $g_1 - e_1$ transition. The fidelity reached $F(\rho, g_{16}) > 0.997$ at $\delta_S = -3291$ MHz, corresponding to the $g_{15} - e_1$ transition $\left(|\langle e_1|\mathcal{O}_+|g_{15}\rangle|^2 \sim 5 \cdot 10^{-3}\right)$. For initialisation into g_8, the fixed laser was set to $\delta_F = 108$ MHz (corresponds to $g_9 - e_9$) with a maximum fidelity of $F(\rho, g_8) > 0.998$ at $\delta_S = 709$ MHz, corresponding to the $g_7 - e_9$ transition $\left(|\langle e_9|\mathcal{O}_-|g_7\rangle|^2 \sim 0.1\right)$. Figure 5.3a shows this schematically. It can be seen immediately that these initialisation driving schemes are all mediated via the ES1 electronic spin flip and optical relaxation. Since the GS1 flip-flop is now heavily suppressed, the relaxation processes $g_{15} \xrightarrow[\text{FF}]{} g_1$ (Figure 5.2b) and $g_7 \xrightarrow[\text{FF}]{} g_9$ (Figure 5.2d) which formed an integral part of the 2 K protocols, are not strong enough for good initialisation. Despite the high fidelities, it must be noted that these are Λ-schemes. Λ-schemes can lead to coherent population trapping (CPT), wherein the system goes into a dark state which is a superposition of the two GS1 eigenstates (g_1, g_{15} or g_7, g_9) being driven - this is not favourable for initialisation into g_8 or g_{16}. CPT is not considered nor included in the model, meaning that this initialisation protocol might not be entirely reliable. CPT might be able to be avoided by pulsing the lasers in an alternating fashion (one laser on, other laser off, vice versa) over the necessary timescale needed for initialisation. However, due to the relaxation of states resonant with the off-laser, this could increase the time needed to reach the steady state. Seeing as this initialisation combines both ES1 and optical relaxation, and that one of the driving transitions is a cross transition (weaker than direct transitions, $|\langle\mathcal{O}\rangle|^2 < 0.9$), steady-state initialisation is likely to be achieved on the order of 1 μs, allowing for several cycles of driving, ES1 relaxation (lifetime $\sim$ 10 ns), and optical relaxation (lifetime $\sim$ 100 ns).

Initialisation at 100 mK without ES1 Spin Relaxation

In reality, by reducing the temperature to 100 mK, the relaxation rates in ES1 $\gamma_e \equiv \gamma_{e_i - e_j}$ are also bound to change, since the energy separations of the ES1 eigenstates are on the same order of magnitude as the energy separations of the GS1 eigenstates ($\sim$ 100 MHz). The temperature dependence of γ_e is not known, and the relation between γ_g and γ_e is likely nonlinear. Therefore, no concrete conclusions can be made here regarding 100 mK fidelities. However, it is possible to use an approach similar to Tissot et al., where the relaxation within ES1 is ignored, by setting the ES1 rate coefficients $\mathcal{R}^e \equiv \mathcal{R}^e_{\text{x}} = 0$ (and keeping $\mathcal{R}^g = 10^{-7}$). Since now both the GS1 and ES1 relaxation processes are suppressed, the protocol must rely on optical relaxation. Using the same parameters (g_8: 48 mT, σ_- polarisation and g_{16}: 99 mT, σ_+ polarisation), a fidelity of $F(\rho, g_{16}) > 0.998$ can be achieved using the driving scheme $g_1 - e_{16}$ (3407 MHz, $|\langle e_{16}|\mathcal{O}_+|g_1\rangle|^2 \sim 10^{-3}$) and $g_{15} - e_{16}$ (-3291 MHz, $|\langle e_{16}|\mathcal{O}_+|g_{15}\rangle|^2 \sim 10^{-6}$). The driving scheme $g_9 - e_8$ (-595 MHz, $|\langle e_8|\mathcal{O}_-|g_9\rangle|^2 \sim 10^{-2}$) and $g_7 - e_8$ (6 MHz, $|\langle e_8|\mathcal{O}_-|g_9\rangle|^2 \sim 10^{-3}$) results in a fidelity of $F(\rho, g_8) > 0.999$. Figure 5.3b shows this schematically. Unsurprisingly, the transitions used in the g_8 (g_{16}) driving scheme have the largest optical driving probabilities $|\langle\mathcal{O}_-\rangle|^2$ ($|\langle\mathcal{O}_+\rangle|^2$) for all optical transitions between g_i and e_8 (e_{16}), excluding the direct transition $g_8 \to e_8$ ($g_{16} \to e_{16}$) which would deplete g_8 (g_{16}). The g_8 driving scheme also has larger driving probabilities as compared to g_{16}, resulting in better initialisation.

Similar to the 100 mK process outlined previously, these driving schemes are also Λ-schemes, and could lead to CPT. Same as before, CPT can be avoided by using alternating pulsed lasers. Seeing as this is almost a purely optical process (with very little contribution from GS1 relaxation and no contribution from ES1 relaxation) involving optical driving transitions that are even weaker than before, the time at which the steady state is reached is likely to be on the order of 10 μs. This will ensure several hundred optical excitation and relaxation cycles (optical lifetime is $\sim$ 100 ns), while

---

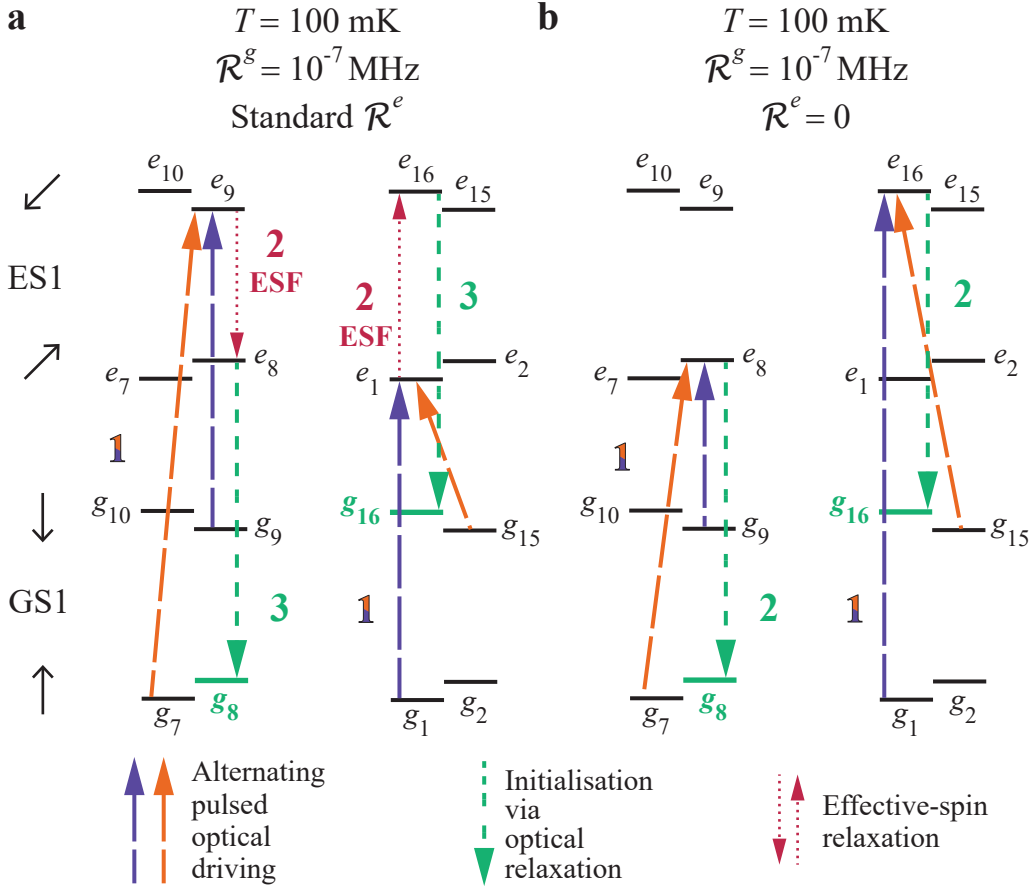[11]This detuning range was not used for the general $0 - 99$ mT analysis due to computational limits.

Figure 5.3: **a** Initialisation driving and relaxation scheme for g_8 and g_6 with GS1 rate coefficients $\mathcal{R}^g = 10^{-7}$ (reflecting 100 mK T_1) and standard ES1 rate coefficients $\mathcal{R}^e$ (Appendix B.I). The lasers are pulsed in an alternating fashion (dashed lines represent alternating pulses) to prevent coherent population trapping (CPT). Note that with GS1 relaxation now suppressed, the best initialisation scheme does not include the GS1 flip-flop, as opposed to the 2 K case. **b** Initialisation driving and relaxation scheme for g_8 and g_{16} with GS1 rate coefficients $\mathcal{R}^g = 10^{-7}$ and ES1 rate coefficients $\mathcal{R}^e = 0$. Same as before, the lasers are pulsed in an alternating fashion to prevent CPT. Now with ES1 relaxation suppressed, the initialisation scheme is purely optical (i.e. no effective-spin relaxation).

still allowing for a small amount of GS1 relaxation to contribute to the initialisation.[12] The maximum fidelity attained here is very similar to that of Tissot et al. [74], and when considering that the two approaches used were quite different (Tissot et al. use a ratchet-type time-resolved method involving a repump for initialisation, as opposed to two-laser steady-state), is a promising indication that good initialisation is possible for V defects in SiC. Currently, the temperature of the ES1 spin-relaxation time has not been characterised. It is therefore not possible to make any definitive conclusions on the 100 mK cases. However, if the GS1 spin-relaxation time has been experimentally measured to increase between 2 K and 100 mK (by 10^3 orders of magnitude), it is not unreasonable to suppose that something similar happens to the ES1 lifetime. In this way, the latter case ($\mathcal{R}_x^e = 0$) is likely to be the most physically accurate.

---

[12]Due to the population imbalance between the GS1 eigenstates which are driven, and the other GS1 eigenstates, GS1 relaxation will be directed into the driven eigenstates. Normally this process is slow at 100 mK, but the population imbalance helps to speed it up. Furthermore, the finite optical linewidth (~ 10 MHz) causes several transitions to be driven simultaneously, further accelerating initialisation.

Summary of Observed Trends

On a final note, it is interesting to see how the initialisation driving scheme changes significantly depending on the temperature. At 2 K, since the GS1 flip-flop is prominent, the initialisation scheme drives direct transitions in the spin-manifold opposite to the static state. For g_{16} this was $g_1 - e_1$, $g_2 - e_2$ and for g_8 this was $g_9 - e_9$, $g_{10} - e_{10}$. These are Π-schemes with very strong optical driving probabilities $|\langle \mathcal{O}_{\mathrm{opt},\pm} \rangle|^2$. The $g_2 - e_2$ and $g_{10} - e_{10}$ transitions can only initialise with the aid of the GS1 flip-flop (see Figures 5.2b, d). Suppressing the GS1 relaxation means that the $g_2 - e_2$ and $g_{10} - e_{10}$ transitions are no longer useful in initialisation. The driving scheme then becomes a Λ-scheme, where the excited eigenstate initialises into the static state via the ES1 electronic spin flip and optical relaxation. Suppressing both GS1 and ES1 led to driving schemes where the excited state analog e_i of the static state g_i was directly populated. These schemes are not possible when GS1 and ES1 relaxation is prominent. Both the 100 mK cases (suppressed spin relaxation) led to initialisation using Λ-schemes, which can lead to CPT. While CPT was not included in the model, it might be possible to avoid this experimentally by pulsing the lasers in an alternating fashion over the necessary initialisation timescale. Despite this, the presence of Λ-schemes at low temperatures could possibly be advantageous. Upon further analysis, it may be possible to use CPT to initialise the system for another qubit candidate, not unlike what has been done for NV centres in diamond [86, 87] and quantum dots [88]. Coherent population trapping has also been seen with molybdenum spins [89] and divacancies [90] in SiC, although not for initialisation purposes.

6   Conclusion

This work aimed to develop initialisation protocols for the neutral charge-state V^{4+} defect in SiC at 2 K, to achieve high-fidelity initialisation for coherent control. These protocols were developed with the use of a theoretical Lindbladian model, which was used to simulate the eigenstate populations of the quantum system. For an inhomogeneous ensemble, no theoretical initialisation protocol with a fidelity of $F > 0.1$ was found. This strongly suggests that inhomogeneous ensembles of V defects in SiC are not a good candidate for quantum memory applications, where much higher fidelities are required. Furthermore, in experiment, the one-laser (uninitialised) signal was higher than the two-laser (initialised) signal. Possible reasons for this signal difference were given, but have yet to be verified. Despite this signal difference and the low fidelities, the simulation was able to accurately predict (accuracy of ± 10 MHz) points of two-laser initialised spin resonance which were experimentally verified using a vanadium-doped SiC sample with inhomogeneous broadening of ~ 20 GHz at 2 K. This motivated using the model to develop theoretical single-defect initialisation protocols.

At the single-defect level, an analysis in the range $0 - 99$ mT found that below 34 mT, where the hyperfine interaction still has a significant contribution to the Hamiltonian, there were no qubit candidates with a population contrast $\Delta P \geq 75\%$. This suggests that the pure hyperfine and mixed hyperfine-electron Zeeman regimes have relaxation pathways which are too strong for good initialisation. Therefore, any initialisation protocol should be focused on the electron Zeeman dominated regime ($\gtrsim 30$ mT). Within this regime, there were two GS1 eigenstates, g_8 ($|\uparrow, -7/2\rangle$) and g_{16} ($|\downarrow, 7/2\rangle$), that could be initialised well with a steady-state two-laser protocol. At 2 K, the maximum fidelities achieved were $F(\rho, g_8) > 0.886$ and $F(\rho, g_{16}) > 0.921$, using Π-schemes, with different requirements for the magnetic field and laser frequencies. An analysis on the spin-state dynamics of GS1 and ES1 found that at 2 K, any steady-state initialisation protocol heavily relies on the spin relaxation within GS1 and ES1. Furthermore, which state (between g_8 and g_{16}) the system would initialise into was found to be dependent on which effective-spin manifolds the applied optical fields were driving. Due to the fact that circular polarisation amplifies transitions for a specific effective-spin manifold, and suppresses transitions in the other, circularly-polarised light was utilised in the initialisation. Since the initialisation protocol at 2 K relies on GS1 relaxation, which has the longest relaxation time ($\lesssim 1$ ms [73]), a pulsed initialisation protocol would require pulses of at least 1 ms to obtain steady-state conditions. An approximated temperature dependence of the GS1 and ES1 relaxation rates was also developed, and at 100 mK, fidelities of $F > 0.999$ were achieved. While not determined with a rigorous method, this result is very similar to that of Tissot et al. [74]. When considering that the two approaches used were quite different, it is a promising indication that good initialisation can be achieved for V defects in SiC.

It was found, in both experiment and simulation, that steady-state two-laser initialisation protocols for V defects in SiC are highly dependent on spin relaxation (and hence temperature), incident laser polarisation, and the degree of inhomogeneity in the system. For quantum technology applications, inhomogeneous ensembles cannot be used owing to their low state fidelities, even after attempted initialisation. The single-defect case was more promising however, showing theoretical fidelities of up to $F > 0.921$ at 2 K. Although fidelities of $F > 0.999$ are extremely favourable for quantum technology applications, it seems that these fidelities are only achievable with very low temperatures, on the order of 100 mK, requiring the use of dilution refrigerators. This is a less practical, and more expensive, operating temperature than 2 K. A single-defect fidelity of $F > 0.921$ at 2 K is suitable for use in quantum repeater applications [32], and also indicates that high initialisation can be achieved at more practical operating temperatures and without the use of dilution refrigerators. Further studies to fully quantify the dependence of all the spin-relaxation processes (GS1 and ES1)

on experimental factors (temperature, number and power of incident electric and magnetic fields), along with an analysis over a larger range of magnetic fields and laser frequencies, may help lead to previously undiscovered areas of high-fidelity initialisation at 2 K. It was also found that the high-fidelity states g_8 and g_{16} each formed qubit candidates with states that have an effective $\Delta m_I = 2$ transition. Initialised spin resonance was experimentally measured for one of these qubit candidates ($g_6 - g_8$), but unfortunately no coherence was seen, which is a fundamental requirement for qubits. These $\Delta m_I = 2$ transitions arise from the nuclear electric quadrupole, indicating that it might be necessary to use electric fields to coherently drive this transition. In fact, achieving highly-initialised coherent control with electric fields is a sought after feat in the community [62]. This could be investigated further by applying electric fields and studying the initialised coherence properties of these qubit candidates.

While this work is by no means an exhaustive guideline for high-fidelity initialisation, it has provided valuable insight into the complicated dynamics of V defects in SiC. Most importantly, it provides a framework for the community to achieve high-fidelity initialisation of V defects in SiC at 2 K. Through these high-fidelity initialisation protocols, this work enables experimental study of the coherence properties of individual vanadium defects at 2 K.

References

[1] B. Schumacher, "Quantum coding," *Physical Review A*, vol. 51, pp. 2738–2747, 4 Apr. 1995.

[2] J. Preskill, "Quantum computing and the entanglement frontier," 2012, **arXiv**.2205.12862. [Online]. Available: `https://arxiv.org/abs/1203.5813` Accessed: 28/4/2023.

[3] F. Arute *et al.*, "Quantum supremacy using a programmable superconducting processor," *Nature*, vol. 574, pp. 505–510, 2019.

[4] H.-S. Zhong *et al.*, "Quantum computational advantage using photons," *Science*, vol. 370, no. 6523, pp. 1460–1463, 2020.

[5] H.-S. Zhong *et al.*, "Phase-programmable gaussian boson sampling using stimulated squeezed light," *Physical Review Letters*, vol. 127, no. 18, p. 180 502, 2021.

[6] L. S. Madsen *et al.*, "Quantum computational advantage with a programmable photonic processor," *Nature*, vol. 606, no. 7912, pp. 75–81, 2022.

[7] H. J. Kimble, "The quantum internet," *Nature*, vol. 453, no. 7198, pp. 1023–1030, 2008.

[8] P. Jouguet, S. Kunz-Jacques, A. Leverrier, P. Grangier, and E. Diamanti, "Experimental demonstration of long-distance continuous-variable quantum key distribution," *Nature Photonics*, vol. 7, no. 5, pp. 378–381, 2013.

[9] H.-K. Lo, M. Curty, and B. Qi, "Measurement-device-independent quantum key distribution," *Physical Review Letters*, vol. 108, no. 13, p. 130 503, 2012.

[10] H. Buhrman and H. Röhrig, "Distributed quantum computing," in *Mathematical Foundations of Computer Science 2003: 28th International Symposium, MFCS 2003, Bratislava, Slovakia, August 25-29, 2003. Proceedings 28*, Springer, 2003, pp. 1–20.

[11] R. Beals *et al.*, "Efficient distributed quantum computing," *Proceedings of the Royal Society A: Mathematical, Physical and Engineering Sciences*, vol. 469, no. 2153, p. 20 120 686, 2013.

[12] P. Komar *et al.*, "A quantum network of clocks," *Nature Physics*, vol. 10, no. 8, pp. 582–587, 2014.

[13] D. Gottesman, T. Jennewein, and S. Croke, "Longer-baseline telescopes using quantum repeaters," *Physical Review Letters*, vol. 109, no. 7, p. 070 503, 2012.

[14] R. Malaney, "The quantum car," *IEEE Wireless Communications Letters*, vol. 5, no. 6, pp. 624–627, 2016.

[15] Y. Yu *et al.*, "Entanglement of two quantum memories via fibres over dozens of kilometres," *Nature*, vol. 578, no. 7794, pp. 240–245, 2020.

[16] D.-C. Liu *et al.*, "On-demand storage of photonic qubits at telecom wavelengths," *Physical Review Letters*, vol. 129, no. 21, p. 210 501, 2022.

[17] D. Bouwmeester, J.-W. Pan, K. Mattle, M. Eibl, H. Weinfurter, and A. Zeilinger, "Experimental quantum teleportation," *Nature*, vol. 390, no. 6660, pp. 575–579, 1997.

[18] J.-G. Ren *et al.*, "Ground-to-satellite quantum teleportation," *Nature*, vol. 549, no. 7670, pp. 70–73, 2017.

[19] A. Kržič *et al.*, "Metropolitan free-space quantum networks," 2022, **arXiv**:2205.12862. [Online]. Available: `https://arxiv.org/abs/2205.12862` Accessed: 28/4/2023.

[20] T.-Y. Chen *et al.*, "Implementation of a 46-node quantum metropolitan area network," *npj Quantum Information*, vol. 7, no. 1, p. 134, 2021.

[21] J. Dynes *et al.*, "Cambridge quantum network," *npj Quantum Information*, vol. 5, no. 1, p. 101, 2019.

[22] J. Yin *et al.*, "Entanglement-based secure quantum cryptography over 1,120 kilometres," *Nature*, vol. 582, no. 7813, pp. 501–505, 2020.

[23] R. Van Meter, *Quantum networking*. John Wiley & Sons, 2014.

[24] M. Körber, O. Morin, S. Langenfeld, A. Neuzner, S. Ritter, and G. Rempe, "Decoherence-protected memory for a single-photon qubit," *Nature Photonics*, vol. 12, no. 1, pp. 18–21, 2018.

[25] M. Brekenfeld, D. Niemietz, J. D. Christesen, and G. Rempe, "A quantum network node with crossed optical fibre cavities," *Nature Physics*, vol. 16, no. 6, pp. 647–651, 2020.

[26] W. K. Wootters and W. H. Zurek, "A single quantum cannot be cloned," *Nature*, vol. 299, pp. 802–803, 1982.

[27] W. J. Munro, K. Azuma, K. Tamaki, and K. Nemoto, "Inside quantum repeaters," *IEEE Journal of Selected Topics in Quantum Electronics*, vol. 21, no. 3, pp. 78–90, 2015.

[28] W. Munro, K. Harrison, A. Stephens, S. Devitt, and K. Nemoto, "From quantum fusiliers to high-performance networks," 2009, **arXiv**:0910.4038. [Online]. Available: https://arxiv.org/pdf/0910.4038.pdf Accessed: 29/4/2023.

[29] L. Jiang, J. M. Taylor, K. Nemoto, W. J. Munro, R. Van Meter, and M. D. Lukin, "Quantum repeater with encoding," *Physical Review A*, vol. 79, no. 3, p. 032 325, 2009.

[30] N. Sangouard, C. Simon, H. De Riedmatten, and N. Gisin, "Quantum repeaters based on atomic ensembles and linear optics," *Reviews of Modern Physics*, vol. 83, no. 1, p. 33, 2011.

[31] H.-J. Briegel, W. Dür, J. I. Cirac, and P. Zoller, "Quantum repeaters: The role of imperfect local operations in quantum communication," *Physical Review Letters*, vol. 81, no. 26, p. 5932, 1998.

[32] L.-M. Duan, M. D. Lukin, J. I. Cirac, and P. Zoller, "Long-distance quantum communication with atomic ensembles and linear optics," *Nature*, vol. 414, no. 6862, pp. 413–418, 2001.

[33] K. Azuma, K. Tamaki, and H.-K. Lo, "All-photonic quantum repeaters," *Nature communications*, vol. 6, no. 1, p. 6787, 2015.

[34] L. Childress, J. Taylor, A. S. Sørensen, and M. D. Lukin, "Fault-tolerant quantum repeaters with minimal physical resources and implementations based on single-photon emitters," *Physical Review A*, vol. 72, no. 5, p. 052 330, 2005.

[35] N. Sangouard, R. Dubessy, and C. Simon, "Quantum repeaters based on single trapped ions," *Physical Review A*, vol. 79, no. 4, p. 042 340, 2009.

[36] K. Azuma, H. Takeda, M. Koashi, and N. Imoto, "Quantum repeaters and computation by a single module: Remote nondestructive parity measurement," *Physical Review A*, vol. 85, no. 6, p. 062 309, 2012.

[37] M. Zwerger, W. Dür, and H. Briegel, "Measurement-based quantum repeaters," *Physical Review A*, vol. 85, no. 6, p. 062 326, 2012.

[38] M. Zukowski, A. Zeilinger, M. A. Horne, and A. K. Ekert, ""Event-ready-detectors" Bell experiment via entanglement swapping," *Physical Review Letters*, vol. 71, no. 26, 1993.

[39] P. Van Loock *et al.*, "Hybrid quantum repeater using bright coherent light," *Physical Review Letters*, vol. 96, no. 24, p. 240 501, 2006.

[40] O. Collins, S. Jenkins, A. Kuzmich, and T. Kennedy, "Multiplexed memory-insensitive quantum repeaters," *Physical Review Letters*, vol. 98, no. 6, p. 060 502, 2007.

[41] L. Jiang, J. M. Taylor, N. Khaneja, and M. D. Lukin, "Optimal approach to quantum communication using dynamic programming," *Proceedings of the National Academy of Sciences*, vol. 104, no. 44, pp. 17 291–17 296, 2007.

[42] J.-W. Pan, S. Gasparoni, R. Ursin, G. Weihs, and A. Zeilinger, "Experimental entanglement purification of arbitrary unknown states," *Nature*, vol. 423, no. 6938, pp. 417–422, 2003.

[43] R. Reichle *et al.*, "Experimental purification of two-atom entanglement," *Nature*, vol. 443, no. 7113, pp. 838–841, 2006.

[44] J. F. Sherson *et al.*, "Quantum teleportation between light and matter," *Nature*, vol. 443, no. 7111, pp. 557–560, 2006.

[45] Z.-S. Yuan, Y.-A. Chen, B. Zhao, S. Chen, J. Schmiedmayer, and J.-W. Pan, "Experimental demonstration of a BDCZ quantum repeater node," *Nature*, vol. 454, no. 7208, pp. 1098–1101, 2008.

[46] M. Shapiro and P. Brumer, "Coherent control of atomic, molecular, and electronic processes," in *Advances in Atomic, Molecular, and Optical Physics*, vol. 42, Elsevier, 2000, pp. 287–345.

[47] M. W. Doherty, N. B. Manson, P. Delaney, F. Jelezko, J. Wrachtrup, and L. C. Hollenberg, "The nitrogen-vacancy colour centre in diamond," *Physics Reports*, vol. 528, no. 1, pp. 1–45, 2013.

[48] M. G. Dutt *et al.*, "Quantum register based on individual electronic and nuclear spin qubits in diamond," *Science*, vol. 316, no. 5829, pp. 1312–1316, 2007.

[49] F. Jelezko, T. Gaebel, I. Popa, M. Domhan, A. Gruber, and J. Wrachtrup, "Observation of coherent oscillation of a single nuclear spin and realization of a two-qubit conditional quantum gate," *Physical Review Letters*, vol. 93, no. 13, p. 130 501, 2004.

[50] J. Weber *et al.*, "Quantum computing with defects," *Proceedings of the National Academy of Sciences*, vol. 107, no. 19, pp. 8513–8518, 2010.

[51] F. Jelezko and J. Wrachtrup, "Single defect centres in diamond: A review," *Physica Status Solidi (a)*, vol. 203, no. 13, pp. 3207–3225, 2006.

[52] L. Rogers, S. Armstrong, M. Sellars, and N. Manson, "Infrared emission of the NV centre in diamond: Zeeman and uniaxial stress studies," *New Journal of Physics*, vol. 10, no. 10, p. 103 024, 2008.

[53] X. Cao, M. Zopf, and F. Ding, "Telecom wavelength single photon sources," *Journal of Semiconductors*, vol. 40, no. 7, p. 071 901, 2019.

[54] G. Keiser, *Fiber Optic Communications*. Springer, 2021.

[55] A. Dréau, A. Tchebotareva, A. El Mahdaoui, C. Bonato, and R. Hanson, "Quantum frequency conversion of single photons from a nitrogen-vacancy center in diamond to telecommunication wavelengths," *Physical Review Applied*, vol. 9, no. 6, p. 064 031, 2018.

[56] R. Ikuta *et al.*, "Frequency down-conversion of 637 nm light to the telecommunication band for non-classical light emitted from NV centers in diamond," *Optics Express*, vol. 22, no. 9, pp. 11 205–11 214, 2014.

[57] M. Kunzer, H. Müller, and U. Kaufmann, "Magnetic circular dichroism and site-selective optically detected magnetic resonance of the deep amphoteric vanadium impurity in 6H-SiC," *Physical Review B*, vol. 48, no. 15, p. 10 846, 1993.

[58] L. J. Anthony, *Sublimation process for manufacturing silicon carbide crystals*, US Patent 2, 854, 364, 1958.

[59] N. Ohtani, T. Fujimoto, T. Aigo, M. Katsuno, H. Tsuge, and H. Yashiro, "Large high-quality silicon carbide single crystal substrates," *Nippon Steel Technical Report. Overseas*, no. 84, pp. 36–41, 2001.

[60] L. Spindlberger *et al.*, "Optical properties of vanadium in 4H silicon carbide for quantum technology," *Physical Review Applied*, vol. 12, no. 1, p. 014 015, 2019.

[61] G. Wolfowicz, C. P. Anderson, B. Diler, O. G. Poluektov, F. J. Heremans, and D. D. Awschalom, "Vanadium spin qubits as telecom quantum emitters in silicon carbide," *Science Advances*, vol. 6, no. 18, eaaz1192, 2020.

[62] J. Hendriks, C. M. Gilardoni, C. Adambukulam, A. Laucht, and C. H. van der Wal, "Coherent spin dynamics of hyperfine-coupled vanadium impurities in silicon carbide," 2022, **arXiv**:2210. 09942 (preprint). [Online]. Available: `https://arxiv.org/pdf/2210.09942.pdf` Accessed: 29/11/2022.

[63] P. V. Klimov, A. L. Falk, D. J. Christle, V. V. Dobrovitski, and D. D. Awschalom, "Quantum entanglement at ambient conditions in a macroscopic solid-state spin ensemble," *Science Advances*, vol. 1, no. 10, e1501015, 2015.

[64] M. Gulka *et al.*, "Room-temperature control and electrical readout of individual nitrogen-vacancy nuclear spins," *Nature Communications*, vol. 12, no. 1, p. 4421, 2021.

[65]   M. Abobeih *et al.*, "Atomic-scale imaging of a 27-nuclear-spin cluster using a quantum sensor," *Nature*, vol. 576, no. 7787, pp. 411–415, 2019.

[66]   M. T. Uysal *et al.*, "Coherent control of a nuclear spin via interactions with a rare-earth ion in the solid state," *PRX Quantum*, vol. 4, no. 1, p. 010 323, 2023.

[67]   J. Baur, M. Kunzer, and J. Schneider, "Transition metals in SiC polytypes, as studied by magnetic resonance techniques," *Physica Status Solidi (a)*, vol. 162, no. 1, pp. 153–172, 1997.

[68]   B. Tissot and G. Burkard, "Spin structure and resonant driving of spin-1/2 defects in SiC," *Physical Review B*, vol. 103, no. 6, p. 064 106, 2021.

[69]   B. Tissot and G. Burkard, "Hyperfine structure of transition metal defects in SiC," *Physical Review B*, vol. 104, no. 6, p. 064 102, 2021.

[70]   C. M. Gilardoni, I. Ion, F. Hendriks, M. Trupke, and C. H. van der Wal, "Hyperfine-mediated transitions between electronic spin-1/2 levels of transition metal defects in SiC," *New Journal of Physics*, vol. 23, no. 8, p. 083 010, 2021.

[71]   A. Csóré and A. Gali, "Ab initio determination of pseudospin for paramagnetic defects in SiC," *Physical Review B*, vol. 102, no. 24, p. 241 201, 2020.

[72]   C. Maia Gilardoni, "Optically addressable spins in silicon carbide and related 2D materials," Ph.D. dissertation, University of Groningen, 2021.

[73]   T. Astner *et al.*, "Vanadium in silicon carbide: Telecom-ready spin centres with long relaxation lifetimes and hyperfine-resolved optical transitions," 2022, **arXiv**:2206.06240 (preprint). [Online]. Available: `https://arxiv.org/pdf/2206.06240.pdf` Accessed: 27/1/2023.

[74]   B. Tissot, M. Trupke, P. Koller, T. Astner, and G. Burkard, "Nuclear spin quantum memory in silicon carbide," *Physical Review Research*, vol. 4, no. 3, p. 033 107, 2022.

[75]   J. R. De Laeter *et al.*, "Atomic weights of the elements. Review 2000 (IUPAC Technical Report)," *Pure and Applied Chemistry*, vol. 75, no. 6, pp. 683–800, 2003.

[76]   G. Audi, O. Bersillon, J. Blachot, and A. H. Wapstra, "The nubase evaluation of nuclear and decay properties," *Nuclear Physics A*, vol. 729, no. 1, pp. 3–128, 2003.

[77]   S. Asaad *et al.*, "Coherent electrical control of a single high-spin nucleus in silicon," *Nature*, vol. 579, no. 7798, pp. 205–209, 2020.

[78]   P. Cilibrizzi *et al.*, "Ultra-narrow inhomogeneous spectral distribution of telecom-wavelength vanadium centres in isotopically-enriched silicon carbide," 2023, **arXiv**:2305.01757 (preprint). [Online]. Available: `https://arxiv.org/pdf/2305.01757.pdf` Accessed: 3/5/2023.

[79]   C. Gilardoni, J. Hendriks, and C. van der Wal, work in preparation, 2023.

[80]   H.-P. Breuer, F. Petruccione, *et al.*, *The Theory of Open Quantum Systems*. Oxford University Press on Demand, 2002.

[81]   E. Gentzsch. "Thor Labs: Polarization Handedness Convention." (2007), [Online]. Available: `https://www.thorlabs.com/images/Tabimages/Polarization_Handedness_Tutorial.pdf` Accessed: 15/4/2023.

[82]   M. A. Nielsen and I. Chuang, *Quantum Computation and Quantum Information*, 2002.

[83]   C. P. Anderson *et al.*, "Electrical and optical control of single spins integrated in scalable semiconductor devices," *Science*, vol. 366, no. 6470, pp. 1225–1230, 2019.

[84]   A. Noiri *et al.*, "Fast universal quantum control above the fault-tolerance threshold in silicon," **arXiv**:2108.02626 (preprint). [Online]. Available: `https://arxiv.org/ftp/arxiv/papers/2108/2108.02626.pdf` Accessed: 30/4/2023.

[85]   J. Hendriks, private communication, May 2023.

[86]   C. Santori *et al.*, "Coherent population trapping of single spins in diamond under optical excitation," *Physical Review Letters*, vol. 97, no. 24, p. 247 401, 2006.

[87]   D. A. Golter, K. N. Dinyari, and H. Wang, "Nuclear-spin-dependent coherent population trapping of single nitrogen-vacancy centers in diamond," *Physical Review A*, vol. 87, no. 3, p. 035 801, 2013.

[88]   X. Xu *et al.*, "Coherent population trapping of an electron spin in a single negatively charged quantum dot," *Nature Physics*, vol. 4, no. 9, pp. 692–695, 2008.

[89]   T. Bosma *et al.*, "Identification and tunable optical coherent control of transition-metal spins in silicon carbide," *npj Quantum Information*, vol. 4, no. 1, p. 48, 2018.

[90]   O. V. Zwier, D. O'Shea, A. R. Onur, and C. H. Van Der Wal, "All-optical coherent population trapping with defect spin ensembles in silicon carbide," *Scientific Reports*, vol. 5, no. 1, p. 10 931, 2015.

[91]   R. D. Worley, M. Zemansky, and H. Boorse, "Heat capacities of vanadium and tantalum in the normal and superconducting phases," *Physical Review*, vol. 99, no. 2, p. 447, 1955.

Appendix

Initialisation Protocols for Quantum Memory Writing with Vanadium Defects in Silicon Carbide

Appendix to the Master's thesis, '*Initialisation Protocols for Quantum Memory Writing with Vanadium Defects in Silicon Carbide*' (2023) by Adrian P.J. Sidhu. Written for the MSc Physics: Quantum Universe programme at the University of Groningen.

Contents

A Appendices to Section 2: Theoretical Overview

A.I Effective Inhomogeneity

Each defect is situated in a different part of the 4H-SiC crystal lattice and feels differing electrostatic inhomogeneities arising from lattice imperfections and other environmental factors. These inhomogeneities result in unique changes in the energy structure of the different defects, and as such causes an inhomogeneous broadening of the GS1−ES1 optical transition linewidth (i.e. transition energy). In the sample studied here, the broadening is on the order of roughly 20 GHz. The consequence of this is that the same laser frequency can be resonant with different transitions between the defects, and the overall energy resolution decreases. However, the effective inhomogeneity is on the order of a few GHz. This is because the energy difference ΔE_{ES1} between e_1 and e_{16} from 0 to 99 mT is between $1-4$ GHz. Thus, a laser with frequency ω resonant with some transition $g_i - e_j$ in one defect can only be simultaneously resonant with a transtion $g_k - e_l$ in another defect if the inhomogeneous broadening Δ between the two defects is $\Delta \lesssim \Delta E_{\text{ES1}}$. Otherwise, another part of the inhomogeneous ensemble is accessed, where the same rule applies. This means that at any one time, the lasers are accessing an ensemble of defects which have an effective inhomogeneous broadening of $1-3$ GHz. In the magnetic field range studied, the difference between e_1 and e_{16} is always larger than the difference between g_1 and g_{16}, which makes the ES1 difference the limiting factor in the inhomogeneity. This can be seen in Figure A.1. The inhomogeneity range used in the simulation was -1 GHz to 1 GHz. The range was kept relatively small to maximise computational efficiency.

A.II Derivation of a Four-Level Lindbladian

As mentioned prior, the system is calculated in the steady state, that is

$$\dot{\rho} = 0. \tag{A.1}$$

Since it is assumed that there are no coherences, so that ρ is only composed of diagonal terms (populations), ρ can be replaced with a 32-entry column vector $\vec{\rho}_{\text{diag}}$. Explicitly

$$\rho = \text{diag}(\vec{P}) \rightarrow \vec{\rho}_{\text{diag}} = \vec{P}^{\text{T}} = (P_{g_1}, \ P_{g_2}, \ldots, P_{e_{16}})^{\text{T}} = (P_1, \ P_2, \ \ldots, \ P_{32})^{\text{T}} \tag{A.2}$$

where the subscripts g_j, e_j have been replaced with $i = 1, \ldots, 32$ for brevity. Replacing the 32×32 matrix ρ with a 32-entry vector $\vec{\rho}_{\text{diag}}$ makes it more (computationally) efficient to solve for the populations. In this way, Eq. (A.1) is a system of 32 linear differential equations (DEs). The evolution of an open quantum system (a system that interacts with its environment) is governed by the master Lindblad equation [80], given by

$$\dot{\rho} = \mathcal{L}\rho \tag{A.3}$$

where $\mathcal{L}$ is the Lindbladian. For the system studied here, the Lindbladian $\mathcal{L}$ can be represented by a 32×32 matrix M. Eqs. (A.1), (A.2), and (A.3) can then be combined to give

$$M\vec{\rho}_{\text{diag}} = \vec{0}. \tag{A.4}$$

Eq. (A.4) is the foundation of the theoretical model used in this research. Now, instead of 32 linear ODEs, Eq. (A.4) is a system of 32 linear equations. To determine the populations ρ, the matrix M must first be constructed. From there, Eq. (A.4) can be rearranged to give
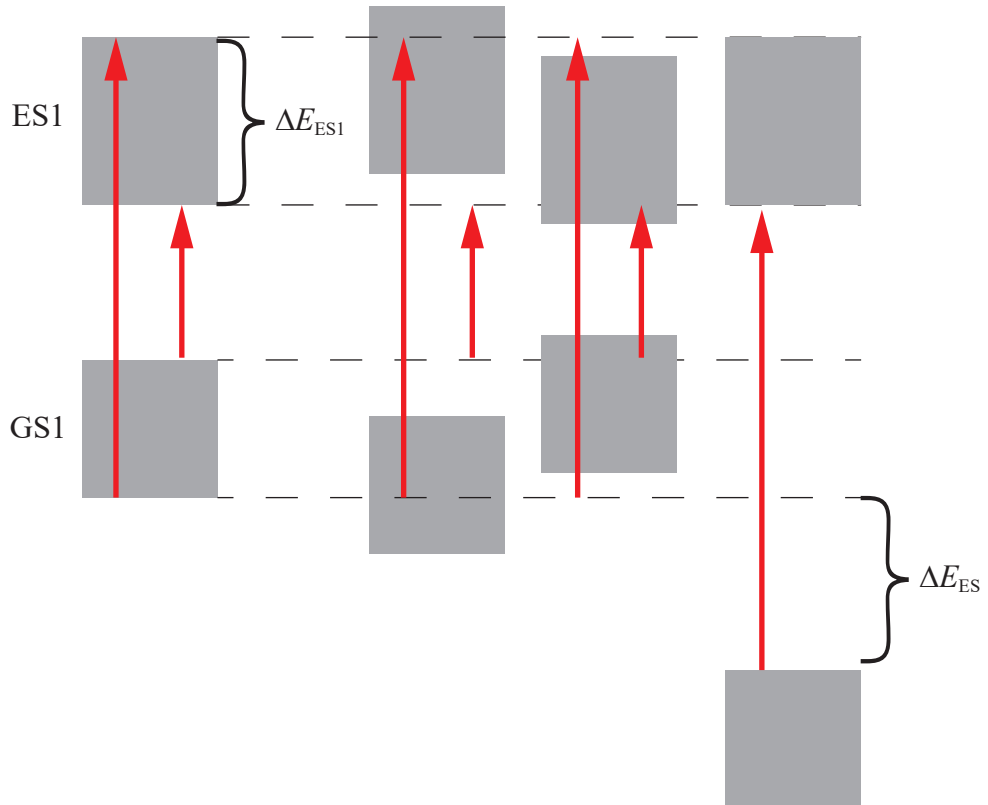
$$\vec{\rho}_{\text{diag}} = M^{-1}\vec{0}.$$

Figure A.1: Schematic showing the effective inhomogeneity Δ_{ES1}. The first three GS1, ES1 manifolds have inhomogeneities $\Delta < \Delta_{\mathrm{ES1}}$, and can be accessed by either the long leg or short leg laser. The last manifold however, has an inhomogeneity $\Delta > \Delta_{\mathrm{ES1}}$, and as such cannot be accessed by any laser (the long leg is shown in the figure). Therefore, Δ_{ES1} acts as an effective inhomogeneity, as the last manifold is not addressed in this driving scheme.

However, there is a problem with the above equation - the only solution is the trivial solution $\rho = \vec{0}$. This is because the populations have not been normalised. The population P_i represents the probability to find the system in state $|\psi_i\rangle$ with $i = 1, 2, \ldots, 32$. As such, the normalisation condition $\sum_i P_i = 1$ is necessary. Then, $\vec{\rho}_{\text{diag}}$ can be modified by adding the total population $P_{\text{tot}} = 1$ to the bottom of the vector to give $\tilde{\rho}_{\text{diag}}$, satisfying the normalisation condition, with M and the zero vector $\vec{0}$ being treated in the same way to give $\tilde{M}$ and $\tilde{0}$. This then gives

$$
\tilde{M}\tilde{\rho}_{\text{diag}} \equiv
\begin{pmatrix}
 & & & \\
 & M & & \\
 & & & \\
1 & \cdots & 1
\end{pmatrix}
\begin{pmatrix}
P_1 \\ P_2 \\ \vdots \\ P_{32} \\ 1
\end{pmatrix}
=
\begin{pmatrix}
0 \\ 0 \\ \vdots \\ 0 \\ 1
\end{pmatrix}
\longrightarrow \tilde{\rho}_{\text{diag}} = \left(\tilde{M}\right)^{-1}\tilde{0}.
$$

which has a non-trivial solution for $\tilde{\rho}_{\text{diag}}$, and hence for $\vec{\rho}_{\text{diag}}$. All that is left to solve for ρ is to determine the Lindbladian matrix M - once M is determined, ρ can be easily solved. To understand how M is constructed, it is best to consider a simple four-level system. This can be seen in Figure A.2. Let the ground states be called $|0\rangle$ and $|1\rangle$, and the excited states $|2\rangle$ and $|3\rangle$. Then, upon applying two lasers that are resonant with the transitions $|0\rangle - |2\rangle$ and $|1\rangle - |3\rangle$, with driving rates Ω_{0-2} and Ω_{1-3} respectively, and allowing for cross relaxation between all states, the rate of change of each state population $\dot{P}_i$ can be modelled as follows

$$
\begin{aligned}
\dot{P}_0 &= -(\Omega_{0-2} + \gamma_{0-1})P_0 + \gamma_{1-0}P_1 + \Gamma_{2-0}P_2 + \Gamma_{3-0}P_3, \\
\dot{P}_1 &= -(\Omega_{1-3} + \gamma_{1-0})P_1 + \gamma_{0-1}P_0 + \Gamma_{2-1}P_2 + \Gamma_{3-1}P_3, \\
\dot{P}_2 &= -(\Gamma_{2-0} + \Gamma_{2-1} + \gamma_{2-3})P_2 + \Omega_{0-2}P_0 + \gamma_{3-2}P_3, \\
\dot{P}_3 &= -(\Gamma_{3-0} + \Gamma_{3-1} + \gamma_{3-2})P_3 + \Omega_{1-3}P_1 + \gamma_{2-3}P_2
\end{aligned}
$$

where Γ_{i-j} is the relaxation rate between excited state i and ground state j, and γ_{m-n} is the relaxation rate between two states in the same ground or excited state manifold. Writing the four equations above in the matrix equation $M\rho$, gives

$$
\begin{pmatrix}
\dot{P}_0 \\ \dot{P}_1 \\ \dot{P}_2 \\ \dot{P}_3
\end{pmatrix}
=
\begin{pmatrix}
-(\Omega_{0-2} + \gamma_{0-1}) & \gamma_{1-0} & \Gamma_{2-0} & \Gamma_{3-0} \\
\gamma_{0-1} & -(\Omega_{1-3} + \gamma_{1-0}) & \Gamma_{2-1} & \Gamma_{3-1} \\
\Omega_{0-2} & 0 & -(\Gamma_{2-0} + \Gamma_{2-1} + \gamma_{2-3}) & \gamma_{3-2} \\
0 & \Omega_{1-3} & \gamma_{2-3} & -(\Gamma_{3-0} + \Gamma_{3-1} + \gamma_{3-2})
\end{pmatrix}
\begin{pmatrix}
P_0 \\ P_1 \\ P_2 \\ P_3
\end{pmatrix}.
$$

The matrix in the above equation is the Lindbladian matrix M for the system. Splitting the Lindbladian matrix into four 2×2 matrices (2 states in each manifold), a general trend can be seen. The diagonal of the upper left matrix gives the total rate of population decrease for state $|i\rangle$ in the ground state manifold. This includes depletion from driving $-\Omega$, and a population decrease via relaxation $-\gamma_g$ to the other ground state. The off-diagonal terms in the upper left matrix are the rates of population increase via ground state relaxation $+\gamma_g$. In the same way, the terms in the upper right matrix are the rates of population increase via relaxation $+\Gamma$ from the excited states into the ground states, and the terms in the lower left matrix gives the rates of population increase in the excited states via driving $+\Omega$ from the ground states to the excited states. The diagonal in the lower right matrix gives the total rates of population decrease for the excited states. This includes relaxation from excited to ground states $-\Gamma$, and relaxation between excited states $-\gamma_e$. Much in the same way as the upper left matrix, the off-diagonal terms in the lower right matrix are the rates of population increase via excited state relaxation $+\gamma_e$. Therefore, the term M_{ij} represents the contribution of population from state j into state i, and each row i is associated with the behaviour of $\dot{P}_i$. The

diagonal terms $M_{ii} < 0$ represent the total contribution of state i to all other states, and as such, each column in the Lindbladian matrix sums to zero. This approach is easily extendable to a 32-state system. Note that for the system studied in this research, the GS1 and ES1 effective-spin relaxation rates are symmetric - that is $\gamma_{i-j} = \gamma_{j-i}$.
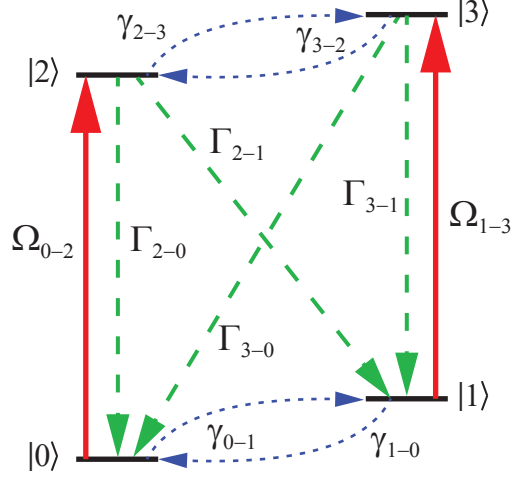

Figure A.2: Four-level system driven by two incident lasers with driving rates Ω_{i-j} between ground state $|i\rangle$ and excited state $|j\rangle$. The spin relaxation within the ground and excited manifolds from state $|i\rangle$ to state $|j\rangle$ is denoted by γ_{i-j}, while optical relaxation from state $|i\rangle$ to state $|j\rangle$ is denoted by Γ_{i-j}.

A.III   Optical Operators: Selection Rules Schematic

Figure A.3 shows the selection rules for driving optical transitions with linearly-polarised light, and $\sigma_{\pm}$ circularly-polarised light. Note that cross transitions are also possible, but these are weaker than direct transitions. For brevity, only two m_I states are shown in each effective-spin manifold.

A.IV   Derivation of Fidelity $F = \sqrt{P}$

Before an initialisation protocol can be developed, a quantitative definition of initialisation must first be given. Ultimately, initialisation means preparing the system into a pure quantum state, and specifically here an eigenstate of GS1. In terms of the 32×32 density matrix ρ, this means going from the mixed state ρ (with nonzero populations along the diagonal) to a pure state σ, where there is only one nonzero population equal to 1. Using the four-level system above as an example, the density matrix ρ of the system at thermal equilibrium is given by (neglecting coherences)

$$\rho = \text{diag}(0.25,\ 0.25,\ 0.25,\ 0.25).$$

If the system must be prepared in the ground eigenstate $|1\rangle$, by applying the appropriate protocol, ρ must be brought to the pure state σ

$$\sigma = \text{diag}(0,\ 1,\ 0,\ 0) = |1\rangle \langle 1|.$$

In reality, it is near impossible to achieve the state σ. However, it is possible to get very close. For example, upon applying some protocol, ρ is brought to

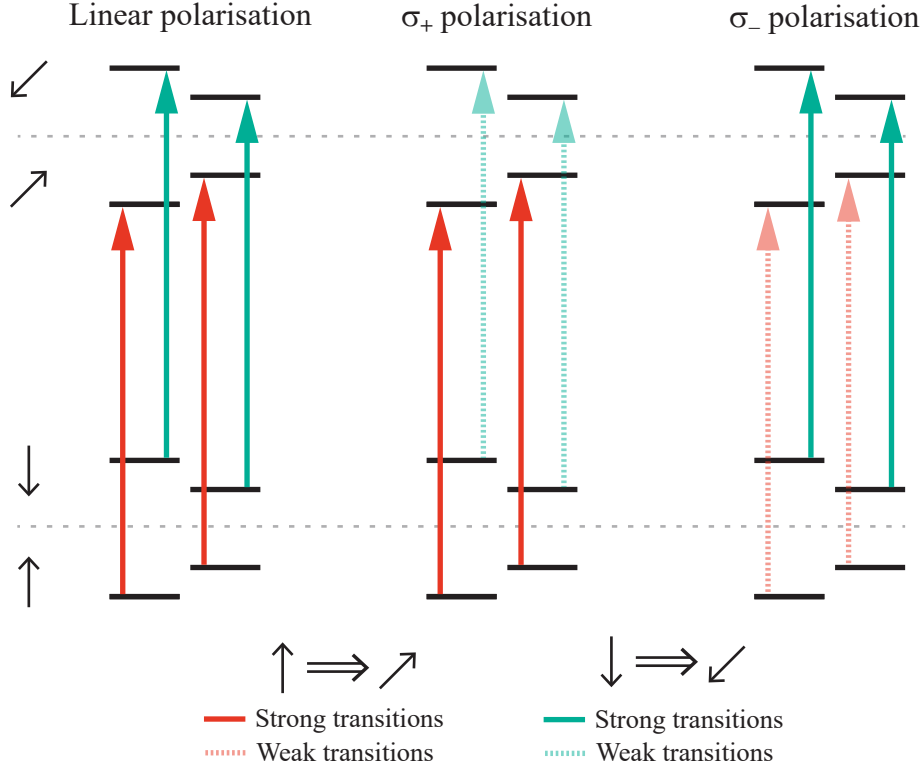$$\rho = \text{diag}(0.0025, 0.9925, 0.0025, 0.0025).$$

Figure A.3: Selection rules for different polarisations of light. Note that cross transitions are also allowed, but are weaker than direct transitions. Cross transitions have been omitted from the schematic for brevity.

The question now is how close is the mixed state ρ to the pure state σ. To answer this, it is useful to introduce the concept of the fidelity $F(\rho, \sigma)$. The fidelity is defined as [82]

$$F(\rho, \sigma) = \text{Tr}\left(\sqrt{\sqrt{\rho}\sigma\sqrt{\rho}}\right)$$

and if ρ and σ commute (which is the case here), this becomes

$$F(\rho, \sigma) = \text{Tr}\left(\sqrt{\rho\sigma}\right).$$

The fidelity is symmetric $F(\rho, \sigma) = F(\sigma, \rho)$ and reduces to the state overlap $F = \langle\psi_\rho|\psi_\sigma\rangle$ when ρ and σ are pure states. In the context of the four-level example, $\sqrt{\rho\sigma} = \text{diag}(0, 0.9962, 0, 0)$. All other terms in $\rho\sigma$ are zero, except the square-rooted population of the quantum state to be prepared. Then, the fidelity becomes $F = \text{Tr}\left(\text{diag}(0, 0.9962, 0, 0)\right) = 0.9962$. This is equal to $\sqrt{0.9925}$, which was the population of state $|1\rangle$ in the initialised ρ. Generalising this to a 32×32 system

$$\rho = \text{diag}(P_1, P_2, \ldots, P_{32}),$$

$$\sigma = \text{diag}(0, 0, \ldots, P_i = 1, \ldots, 0).$$

with $i \leq 16$ as the system is initialised into one of the GS1 eigenstates. Then

$$\rho\sigma = \delta_{ij}P_j.$$

Thus, when working with density matrices without coherences, and comparing them to pure eigenstates as is done here, the fidelity of an initialised state ρ and eigenstate g_i is simply given by

$$F(\rho, g_i) = \sqrt{P_{g_i}} \tag{A.5}$$

where P_{g_i} is the population of eigenstate g_i in ρ.

B   Appendices to Section 3: Methods & Approach

B.I   Implementation of Lindbladian Model

Contact the author (Adrian P.J. Sidhu) for more information on the computational implementation of the Lindbladian model.

Mathematical Description of Operators

In total there were seven operators used in the Lindbladian model. Four of these were the four effective-spin processes - electron spin flip (ESF), nuclear spin flip (NSF), flip-flop (FF), and the $\hat{z}$-axis flip-flop (FFz). The ESF entails a change in the effective spin $\Delta m_{\tilde{S}} = 1$, the NSF a change in the nuclear spin Δm_I, and the FF and FFz a change in both the effective electron spin and nuclear spin, $\Delta m_{\tilde{S}} = 1$ and Δm_I. Then there were the optical relaxation and linearly-polarised driving operator $\mathcal{O}_{\text{opt}}$, and finally the circularly-polarised driving operators $\mathcal{O}_{\pm}$. The four effective-spin operators used in the model are

$$\mathcal{O}_{\text{ESF}} = \left(\tilde{S}_+ + \tilde{S}_-\right) \cdot \mathcal{I}_I, \tag{B.1}$$

$$\mathcal{O}_{\text{NSF}} = (I_+ + I_-) \cdot \mathcal{I}_{\tilde{S}}, \tag{B.2}$$

$$\mathcal{O}_{\text{FF}} = I_+\tilde{S}_+ + I_-\tilde{S}_-, \tag{B.3}$$

$$\mathcal{O}_{\text{FFz}} = I_z\tilde{S}_z. \tag{B.4}$$

where $\tilde{S}_{\pm} = \tilde{S}_x \pm i\tilde{S}_y$ and $I_{\pm} = I_x \pm iI_y$ are raising and lowering operators for the effective-spin and nuclear spin, respectively. The spin operators used in the model are given by

$$\tilde{S}_z = \frac{1}{2}\begin{pmatrix} J_8 & 0_{8,\,8} \\ 0_{8,\,8} & -J_8 \end{pmatrix},$$

$$\tilde{S}_+ = \begin{pmatrix} 0_{8,\,8} & J_8 \\ 0_{8,\,8} & 0_{8,\,8} \end{pmatrix},$$

$$\tilde{S}_- = \begin{pmatrix} 0_{8,\,8} & 0_{8,\,8} \\ J_8 & 0_{8,\,8} \end{pmatrix},$$

$$I_z = \begin{pmatrix} i_z & i_z \\ i_z & i_z \end{pmatrix}$$

$$\text{with } i_z = \text{diag}(\boldsymbol{m_I}) = \text{diag}(7/2,\ 5/2,\ 3/2,\ 1/2,\ -1/2,\ -3/2,\ -5/2,\ -7/2),$$

$$I_{\pm} = \begin{pmatrix} i_{\pm} & i_{\pm} \\ i_{\pm} & i_{\pm} \end{pmatrix}$$

$$\text{with } i_{\pm} = \text{diag}_{\pm}\left(\sqrt{j(j+1) - \boldsymbol{m_I}(\boldsymbol{m_I} \pm 1)}\right)$$

$\mathbb{I}_n$ is an $n \times n$ identity matrix, J_n is an $n \times n$ matrix of ones, and $0_{n,\,n}$ is an $n \times n$ matrix of zeros. The $\text{diag}_{\pm}(\boldsymbol{x})$ operator places the elements $\boldsymbol{x}$ just above (+) or just below (−) the main diagonal. The matrices $\mathcal{I}_I$ and $\mathcal{I}_{\tilde{S}}$ are to ensure that there are no flip-flops in $\mathcal{O}_{\text{ESF}}$ and $\mathcal{O}_{\text{NSF}}$, respectively. Since the eigenstates are composed of a linear combination of effective-spin states, the raising and lowering effective-spin operators $\tilde{S}_{\pm}$ weakly allow changes in the nuclear spin (projection number) m_I, which results in $\tilde{S}_+ + \tilde{S}_-$ being an effective (weak) flip-flop. The same applies to $I_{\pm}$ with changes in $m_{\tilde{S}}$. To ensure $\tilde{S}_+ + \tilde{S}_-$ remains a pure electron spin flip it is multiplied with the matrix $\mathcal{I}_I$, which is defined in the model by

$$\mathcal{I}_I = \begin{pmatrix} \mathbb{I}_8 & \mathbb{I}_8 \\ \mathbb{I}_8 & \mathbb{I}_8 \end{pmatrix}.$$

The matrix $\mathcal{I}_{\tilde{S}}$ works in a similar way to restrict $\mathcal{O}_{\text{NSF}}$ to pure nuclear spin flips, and is given in the model by

$$\mathcal{I}_{\tilde{S}} = \begin{pmatrix} J_8 & 0_{8,\,8} \\ 0_{8,\,8} & J_8 \end{pmatrix}$$

The optical driving and relaxation operators are given in Section 2.3.

Values Used for Model Parameters

The Hamiltonian used for the system is given in Section 2.1.2, but will be given here again for clarity. Denoting the hyperfine contribution as HF, the electron ($\tilde{S}$) Zeeman contribution as Z:el, and the nuclear (I) Zeeman contribution as Z:nuc, the Hamiltonian for effective spin states transforming as Γ_4 and $\Gamma_{5,\,6}$ is given by

$$H_{\Gamma_x} = H^{eff}_{\text{HF},\,\Gamma_x} + H^{eff}_{\text{Z:el},\,\Gamma_x} + H^{eff}_{\text{Z:nuc:},\,\Gamma_x}, \tag{B.5}$$

where for $\Gamma_x = \Gamma_4$

$$\begin{aligned}
H^{eff}_{\text{HF},\,\Gamma_4} &= a_{\parallel,\,\Gamma_4}\tilde{S}_z I_z + a_{\perp,\,\Gamma_4}(\tilde{S}_+ I_+ + \tilde{S}_- I_-) + Q_{zz}I_z^2 \\
H^{eff}_{\text{Z:el},\,\Gamma_4} &= -\mu_B\big(g_{\parallel,\,\Gamma_4}B_z\tilde{S}_z + g_{\perp,\,\Gamma_4}(B_x\tilde{S}_x + B_y\tilde{S}_y)\big) \\
H^{eff}_{\text{Z:nuc:},\,\Gamma_4} &= -\mu_N g_n(B_z I_z + B_x I_x + B_y I_y)
\end{aligned} \tag{B.6}$$

and for $\Gamma_x = \Gamma_{5,\,6}$

$$\begin{aligned}
H^{eff}_{\text{HF},\,\Gamma_{5,\,6}} &= (a_{\parallel,\,\Gamma_{5,\,6}}\tilde{S}_z + a_{\perp,\,\Gamma_{5,\,6}}\tilde{S}_x)I_z + Q_{zz}I_z^2 \\
H^{eff}_{\text{Z:el},\,\Gamma_{5,\,6}} &= -\mu_B g_{\parallel,\,\Gamma_{5,\,6}}B_z\tilde{S}_z \\
H^{eff}_{\text{Z:nuc:},\,\Gamma_{5,\,6}} &= -\mu_N g_n(B_z I_z + B_x I_x + B_y I_y).
\end{aligned} \tag{B.7}$$

$\tilde{S}_{x,\,y,\,z}$, and $I_{x,\,y,\,z}$ are the effective-spin and nuclear spin operators, respectively, and $(B_x,\ B_y,\ B_z)$ is the applied static magnetic field vector. The $\hat{z}$ axis is taken to be parallel with the crystal c axis. The parameters used in the simulated model were taken from Wolfowicz et al. [61] and are given by

$$\begin{aligned}
a_{\parallel,\,\Gamma_4} &= 232 \text{ MHz} \\
a_{\perp,\,\Gamma_4} &= 162 \text{ MHz} \\
g_{\parallel,\,\Gamma_4} &= 1.664 \\
g_{\perp,\,\Gamma_4} &= 0 \\
a_{\parallel,\,\Gamma_{5,\,6}} &= 215 \text{ MHz} \\
a_{\perp,\,\Gamma_{5,\,6}} &= 70.5 \text{ MHz} \\
g_{\parallel,\,\Gamma_{5,\,6}} &= 2.1 \\
g_{\perp,\,\Gamma_{5,\,6}} &= 0.
\end{aligned}$$

Determining the Rate Coefficients $\mathcal{R}$ and Their Limits

The rate coefficients $\mathcal{R}$ are used to quantify environmental interactions in the Lindbladian effective-spin relaxation rates. To determine the rate coefficients, experimental two-laser spectroscopy data at 15 static magnetic field strengths (0 mT, 2 mT, 4 mT, 6 mT, 8 mT, 13 mT, 18 mT, 23 mT, 28 mT, 33 mT, 38 mT, 43 mT, 48 mT, 75 mT, 300 mT) was used. Since a two-laser spectroscopy signal directly reflects how much population is in the excited state (see Figure 3.1b), this data was

compared to the sum of the ES1 eigenstate populations in the simulation. The rate coefficients were then changed to fit this experimental data as best as possible. This was done in a few different ways - first by eye, then by matching the simulated peaks (dips) with experimental peaks (dips), and finally by minimising the RMSE. In the end, a set of rate coefficients were determined globally for the magnetic fields. These are referred to as the standard rate coefficients in the main text, and are given by

$$\mathcal{R}_{\mathrm{ESF}}^{g} = 0.01 \text{ MHz},$$
$$\mathcal{R}_{\mathrm{NSF}}^{g} = 0.001 \text{ MHz},$$
$$\mathcal{R}_{\mathrm{FF}}^{g} = 0.5 \text{ MHz},$$
$$\mathcal{R}_{\mathrm{FFz}}^{g} = 5 \text{ MHz}$$
$$\mathcal{R}_{\mathrm{ESF}}^{e} = 30 \text{ MHz},$$
$$\mathcal{R}_{\mathrm{NSF}}^{e} = 0.001 \text{ MHz},$$
$$\mathcal{R}_{\mathrm{FF}}^{e} = 0.1 \text{ MHz},$$
$$\mathcal{R}_{\mathrm{FFz}}^{e} = 30 \text{ MHz}.$$

Note that a high rate coefficient does not necessarily mean a high relaxation rate, as the relaxation rate is also dependent on the associated transition probability. For example, while the GS1 flip-flop has a rate coefficient of 0.5 MHz, it is the dominant relaxation process of GS1. Errors for these rate coefficients were determined by finding the value for which the RMSE changed by 10% of the original RMSE (calculated with the standard rate coefficients), at each magnetic field studied. The rate coefficients with the smallest errors relative to the respective standard rate coefficient were the coefficients that the simulation response was most sensitive to. As seen in Section 4.1, at 40 mT this was the GS1 NSF (error of $\Delta\mathcal{R}_{\mathrm{NSF}}^{g} = 0.007$, with $\Delta\mathcal{R}_{\mathrm{NSF}}^{g}/\mathcal{R}_{\mathrm{NSF}}^{g} = 7$) followed by the GS1 ESF (error of $\Delta\mathcal{R}_{\mathrm{ESF}}^{g} = 0.13$, with $\Delta\mathcal{R}_{\mathrm{ESF}}^{g}/\mathcal{R}_{\mathrm{ESF}}^{g} = 13$).

Summing Over Inhomogeneities

The inhomogeneities Δ_{inh} are implemented in the model through the Lorentzian PDF. For an inhomogeneous ensemble, Eq. (2.15) becomes

$$f(\omega, \ \Delta_{\mathrm{inh}}; \ \omega_0, \ \Gamma_{\mathrm{opt}}) = \frac{1}{\pi} \frac{\Gamma_{\mathrm{opt}}}{\left((\omega_0 + \Delta_{\mathrm{inh}}) - \omega\right)^2 + \Gamma_{\mathrm{opt}}^2}. \tag{B.8}$$

For the simulated results in the main text, an inhomogeneous broadening of 2 GHz was used (see Appendix A.I), with inhomogeneities ranging from -1 GHz to 1 GHz in 2 MHz steps (1001 values in total). The inhomogeneity distribution (i.e. the spectral density) was uniform. The Lindbladian matrix was calculated and the populations solved for each inhomogeneity Δ_{inh} (with $\Delta_{\mathrm{inh}} = -1$ GHz, -998 MHz, ..., 998 MHz, 1 GHz). To then simulate the response of an inhomogeneous ensemble, the populations were summed over the inhomogeneities. Explicitly, per magnetic field strength, the 32 populations were calculated for each laser detuning and each inhomogeneity. As such, the population arrays (per magnetic field strength) were of the size $32 \times N_{\delta_S} \times N_{\Delta_{\mathrm{inh}}}$, where N_{δ_S} is the number of laser detunings and $N_{\Delta_{\mathrm{inh}}} = 1001$ is the number of inhomogeneities. The populations were then summed over the dimension of the inhomogeneities, resulting in a population array size of $32 \times N_{\delta_S}$. The only terms in the Lindbladian which account for the inhomogeneities are the driving terms, but the summation also includes the relaxation terms. Summing over both the driving and relaxation terms of the Lindbladian has the effect of reducing the efficiency of initialisation, as in a physical inhomogeneous ensemble. However, the relaxation terms of the Lindbladian are summed $N_{\Delta_{\mathrm{inh}}}$ times with equal strengths, since these terms are inhomogeneity independent (they do not contain

the Lorentzian PDF, Eq. (B.8)). For example, if one of the original (single-defect) relaxation terms of the Lindbladian is γ, the corresponding term in the inhomogeneous Lindbladian is $N_{\Delta_{\text{inh}}} \cdot \gamma$.

To adequately represent the physical system, the distribution (i.e. the spectral density) of inhomogeneities needs to be approximately continuous, as is seen in experiment (see Figure B.2). To ensure approximate continuity in the simulation, a spacing of 2 MHz was used. This was more computationally efficient than using 1 MHz. Using a spacing of 2 MHz means that in general, for some inhomogeneous broadening Δ, the number of inhomogeneities $N_{\Delta_{\text{inh}}}$ will be given by $N_{\Delta_{\text{inh}}} = \Delta/2\text{ MHz} + 1$ (the +1 is to account for $\Delta_{\text{inh}} = 0$). For example, if $\Delta = 2$ GHz= 2000 MHz, the number of inhomogeneities is given by $N_{\Delta_{\text{inh}}} = 2000/2 + 1 = 1001$. This linear dependence between Δ and $N_{\Delta_{\text{inh}}}$ arising from the necessity of having a continuous inhomogeneity distribution, paired with the summing of the relaxation terms of the Lindbladian ($N_{\Delta_{\text{inh}}} \cdot \gamma$), results in the absolute percentage value of ΔP being highly dependent on the broadening Δ used. Taking the ~ 525 MHz peak in Figure 4.1 as an example, doubling the inhomogeneous broadening from $\Delta = 2$ GHz to $\Delta = 4$ GHz (-2 GHz to 2 GHz) results in the peak going from $\Delta P(g_6, g_8) = 0.48\%$ to $\Delta P(g_6, g_8) = 0.23\%$, which is just less than half of the initial value (Figure B.1). Note that since the effective inhomogeneity is only ~ 2 GHz (Appendix A.1), the behaviour of ΔP does not change. This can be seen in the right panel of Figure B.1. This means that the absolute percentage value of ΔP is not a physically significant value. In other words, a population contrast of $\Delta P(g_i, g_j) = 1\%$ in the simulated inhomogeneous ensemble does not mean that in the physical ensemble there is an actual 1% difference in population between the states g_i and g_j. Despite this, the relative differences in ΔP for a constant inhomogeneous broadening, including differences between different parameters (magnetic field, laser detunings, qubit candidate), are still significant. For example, if the ΔP between states g_i and g_j at a magnetic field strength of B_0 and detuning $\Delta\delta_0$ is higher than the ΔP between states g_k and g_l at a magnetic field strength of B_1 and detuning $\Delta\delta_1$, it can be experimentally measured (the peak at ~ 525 MHz is evidence of this). This means that the simulated inhomogeneous ensemble can still be used to determine good points of initialisation (for a constant inhomogeneous broadening). Note that this does not apply in the single-defect case, as there are no inhomogeneities and as such this summation problem does not arise.

B.II   Computational Limitations

While it was necessary to use single-defect protocols to prepare for the experimental verification of an inhomogeneous ensemble, as it allows for an indirect verification of the single-defect case, there was a significant caveat; the two-laser detunings were greatly restricted, specifically between 100 MHz (limit of the electro-optic modulator [EOM]) and 600 MHz. This upper limit was by no means experimental, as the EOM could detune up to several GHZ. Instead, it was due to the memory limits of the simulation. Preparing an array of 32 states for each of the two detunings, and for each magnetic field, pushed the limits of available RAM in MATLAB (the simulation was built in MATLAB). This was not a problem for the inhomogeneous case, as the inhomogeneities (which are analogous to the second detuned laser here) were summed over, and hence only saved as temporary variables. The most efficient way found that would still allow for reasonable analysis times was to separate the magnetic fields into ten 1 mT steps, from $0 - 50$ mT. Wanting to maintain a detuning of ± 1200 MHz for one of the lasers for use in the experimental verification of single-defect initialisation protocols, this meant restricting the other laser to ± 600 MHz for memory purposes. This resulted in each population array being of the size $32 \times 2401 \times 1201 \times 10 = 9.23 \cdot 10^8$, which on average corresponded to a MATLAB structure of 7 GB - any larger exceeded the available RAM. For the three polarisations, this was over 100 GB of data. Since the experiment was done with an inhomogeneous ensemble, any theoretical point of interest had the detunings (δ_1, δ_2) of its two beams
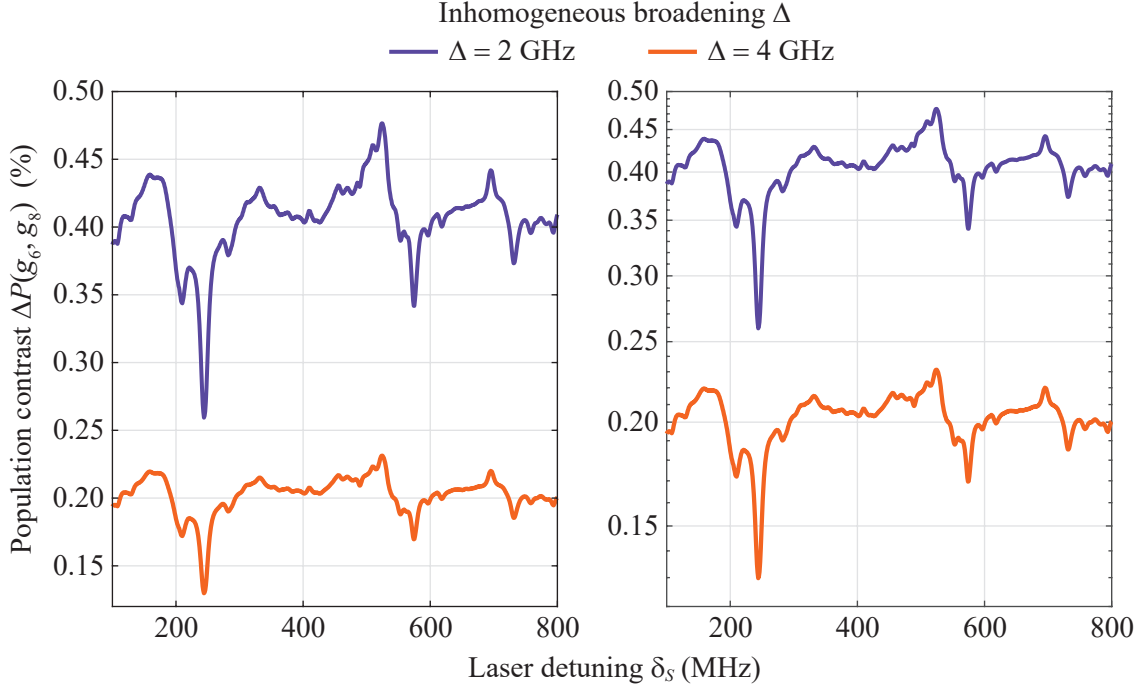
Figure B.1: Simulated population contrast $\Delta P(g_6,\ g_8)$ at 40 mT with two linearly-polarised lasers (and increased GS1 NSF, ESF rate coefficients). The purple plots show ΔP with an inhomogeneous broadening of $\Delta = 2$ GHz (same plot as in Figure 4.1d), while the orange plots show ΔP with an inhomogeneous broadening of $\Delta = 4$ GHz. The left panel has a linearly-scaled y axis, while the right panel has a logarithmically-scaled y axis. The plots in the two panels are the same. It can be seen that while the increased broadening causes ΔP to decrease and the plot to flatten (left panel), the behaviour of ΔP remains the same (right panel). This shows that for a simulated inhomogeneous ensemble, the absolute percentage value of ΔP does not hold physical significance. However, the relative values of ΔP are still important.

subtracted from each other (see Section 2.3 for more information on single-defect and inhomogeneous detuning schemes) to attain its inhomogeneous detuning $\Delta\delta$. This is where a problem arose - for $\delta_1 \geq 600$ MHz, the subtraction $\Delta\delta = \delta_1 - \delta_2$ was not accurate. This was due to the fact that above an absolute value of 600 MHz, one of the lasers remained at ±600 MHz, its maximum absolute value. Thus two-laser detunings $\Delta\delta$ above 600 MHz were in fact the detunings from the ±1200 MHz beam subtracted by a constant ±600 MHz, rather than the actual difference between the two laser frequencies. In hindsight, using a detuning of ±900 MHz for both beams would have still allowed for a thorough single-defect analysis for experimental verification while also increasing the upper limit on the two-laser detuning. A detuning of ±900 MHz was used for the theoretical single-defect protocols seen in Section 5 for these reasons.

B.III   Verification of GS1−ES1 and $g_6 - g_8$ Transition Energy

Resonant Excitation Spectroscopy: GS1−ES1

A resonant excitation spectroscopy measurement was done to determine the GS1−ES1 transition energy experimentally. This can be seen in Figure B.2. The resonant transition energy is around 1278.81 nm (middle of the dip in Figure B.2). To ensure that there was still a distinct transmission signal (transmission is minimized at 1278.81 nm) while still addressing the GS1−ES1 transition, a carrier frequency of 1278.85 nm (and later 1278.86 nm, to increase the signal) was chosen.
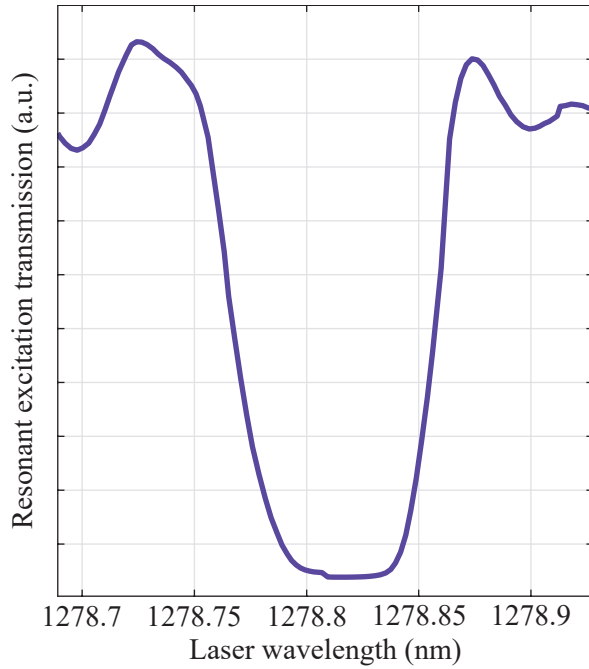
Figure B.2: Resonant excitation spectroscopy measurement done to determine the GS1−ES1 transition energy.

Optically Detected Magnetic Resonance (ODMR): $g_6 - g_8$

The simulation was used to predict the transition energy of the qubit candidate $g_6 - g_8$. An optically detected magnetic resonance (ODMR) measurement was subsequently done to determine what the transition energy was experimentally, using the simulated prediction as a guide. The results can be seen in Figure B.3. The microwaves in the subsequent OD2LSR measurement were then set to 358.7 MHz, based on the experimental ODMR measurement seen in Figure B.3a.
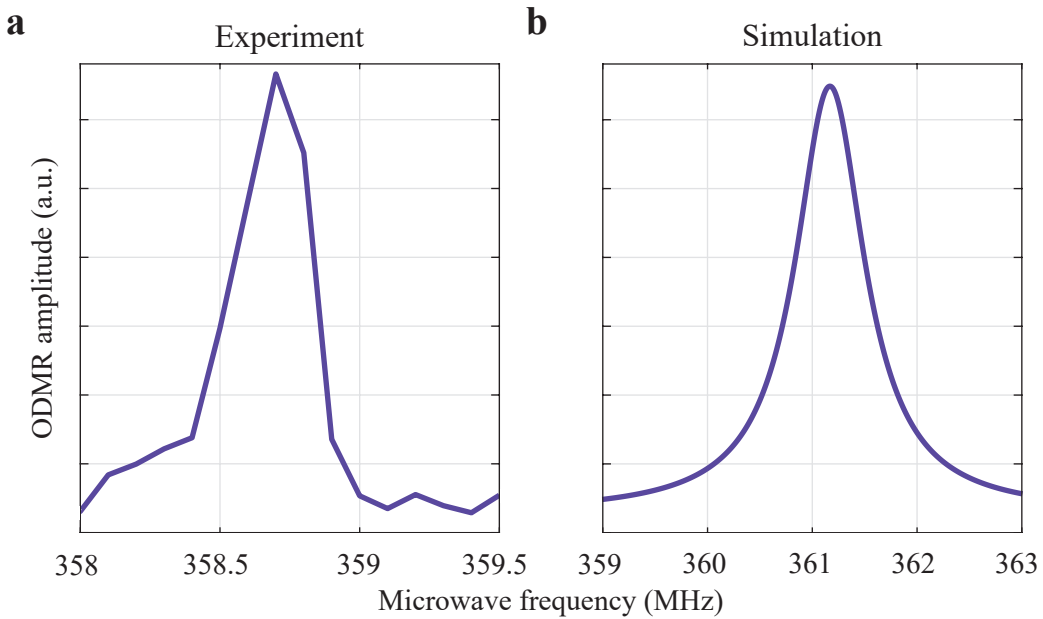

Figure B.3: **a** Experimental ODMR measurement to determine the transition energy of $g_6 - g_8$. **b** Simulated ODMR measurement to provide a prediction of the $g_6 - g_8$ transition energy for experiment.

C Appendices to Section 4: Experimental Results

C.I Transition Analysis and Optical Readout Problem

Figure 4.1 shows an OD2LSR measurement taken at 40 mT, along with simulated population contrasts $\Delta P(g_6, \ g_8)$. There are three main initialisation features predicted by the simulation - the series of peaks and dips from $200 - 300$ MHz, the peak at ~ 524 MHz, and the experimental dip and peak at ~ 700 MHz and ~ 732 MHz respectively. The simulation predicts a peak followed by a dip instead. The reason for this is discussed further on. Some other features seen in the simulation, especially the dip at 575 MHz, are not present in the experimental data. This is most likely due to the detection technique. As explained in Section 3.1, and Figure 3.1, the OD2LSR measurement technique uses one of the initialisation lasers as an optical readout. Thus, to be able to detect an initialisation feature (i.e. a population contrast between g_6 and g_8), the detected scan laser must be resonant with an optical transition involving g_6 (or g_8, but this would deplete g_8, resulting in worse initialisation). Seeing as g_8 is on average 0.4% higher in population than g_6, application of a resonant microwave field would drive this population between the states (see Figure 3.1b). Therefore, the scan laser is probing g_6 for most of the initialisation features seen.

The simulation does not require optical readout. Instead, the full system dynamics are simply calculated. This results in initialisation features that might be present in the physical system but that cannot be experimentally probed. For example, within the simulation, a certain two-laser scheme might result in g_8 being depleted. This would consequentially result in a dip in the $g_6 - g_8$ population contrast, as the g_8 population is always greater at 40 mT. However, if g_6 is not simultaneously probed with one of the two lasers via a strong optical resonance, this will not be detected in experiment. This is exactly what happens at the 575 MHz dip, where there are two optical transitions $g_8 - e_7$ and $g_8 - e_9$, forming a V-scheme (two-laser detuning of 574.4 MHz) which depletes g_8. There is also a V-scheme involving g_6 at 574.4 MHz, but its overlaps are an order of magnitude lower than the g_8 V-scheme, so P_{g_6} is not as affected as P_{g_8}. The depletion of g_8 leads to a ~ 0.05 percentage point decrease in the simulated $g_6 - g_8$. This is on the same order of the experimentally-detected peak at 524 MHz. In experiment, a resonant microwave pulse drives population between g_6 and g_8, resulting in the g_8 depletion being reflected in g_6. The g_6 V-scheme has a limiting optical driving transition probability (i.e. the optical transition in the two-laser driving scheme with the smallest transition probability) of $|\langle O_{\mathrm{opt}}\rangle|^2 \approx 10^{-6}$ and the g_8 V-scheme has a limiting optical transition probability of $|\langle O_{\mathrm{opt}}\rangle|^2 \approx 10^{-5}$. Compare this to the $g_7 - e_{7, 9}$ and $g_9 - e_{7, 9}$ V-schemes which also occur at a detuning of 574.4 MHz, with limiting optical transition probabilities of around $|\langle O_{\mathrm{opt}}\rangle|^2 \approx 0.25$. It is clear to see that while the simulation would detect the g_8 depletion, in experiment the optical readout of both g_6 and g_8 is heavily suppressed by absorption in the g_7 and g_9 V-schemes. The 524 MHz peak seen in experiment has an optical readout on g_6 (π-scheme with 524.8 MHz detuning), with a limiting optical transition probability of $|\langle O_{\mathrm{opt}}\rangle|^2 \approx 10^{-3}$, more than 1000 (100) times that of the limiting transition probability of the g_6 (g_8) scheme at 574.4 MHz. In the single-defect case, it would be possible to acquire an optical readout of the 575 MHz dip, as the individual laser frequencies are different for the different V-schemes. However, seeing that this would result in a decreased contrast, it is not optimal for initialisation.

For both the single-defect and inhomogeneous case, the lack of an optically accessible state could be solved by the addition of a third, optical-readout laser, though this can be impractical. Thus, a simulation-based solution is favourable. As mentioned previously, the simulated data gives the entire system picture, whereas the experiment only shows features which can be optically read. This disconnect between experiment and simulation could be improved by integrating an optical readout feature in the simulation, whereby initialised features that do not have optical transitions corresponding to

one of the initialised states are not included, or at the least, heavily suppressed. For example, adding a scaling factor to optical transitions resonant with g_6 would highlight initialisation features that are both optically accessible for readout and correctly represent the dynamics. Thankfully, despite this optical readout limitation not being imposed prior to experiment, most of the relevant initialisation features can still be seen.

The reason why the simulation predicts a peak at 700 MHz, as opposed to the dip seen in the experiment, and a dip at 730 MHz as opposed to a peak goes back to the above mentioned optical readout problem. The population contrast was calculated by $|P_{g_8} - P_{g_6}|$, and seeing that for all detunings at 40 mT $P_{g_8} > P_{g_6}$ this is equal to $P_{g_8} - P_{g_6}$. Analysis has shown that for the 524 MHz peak, and the $100 - 200$ MHz features, it is the changes in P_{g_8} that are being detected via an optical readout on g_6 (after population driving with microwaves). Upon flipping the contrast to $P_{g_6} - P_{g_8}$, the simulation shows the dip and peak like experiment. Thus, it is the changes in P_{g_6} that are being probed here (via optical readout on g_8) and hence the simulated population contrast calculated as $P_{g_8} - P_{g_6}$ shows the opposite. While it would be possible to add an optical readout scaling factor that is also sensitive to sign changes, and hence changes in both P_{g_8} and P_{g_6}, these features can still be seen regardless of their sign. When developing protocols for OD2LSR-like measurements (i.e. continuous-wave) it is thus better to simply check whether promising initialisation features have an optical readout state, and whether it is reading out the correct state.

The peak at 524 MHz is the result of several initialising driving schemes. There are two prominent π-schemes involving a $g_9 - e_8$ transition. The $e_8 - e_9$ relaxation rate is very strong here, $\gamma_{e_8-e_9} = \mathcal{R}_e|\langle O_e \rangle|^2 \approx 0.8$, meaning that both states relax into each other quickly. This is an electron spin flip mediated relaxation, as explained in Section 5.1. However, the optical relaxation overlap between e_8 and g_8 is $\sim 25\%$ greater than the $e_9 - g_9$ relaxation. This stronger optical relaxation causes e_8 to have a lower population than e_9 before steady state, and so the population imbalance between e_8 and e_9 causes a faster depletion in e_9. Via the optical relaxation of e_8, this ultimately results in a larger P_{g_8}. There are two similar schemes involving the g_{10} to e_8 transition which work by the same mechanism. The π-scheme used for optical readout on g_6 is composed of the transitions g_6-e_7 with $|\langle O_{\text{optical}} \rangle|^2 \approx 10^{-3}$ and $g_9 - e_8$ with $|\langle O_{\text{optical}} \rangle|^2 \approx 10^{-2}$. This scheme populates g_8 via e_8 optical relaxation and also depletes g_6, increasing the overall $g_6 - g_8$ contrast, while providing optical readout on g_6.

C.II Relative Amplitudes and the Rate Coefficient Problem

The simulation is able to accurately and precisely determine the detunings at which initialisation features occur, but struggles to correctly predict the relative amplitudes of the different initialisation features. A clear example of this can be seen in the peaks and dips in the $200 - 300$ MHz range. Three dips can be seen in both experiment and simulation, with the difference being that the dip at ~ 245 MHz has a much larger amplitude in simulation as compared to experiment. To understand this, the Lindbladian model must be analysed. The states $\{|\psi\rangle\}$ are eigenstates of H with eigenvalues given by the eigenstate energies, as discussed in Section 2.1.2. The population amplitudes are determined by the Lindbladian terms, $\mathcal{R} \cdot |\langle \psi_i|\mathcal{O}|\psi_j \rangle|^2$ for the relaxation terms and $f(\omega; \omega_0, \Gamma_{\text{opt}}) \cdot \mathcal{R} \cdot |\langle \psi_j|\mathcal{O}|\psi_i \rangle|^2$ for the driving terms. The rate coefficients $\mathcal{R}$ are determined empirically. The simulation calculating accurate transition energies at the hyperfine level provides evidence for a reliable (perturbed) Hamiltonian. Furthermore, seeing that the optical linewidth has been determined to high precision [60, 61], either the empirically determined rates, or the operators themselves, are inaccurate in their predictions.

The operators used in the Lindblad model were derived in a purely phenomenological framework.

Thus, it is unlikely that the operators are inaccurate, as they are basic quantum mechanical operations, such as ladder operators. Furthermore, seeing as the transition probabilities $|\langle\psi_j|\mathcal{O}|\psi_i\rangle|^2$ are calculated with the Hamiltonian basis states $\{|\psi\rangle\}$, and the Hamiltonian has been verified to be accurate via ODMR measurements, these probabilities represent the spin dynamics at the defect level well. That being said, in both the inhomogeneous ensemble and the single defect case the vanadium exists in and interacts with the surrounding environment. Therefore some of the processes described at the theoretical level are suppressed and others enhanced by these environmental interactions. Admittedly, a big assumption of the model is that the rate coefficients $\mathcal{R}$ are electromagnetic-field independent. One set of standard coefficients were determined using 15 magnetic fields, 14 in the range of $0-75$ mT and one at 300 mT. Additionally, no distinction was made between using one or two lasers or having microwaves incident on the sample. The power dependencies were not characterised either. While the coefficients are applied globally to one process, for example the rate coefficient for a $\Delta m_I = 1$ and $\Delta m_I = 2$ nuclear spin flip is the same, this still works to favour some transitions over others depending on the preferred process of a transition. The ability to strengthen or weaken specific processes directly influences the spin state dynamics, and hence the state populations.

The only way to properly remedy this is to determine field- and sample-dependent coefficients. This can be done in a similar manner to before, using experimental two-laser data and optimising the rates for the specific experimental parameters used. In future research, it would be suggested to use a simple but automated machine learning regression technique, in tandem with a high-performance computing cluster, to determine the rates more efficiently, and for a larger number of magnetic fields.

The rate coefficients affecting the relative amplitudes has consequences on the initialisation approach. The approach used to find promising points of initialisation for experimental verification involved maximising the population contrast (or USRN for experiment). If the accuracy of the population contrast amplitudes is questionable, this means that maximising it without the appropriate rate coefficients is not completely reliable. Furthermore, since the population contrast depends on the rates in a non-linear way, the error arising from these coefficients is not systematic. Fortunately, the errors in the relative amplitudes between experiment and simulation were not very large (for 40 mT, the largest error was around 20% for the dip at ~ 250 MHz) and the simulation was still able to provide good points for initialisation. This might be due to the fact that both 38 mT and 43 mT were used in the rate coefficient determination, and these fields have very similar dynamics to 40 mT.

Summary

One of the biggest assumptions made in the model used in this research is that the rates stay independent of all experimental parameters except temperature (rate coefficients were determined using experimental data taken at 2 K). Analysis between simulated and experimental results has shown that the rates are dependent on quite a few experimental parameters (number of incident oscillating fields, strength of static magnetic field, laser polarisation). Of course, finding a different set of rate coefficients for each magnetic field and polarisation, and for both the one- and two-laser cases would be unrealistic. A possible approach would be to determine one set of rates for ranges of, for example, 10 magnetic fields. Then for one range, determine the difference between the one- and two-laser cases. In this way there would be two sets of rate coefficients for a range of 10 magnetic fields. Furthermore, in the electronic Zeeman regime, the rates can be kept more or less constant, as the dynamics of the system do not change much here.

C.III   Rejected Hypotheses for the One-/Two-Laser Signal Difference

It was first thought that the addition of a second laser could result in g_8 being depleted faster, consequentially reducing the population contrast. To verify this, a series of V-, $\lambda-$, $\pi-$, and X-schemes were analysed at 400 MHz, where there were no significant initialisation features in both the experiment and simulation. In the one-laser case it was concluded that the high contrast between g_6 and g_8 was due to the strong relaxation pathways between g_8 and all other ground states, as over the entire detuning range g_8 has a $\sim 0.45\%$ larger population than g_6. This effect is also present in the two-laser case however, and does not explain the signal difference. In the end, the analysis proved unfruitful; there were no one-laser transitions or two-laser schemes which could sufficiently explain such a difference between the two signals. Another possible explanation was that the optical linewidth used in the simulation, 10 MHz corresponding to an optical lifetime of 100 ns, was too narrow. Increasing this linewidth (and in turn decreasing the excited state lifetime) to 20 MHz (50 ns) resulted in the two-laser contrast decreasing, as expected. Despite this, the two-laser contrast was still higher than the one-laser contrast, and hence was still unable to explain the signal difference. Increasing the optical linewidth above 20 MHz is not physically reasonable.

It is extremely unlikely that the signal difference is attributed to a temperature increase. It can be assumed that around 50% of the total beam power (100 μW) is absorbed by the vanadium defects (SiC is transparent) with a defect concentration of 10^{17} cm^{-3}. In a 12 hour run that is $\sim$ 4.3 J absorbed. The laser beam diameter is 50 μm and the sample thickness is 300 μm. The heat capacity of V in the sample was calculated to be $C \sim 5 \times 10^{-12}$ J·K^{-1} (molar heat capacity taken from Worley et al. [91])

$$C = \left(\frac{10^{17} \text{ cm}^3 \cdot \pi(25 \ \mu\text{m})^2 \cdot (300 \ \mu\text{m})}{6.022 \cdot 10^{23}} \right) \cdot C_{\text{mol}} \approx 5 \times 10^{-12} \text{J} \cdot \text{K}^{-1}$$

The temperature change due to 4.3 J of energy added to the system is given by

$$\Delta T = \frac{4.3 \text{J}}{5 \times 10^{-12} \text{J} \cdot \text{K}^{-1}} \sim 10^{-11} \text{K}.$$

A $\sim 10^{-11}$ K is wholly negligible and would not be able to cause any discernable change in the relaxation rates.

C.IV   Preliminary Results: OD2LSR at 1.8 K

Figure C.1 shows recent (early May 2023) OD2LSR results at 1.8 K, with the microwave frequency set to the $g_6 - g_8$ transition at 40 mT. It can be seen that although the two-laser baseline signal is lower than the one-laser signal, at the ~ 525 MHz peak, the two-laser signal surpasses the one-laser signal. As explained in Section 4.1, this strongly suggests that the signal difference is due to a population leakage over the inhomogeneous ensemble.

C.V   Inefficacy of the USRN

When developing the protocol for experimental verification, the USRN was maximised to find promising points of initialisation. When no initialised magnetic resonance was seen for $g_7 - g_9$ at the 30 mT clock transition,[13] the efficacy of the USRN was evaluated. It was discovered that the ESD probability cannot be simply maximised to find potential points of good coherence, and hence, the USRN was not a good measure of possible coherence. The ESD probability is inherently linked to the spin-relaxation probability (both use the ESF, NSF, FF, FFz relaxation operators). In this way,

---

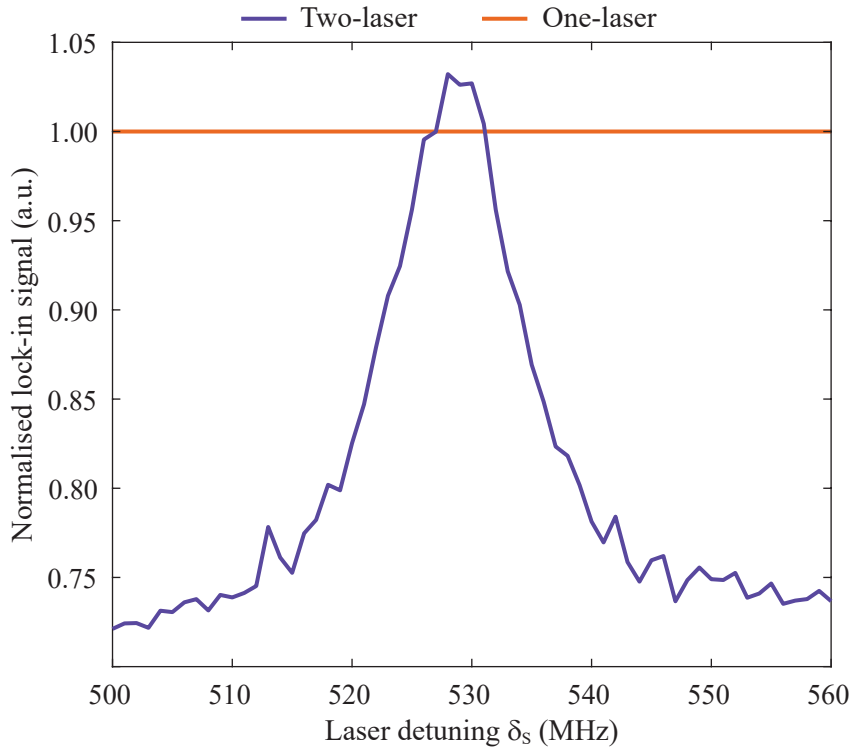[13]Note that for brevity this was not mentioned in the main text.

Figure C.1: OD2LSR measurement at 1.8 K normalised with respect to the one-laser signal. Notice that the two-laser signal surpasses the one-laser signal at the ~ 525 MHz peak. As explained in Section 4.1, this strongly suggests that the signal difference is due to a population leakage over the inhomogeneous ensemble.

the higher the ESD probability, the higher the spin-relaxation probability. While a high ESD probability indicates a good chance of driving coherently, a high spin-relaxation probability means worse initialisation, and hence a worse ΔP. Therefore, if the ESD probability is too high, the contrast between the two states being driven will be very low. Conversely, if the ESD probability is too low, the contrast will improve, but driving the transition coherently is very unlikely. In Figure C.2 it can be seen that the ESD probability for $g_7 - g_9$ at the 30 mT clock transition is around $8 \cdot 10^{-2}$. Since this transition has been coherently driven before [62], it suggests that the ESD probability should be larger than 10^{-2} to facilitate coherent driving, but still be lower than the $g_7 - g_9$ ESD probability ($\sim 10^{-1}$), as no initialisation was seen for g_7 or g_9, implying relaxation that is too strong for initialisation. The qubit candidate $g_6 - g_8$ at 40 mT can be seen to have an ESD probability of around $4 \cdot 10^{-2}$, half of the clock transition probability. While no coherence was seen for $g_6 - g_8$, initialised magnetic resonance was observed via OD2LSR measurements. The reason for there being no coherence measured for $g_6 - g_8$ might do with the fact that this is an electric quadrupole transition, and therefore it cannot be coherently driven with a magnetic field. This insight into the ESD probability means that the USRN is not a good measure of potential initialised coherence, or even potential initialised resonance. In Section 5, the initialisation approach is purely focused on maximising the population contrast ΔP for this reason.

C.VI   Coherently Driving Effective-Spin Transitions

Before coherently driving an initialised qubit candidate, the main process mediating the transition must be determined. As outlined briefly in Section 2.4, transitions primarily mediated by a $\Delta m_I = 1$ process are magnetic dipole transitions, whereas $\Delta m_I = 2$ are electric quadrupole transitions. For
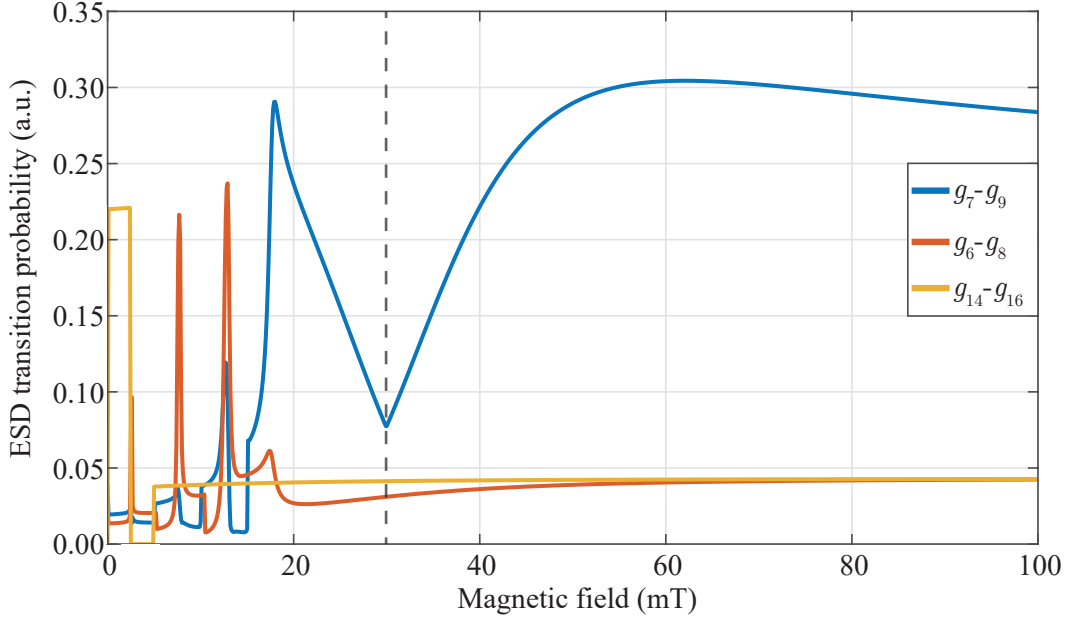
Figure C.2: ESD transition probability $|\langle g_j | \mathcal{O}_{esd} | g_i \rangle|^2$ of three transitions $g_7 - g_9$, $g_6 - g_8$, and $g_{14} - g_{16}$, with the latter two being qubit candidates in Section 5. It can be seen that below 30 mT (dashed grey line), the ESD probability is erratic with respect to an increasing magnetic field, reflecting the strong and unpredictable relaxation pathways in this region. $\gtrsim 30$ mT, the system starts to stabilise, as it enters the electron Zeeman dominated regime.

magnetic field driving (done with microwaves in experiment, see Section 3), only magnetic fields parallel to the c axis can resonantly (and coherently) drive transitions, as $g_\perp \approx 0$ in vanadium [61]. For electric fields, it is not currently known whether a parallel or perpendicular field is needed, as the resonance/ coherence properties of electric quadrupole transitions are outside the scope of this work. However, some insight can still be given based on what is seen in experiment and simulation.

The qubit candidate $g_6 - g_8$ at 40 mT is mediated primarily by a nuclear spin flip of $\Delta m_I = 2$, thus an electric quadrupole transition. Optically detected magnetic resonance (ODMR), and initialised spin resonance (OD2LSR measurement, Figure 4.1) with magnetic fields was detected (ODMR of this transition was also measured in Hendriks et al. [62]), indicating that the transition can be resonantly driven by magnetic fields. No coherence was measured however (no Rabi oscillations were observed). Currently, it is thought that this $\Delta m_I = 2$ transition can be resonantly driven with magnetic fields due to a mixing of dipolar spin-states in g_6 and g_8, with this mixing resulting from the electric quadrupole perturbation to the Hamiltonian. A simplified picture can be made to understand this. At 40 mT, eigenstate g_8 has an overlap with the spin state $|\uparrow, -5/2\rangle$ of $|\langle g_8| \uparrow, -5/2\rangle|^2 \approx 10^{-4}$, and g_6 has an overlap $|\langle g_6| \uparrow, -5/2\rangle|^2 \approx 10^{-5}$. If the nuclear electric quadrupole is removed, these overlaps are exactly zero. While these overlaps are small (compared to the largest overlaps $|\langle g_8| \uparrow, -7/2\rangle|^2 \approx 0.999$ and $|\langle g_6| \uparrow, -3/2\rangle|^2 \approx 0.82$) they are not negligible. These nonzero overlaps between g_6, g_8 and the spin state $|\uparrow, -5/2\rangle$, with both transitions mediated by a $\Delta m_I = 1$ process, indicate that magnetic spin resonance is weakly driven via these dipolar spin-state terms. When the magnetic field is further increased, the level of spin-state mixing in the eigenstates decreases. At 99 mT for example, these overlaps become $|\langle g_8| \uparrow, -5/2\rangle|^2 \approx 5 \cdot 10^{-6}$ and $|\langle g_6| \uparrow, -5/2\rangle|^2 \approx 10^{-6}$. This is an order of magnitude lower than at 40 mT, and would make magnetic field driving harder.

The solution then seems to be to use electric field driving for these $\Delta m_I = 2$ transitions. It is not

known whether a perpendicular or parallel electric field should be used for the driving. Gilardoni [72] (Chapter 4) uses symmetry arguments to show that transitions between the effective-spin manifolds of a Kramers doublet (KD) cannot be driven by electric fields perpendicular to the crystal c axis. Whether this is the case for nuclear spin transitions is not known. Theoretically, this could be investigated further by utilising a similar operator to the effective-spin driving operator $\mathcal{O}_{\mathrm{esd}}$ to quantify electric quadrupole transitions. Experimentally, electric spin resonance can be tested by using a capacitor (e.g. via gold deposition on SiC sample) to apply homogeneous electric fields.

D Appendices to Section 5: Theoretical Single-Defect Initialisation

D.I Suggestions for Continuous-Wave Experiments

Despite the high fidelities achieved in the single-defect initialisation processes developed in Section 5.2, a problem arises when applying this to experiments utilising continuous-wave lasers, such as the optically-detected two-laser spin resonance (OD2LSR) measurements. If attempting to probe, characterise, or initialise with an approach involving two lasers which are continuously on (also during the application of the coherent driving field e.g. microwaves), one of the lasers has to be resonant with the CP state for optical readout. Thus, the initialisation driving scheme must include a transition with a CP state. The detunings suggested (48 mT, g_8: 71 MHz, 108 MHz and 99 mT, g_{16}: -252 MHz, -259 MHz) are not resonant with the proposed CP states, g_6 and g_{14}. Furthermore, due to the dynamics explained in Section 5.1, optical resonance with these CP states is greatly suppressed in circularly-polarised driving schemes. For example, $|\langle e_{14}|\mathcal{O}_+|g_{14}\rangle|^2 \sim 10^{-11}$ at 99 mT, making it practically very difficult to drive. If linear polarisation were to be used instead, another problem arises; driving these CP states redistributes the population. For example, if attempting to initialise g_{16} at 99 mT using the $e_1 - g_1$ transition (-259 MHz), which results in a fidelity of $\gtrsim 0.8$,[14] while simultaneously accessing $g_{14} - e_{14}$ (260 MHz with $|\langle e_{14}|\mathcal{O}_{\text{opt}}|g_{14}\rangle|^2 \sim 0.99$) for optical readout, the fidelity of g_{16} drops to ~ 0.3. This is less than half of the initial fidelity, as seen in Figure D.1b. This is because the $g_{14} - e_{14}$ transition, which is a $\downarrow \Longrightarrow \nearrow$ transition, initialises into g_8 in the $\uparrow$ manifold, as explained previously. Furthermore, cross transitions within the same spin manifold (in this case, $g_{14} - e_i$ for $i = 9 - 13$, 15, 16) are much weaker than direct transitions, with the strongest spin-manifold-conserving cross transition being an order of $\sim 10^5$ weaker than the direct transition. These cross transitions would result in a weaker population redistribution effect, but would be much harder to drive and require stronger driving fields. This in turn could accelerate relaxation rates, and might even cause temperature increases in the sample. Therefore spin-manifold-conserving cross transitions are not ideal for optical excitation.

It should be noted that in applications where the system is directly manipulated after initialisation, this lack of an optical readout transition is not a problem. As was seen in Section 5.3, using a pulsed initialisation protocol negates the need for optical readout during initialisation. However, continuous-wave experiments (e.g. OD2LSR) have much simpler pulse sequences, and can still provide valuable insight into the system. Therefore, it is important to find a remedy for this optical readout problem. Currently, there are three possible solutions for this. The first would be to use two linearly-polarised lasers, wherein one laser drives the prominent initialisation transition, and the other drives a CP spin-manifold-cross transition. Linear polarisation is required as cross transitions are greatly suppressed in circular polarisations. Carefully chosen cross transitions can help maintain the fidelity while accessing the relevant CP state. For example, initialising into g_{16} at 99 mT by driving the $g_1 - e_1$ transition to achieve a baseline fidelity of $\gtrsim 0.8$, a cross transition can be found to access g_{14} while also maintaining the fidelity above 0.8. The strongest g_{14} cross transition at 99 mT is $g_{14} - e_2$ with an overlap of $|\langle O_{\text{optical}}\rangle|^2 \sim 10^{-2}$ and a detuning of -3079 MHz. Conducting a two-laser initialisation with the detunings -259 MHz ($g_1 - e_1$) and -3079 MHz ($g_{14} - e_2$) yields a promising result. The fidelity actually increases from the baseline, albeit by less than 0.01 (i.e. $F < 0.801$). The reason it increases is because via a combination of GS1 and ES1 relaxations, population from e_2 eventually ends up in g_1 and is subsequently driven. This relaxation pathway is quite weak however, which is why the increase is less than a percent. Nonetheless, this is a two-laser initialisation scheme resulting

---

[14]Of course, due to spectral diffusion and other environmental factors, one-laser initialisation is practically very hard to achieve. Spectral diffusion is not included in the model however, and as such, one-laser initialisation (for single defects) is possible within it. Therefore, values relating to one-laser initialisation are to simply give an indication of the effect of different driving schemes on the overall fidelity.
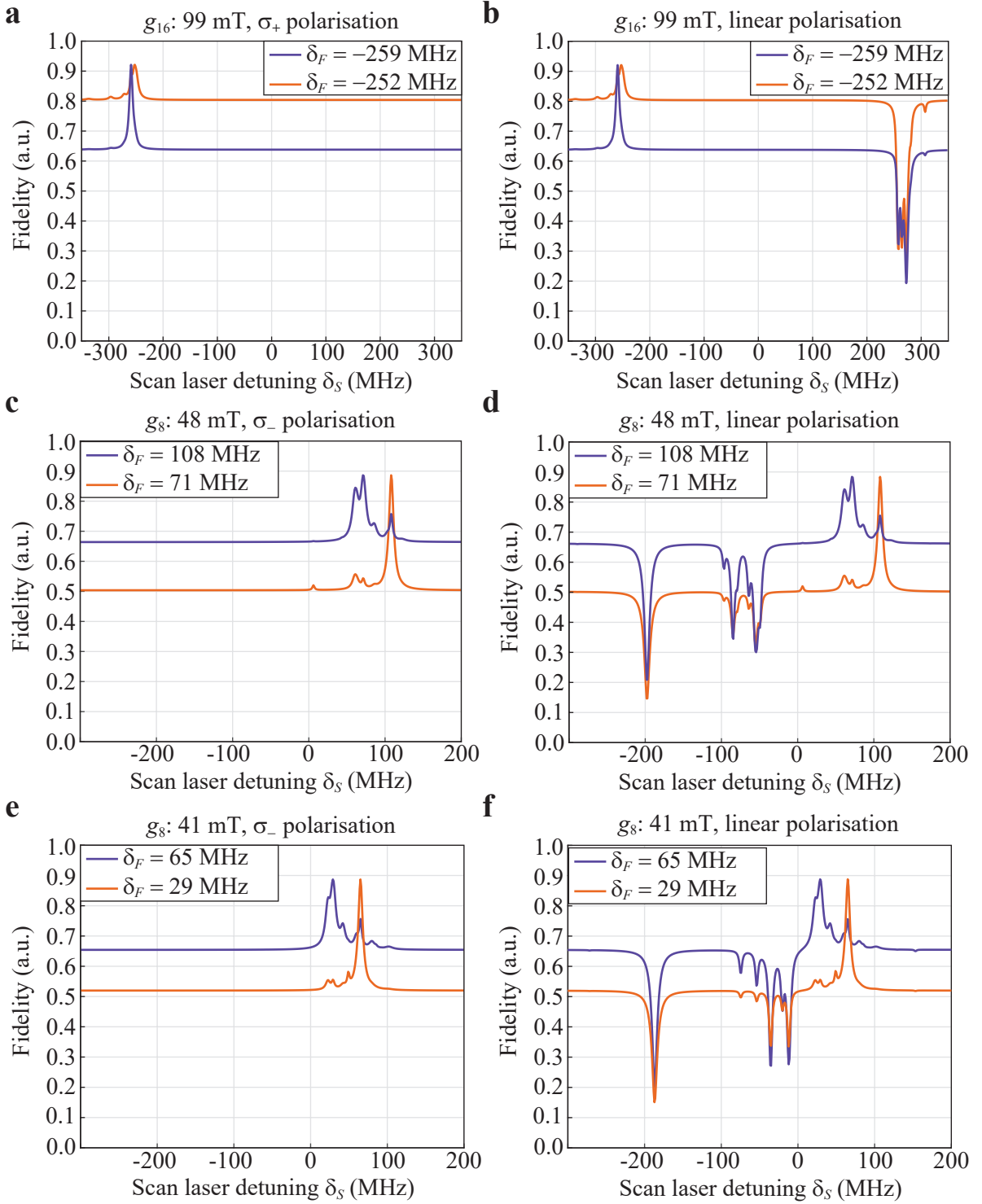
Figure D.1: Two-laser initialised fidelities of g_{16} at 99 mT (**a**, **b**) and g_8 at 48 mT (**c**, **d**) and 41 mT (**e**, **f**) as a function of scan laser detuning δ_S (other laser detuning δ_F kept fixed) for different magnetic fields. The left panels show the fidelity using the relevant circular polarisation (σ_+ for g_{16}, σ_- for g_8) while the right panels show the fidelity using linear polarisation. Each peak and dip represents resonance with some optical transition. Due to the optical linewidth, some resonances cannot be fully resolved and appear as a combination of peaks and/ or dips. Optically addressing the coherent partner (CP) states, g_6 (48 mT) and g_{10} (41 mT) for g_8 and g_{14} for g_{16}, for optical readout with linear polarisation results in a redistribution of population and a consequential reduction in the fidelity of g_8 and g_{16}, as can be seen in **b**, **d**, and **f**.

in a fidelity of > 0.8 with simultaneous optical readout. The same can be done for g_8 at 48 mT, wherein the scheme $g_9 - e_9$ (108 MHz) paired with the $g_6 - g_{10}$ (933 MHz) results in a fidelity of > 0.75. The fidelities from this method are not as high as in the previous method, but the CP states can be read out which is an experimental necessity in continuous-wave experiments.

The second solution would be to change the CP states from g_6 and g_{14} to states in the opposite effective-spin manifold, such that the qubit is either flip-flop or electron spin flip mediated. This would allow for initialisation and readout with only two circularly-polarised lasers. As discussed previously, the strongest interactions in GS1 are flip-flop mediated. However, g_8 and g_{16} have weak flip-flop coupling, and even weaker electron spin flip coupling, which is why they are easy to initialise into. Therefore, the contrast between the new CP state with the respective static state must be high, while also having an ESD probability which is not too small relative to the $g_7 - g_9$ clock transition. There are unfortunately no spin-manifold-cross transitions with ESD probabilities on the order of the clock transition ESD probability. That being said, the transitions $g_8 - g_{10}$ and $g_2 - g_{16}$ had the highest contrasts and are initialised by driving schemes[15] which are resonant with the CP state. While the state overlaps of these transitions are small as compared to the clock transition, with the appropriate driving field power, the transitions should still be able to be driven. However, increasing the driving field power might lead to unwanted effects in the sample, such as a temperature increase. Additionally, the transitions $g_8 - g_{10}$ and $g_2 - g_{16}$ are not ZEFOZ transitions, meaning that they are not protected from magnetic noise. Nonetheless, this approach would allow for fidelities of > 0.92 for a g_{16} initialised state, and > 0.88 for g_8 initialised states. Similar to the flip-flop mediated $g_7 - g_9$ clock transition at 30 mT, these transitions are also driven via magnetic spin resonance (due to the hyperfine magnetic dipole resulting from $\Delta m_I = 1$) as opposed to electric spin resonance.

Finally, a third laser could be introduced for optical readout. The third laser should have either linear polarisation, or the opposite circular polarisation to the initialisation lasers, such that the required readout probability $|\langle \mathcal{O}_{\mathrm{opt}, +, -} \rangle|^2$ is not suppressed. It also needs to be resonant with a transition involving the CP state, preferably a direct transition (highest probabilities). In this way, the system can be two-laser initialised to the highest achievable fidelity, an oscillating magnetic or electric field applied to drive the transition between the static and CP states, and the third laser used to read out the CP state. This is similar to the protocol that will be outlined in Section 5.3, except here the two initialisation lasers are kept incident on the sample. A caveat of this approach is the practical feasibility. Introducing a third beam would involve either the addition of another laser or adding a beam splitter to split one of the original two beams (Section 3.1 explains that the two beams used in the OD2LSR measurement already come from a beam splitter), which are not convenient modifications to make. Furthermore, the optical readout laser must be pulsed to ensure that it is not on during initialisation. If the readout laser were to be on while initialising, it could redistribute the GS1 eigenstate population (especially if it is a direct transition involving the CP state) and it could cause T_1 and contrast effects, as discussed in Section 4.1. However, pulsing the optical readout laser has complications for the OD2LSR measurement method. The lock-in frequency in the OD2LSR measurements was fixed to the microwave repetition rate. Introducing a pulsed optical readout laser means that the lock-in frequency must incorporate this. While possible, it is not trivial. This method is theoretically the most favourable, but has the most practical limitations.

With each of the above methods there is a trade-off between fidelity and practicality. The first method, wherein one laser is resonant with a CP state (g_6 or g_{14}), allows for optical readout and uses ZEFOZ transitions, but results in a non-negligible decrease in the fidelity. For g_{16} this was a

---

[15]Driving schemes are $g_1 - e_1$ and $g_2 - e_2$ for initialisation into g_{16}, and $g_9 - e_9$ and $g_{10} - e_{10}$ for initialisation into g_8.

decrease from ~ 0.92 to ~ 0.8, while for g_8 it was from ~ 0.88 to ~ 0.75. The second method, wherein the CP states are changed such that the qubits are flip-flop mediated, allows for high-fidelity initialisation but low ESD probabilities. This means that the coherent driving field must be considerably more powerful, which could lead to unwanted effects on the initialisation. Furthermore, the qubits proposed are not ZEFOZ transitions. The last method, wherein an additional laser is used for optical readout, is theoretically the most favourable. This is because high initialisation can be achieved with ZEFOZ qubit candidates. However, this method is practically the most inconvenient. The quantitative advantages and disadvantages of these methods have not yet been fully determined. Ultimately, seeing as the theoretical model is a simplified picture of the physical system and as such cannot provide all the necessary information, it would be best to implement these different methods experimentally. Only then can a more informed conclusion be made on the efficacy of these methods. What can be concluded however, is that g_8 and g_{16} in the electron Zeeman dominated regime are prime candidates for initialisation, reaching fidelities far above any other GS1 eigenstate.